Design and Control of a Direct Drive Slotless Permanent Magnet Alternating Current Generator for Low Speed Bristol Cylinder Wave Device

by

Sze Song Ngu

Submitted in fulfilment of the requirements for
the degree of Doctor of Philosophy (Ph.D.)

Electronics and Electrical Engineering
School of Engineering
College of Science and Engineering
The University of Glasgow

July 2013

Abstract

Global demand for renewable energy is at an all-time high. Renewable energy can be extracted from naturally available resources such solar, wind, tides, geothermal heat, sea waves and the others. The percentage of renewable energy in the energy resources is increasing at an ever increasing rate. While much renewable energy is large scale, it is also suitable for rural and remote areas.

The challenges facing today's renewable energy supply industry are many, especially in the wave energy field which is still underdeveloped. The number of commercialised wave energy devices is very limited and the concepts implemented for harnessing wave energy are very different between the different devices and often struggle to be effective or survive ocean-going conditions. Thus, major research is required to find new and effective methods for harnessing wave energy which are able to supply power to the grid with high conversion rate and good reliability.

The proposed Bristol cylinder device, in theory, should be able to harness sea wave energy and to convert it into useful electricity, and this device is studied in detail here. This device is still new in terms of practical application in ocean conditions. It needs power electronics and effective controllers for high-efficiency power extraction and to be successfully integrated into the power grid. When the device was first investigated in the 1970s, power electronics and variable-speed brushless permanent-magnet machinery was simply not developed to the level it is today, hence the revisiting of this device several decades later. A successful Bristol cylinder wave device which can extract renewable energy may well impact on the renewable energy sector.

The wave characteristics were studied and simulated using Airy Linear Wave Theory and Stoke's Second Order Theory. The dynamic characteristics of the Bristol cylinder are investigated when interacting with waves, together with the control necessary to make it a functioning device. A lab scale wave tank suitable to test the Bristol cylinder is designed.

A surface magnet permanent magnet synchronous generator (PMSG) design is considered in this research project. This generator configuration shows its suitability in producing high conversion-rate power when working in a low speed environment. The sizing exercise is performed to determine the size of the lab scale PMSG. Analytical analysis and finite element analysis is performed to study the performance of the designed PMSG. A study of the effect of the armature length with the corresponding incident wave is done. Field oriented control (FOC) is applied to control the speed of the generator. FOC is shown to be suitable for stable control of the generator speed. Simulations using MATLAB are utilized and Simulink is used to construct the model and evaluate the potential performance of the control system design. In this thesis, theoretical analyses and simulations of the generator performances are carried out for several generator topologies and sizes. The grid side converter controller technique is also simulated in MATLAB/Simulink and the performance evaluated.

Acknowledgements

Throughout my university life, at five different universities, in three different countries, I have learned and realised that I could never have done any of this, particularly the research and writing that went into this dissertation without the support and encouragement of a lot of people.

First and foremost I would like to express my deepest gratitude to my main supervisor, Associate Professor David Dorrell (now with the University of Technology, Sydney, Australia) for his guidance and criticism in this thesis throughout the entire research process. His valuable direction, suggestions, thoughtful support, advice and patience were fundamental in order to carry out such successful research work. Thanks for motivating me to undertake this research project.

I would also like to thank my second supervisor, Mr. Calum Cossar for providing the much needed support related to this work. Likewise, I would like to thank my second main supervisor, Professor Enrique Acha for his supervision, criticism, encouragement, support and advice which were important in the development of this thesis.

Furthermore, I would like to thank Green Cat Renewables especially Mr. Cameron Sutherland for providing the opportunity for site visit at Newcastle during the start of my research. It gives me the opportunity to view the actual wave device and to get the idea to start my research. Besides that, I would like to thank University of Technology, Sydney for the appointment as visiting academic for the short term placement in the university to complete part of my research there.

Many thanks to my friends and colleagues in the Energy group and the Power Engineering group in the School of Electronics and Electrical Engineering. I have learned so much from all of you especially Dr. Jin Yang, Mr. Majid Mumtaz, Dr. Bazad Kazemtabrizi, Mr. Liam MacIsaac, and Mr. Graham Morton. Thanks for making the working environment enjoyable too.

The financial support for this research project given by Universiti Malaysia Sarawak (UNIMAS) in the name of Doctorate Training Award is gratefully acknowledged.

Finally, I would like to thank my family for their love and support throughout this time. Special thanks to my father Dato' Dr. Piew Seng Ngu, my mother Mdm. Swee Yung Ngu, my wife Lee Chin Kho, my daughters Kimberly Shu Yee Ngu and Kathy Shu Xuen Ngu, my sisters Ms. Sophia Sze Ling Ngu, Dr. Sze San Ngu, Dr. Sze Ting Ngu, and my brother, Dr. Sze Liang Ngu for their love and unconditional moral support.

Table of Contents

List of Figures

List of Tables

List of Symbols

a	Sea wave amplitude, vertical distance between the still water level and the crest or trough (half the wave height)
c	Capacitance
d	Water depth
$dq0$	direct-quadrature-zero
e	Back-EMF induced into the windings by the PM excitation
f	Sea wave frequency in Hz
g, g_l, g_{FS}	Gravitational constant
h_g	Effective air-gap length between the PM and the stator core (for an air-gap winding this includes the thickness of the winding layer)
h_m	Magnets thickness
h_{tooth}	Stator tooth height
i_{inv}, i_{rec}, i_c	Currents
i_{qo} , i_{do}	Currents
j	Square root of -1
k	Wave number (dimensionless parameter)
k_{ad}	d-axis armature reaction factor (unity for a surface magnet machine)
k_d	Distribution factor
k_f	Winding factor to assess the effectiveness of the winding layout
k_{fr}	Form factor of the rotor flux (depends on the rotor topology)
k_p	Pitch factor
k_s	Slot opening factor for a slotted stator or the spread of the air-gap coil for an air-gap winding
k_{sk}	Skew factor
l_m	Magnet width
l_p	Pole width at the mean air-gap radius
l_{st}	Pole pitch arc length at the mean stator yoke radius
m	Cylinder mass
n	Harmonic number
p	Number of pole pairs
p_d, p_s	Dynamic pressure

r	Rotational radius of the Bristol cylinder
t	Time
$u,\ u_s$	Horizontal particle velocity of water particle
$\dot{u}\ , \dot{u}_s$	Horizontal particle acceleration of water particle
$v_d\ , v_q$	Voltages
v_g	Grid voltage
$v_{qg}\ , v_{dg}\ , v_c$	Voltages
$w,\ w_s$	Vertical particle velocity of water particle
$\dot{w}\ , \dot{w}_s$	Vertical particle acceleration of water particle
x	Instantaneous distance
z	Instantaneous water particle distance which is the vertical distance from the still water level

A_p	Average magnetic field over the positive part of the coil
A_m	Average magnetic field over the negative part of the coil
B	Magnetic flux density
B_{gap}	Air-gap flux density
B_r	Remanence
B_{sat}	Saturation flux density
C	Celerity (wave speed)
$D,\ D_l,\ D_{FS}$	Water depth
D_c	Cylinder diameter
D_d	Damping coefficient
D_{rw}	Relative depth of water
D_r	Rotor diameter
D_s	Rotational axis depth
E_d	Energy density of sea wave
E_{ph}	Induced phase back-EMF
E_{PM}	Per phase armature terminal voltage
F_R	Froude number
G	Gain

H, H_l, H_{FS}	Sea wave waveheight, the vertical distance between the crest and the following trough
H_c	Coercivity
$H_{cut\text{-}in}$	Cut-in waveheight
$H_{cut\text{-}out}$	Cut-out waveheight
H_{cu}	Surface current density
H_m	Magnetic field intensity
H_n	Nominal waveheight
H_{tooth}	Stator teeth coercive force
H_{yoke}	Stator yoke coercive force
I_c	Coil current
$\bar{I}_{ph}$	Phase current vector
I_{sd}, I_q*	Currents
I_p	Peak current
J	Moment of inertia
K	Output coefficient
K_s	Stiffness coefficient
L	Sea wave wavelength, the horizontal distance between the crests or troughs of continuous sinusoidal waves
L_i, L_q, L_d	Inductances
L_w	Winding inductance
L_{stk}	Stack length of rotor
N	Speed of the rotor in rev/min
N, N_c	Number of turns of windings
N_1	Total turns number per phase
N_m	Number of magnet poles on the rotor
P	Mean power per meter of sea wave front
P_d	Sea wave power density
P_g	Active power
$P_{\max}$	Maximum generator power
P_t	Turbine power
PV	Generator bus
PQ	Load bus

Q_g	Reactive power
R	Resistance
R_{Fe}	Stator yoke reluctance
R_{ph}	Phase resistance
R_{PM}	Magnets reluctance
R_r	Rotational radius
R_δ	Air gap reluctance between magnet and stator
$R_{\delta 2}$	Leakage reluctance in the inter-magnet region
S	Wave steepness
T, T_l, T_{FS}	Wave period
T_t, T_e	Torque
T^{-1}	Transverse matrix
V, V_l, V_{FS}	Wave velocity
V_M	Magnets volume
$\overline{V}_{ph}$	Phase voltage vector
X_s	Synchronous reactance
X_d	d-axis reactance
X_q	q-axis reactance
σ	Sea water density
σ	Sheer stress
ω	Wave frequency in rad/s
ω_e	Angular frequency
ω_m	Angular velocity in rad/s
η, η_s	Surface wave elevation
£	Sterling pounds
λ	Geometric scaling factor
λ_a	Amplitude of flux induced or scaling factor
λ_{PM}	Permanent magnet flux linkage
μ	Relative permeability
γ	Electric conductivity
θ_{LOAD}	Load phase angle

ϕ_δ	Air-gap magnetic flux
ϕ_{PM}	Permanent magnet total magnetic flux
ϕ_σ	Magnets end regions additional leakage fluxes
ϕ_{PM+C}	Flux linkage with magnet and coil current
ϕ_C	Flux linkage due to coil current
μ_0	Air permeability
μ_{PM}	Relative magnet permeability
Θ_{PM}	Magnetomotive force
$\Theta_{t(i)}$	MMF in stator teeth
$\Theta_{s(i)}$	MMF in yoke
ϕ_c	Coil offset
α_c	Coil pitch
β_c	Slot opening angle
Φ	Magnetic flux
Ψ	Flux linkage
θ	Angle of the rotor with respect to the reference axis
θ_e	Electrical position, the position of the rotor shaft
θ_m	Mechanical position, the position of the rotor shaft
π	= 3.142 rad
ε	Relation between no load induced EMF and net voltage
ζ	Magnet utilization coefficient
$\lvert\ \rvert$	Magnitude

Chapter 1

INTRODUCTION

1.1 Background

Renewable energy has emerged as one of the most discussed topics in the electricity generation field. Renewable energy has been labelled as green energy due to its minimum pollution and the freely available and sustainable sources. The total energy generation from renewable resources is projected to increase by 3 % annually [1]. Some renewable energy sources are now being commercially exploited; these include the hydropower, biomass, geothermal, solar and wind power. The technologies within these renewable energy areas are established with energy entering the energy supply market. Meanwhile wave and tidal energy technologies are still under development and they are not yet widely demonstrated nor commercialized. There are several prototypes systems across the world and some of these are generating onto the grid [2]-[5]. This has created many new research opportunities in the renewable energy sector. The aim is to develop new energy absorption devices for energy conversion purposes, and to control these devices to maximize energy conversion. The whole process of converting renewable sources into useful energy is very demanding and complicated. It involves designing new devices to tap the raw energy, converting it to useful energy depending on the purpose, and transmitting it to the required destination. The device has to be robust and durable.

The study of wave energy is reported to have commenced in 1970 [6]. However, due to the complexity and difficulty in extracting the energy, it is still not widely utilized. Ocean waves are complex, very irregular and unpredictable. Deep water wave power available throughout the world is estimated to be around 8000 to 80000 TWh in 2007 [6]. This shows that the potential of harnessing energy from waves is feasible and there have been several studies around the world reporting on the wave resources in a particular location [7]-[14]. There are now many early stage marine energy systems being developed; although it is acknowledged that, while the

wave devices work in theory, there are bigger challenges ahead in terms of conversion rates, robustness, control, cost, and maintenance of the whole system.

One system that is of particular interest in this research is the Bristol Cylinder type of device. While the device was developed by Evans *et al* in 1979 [15], it is still in the early research stage by Green Cat Renewables Ltd, UK; this report will concentrate on the understanding of the nature of sea waves, the operation of the device, the design of generator that fits into it, and a control system that will use incoming wave parameters to tune the turbine to individual waves. The device requires a very low speed generator for some sea states hence, close speed and position control is needed.

To contribute towards achieving such aims, the research work reported in this thesis uses Linear Small Amplitude Wave Theory and Stokes Second Order Wave Theory to study the nature and characteristics of deep water waves. Based on the work done, these theories are the most suitable for explanation of the interactions between waves and the device, and the control requirements for the movement of the wave device. This report also highlights the design process of a multi-pole PMSG that fits into the particular device. Last but not least, a full scale control system is proposed for maximization of the power and protection of the device.

1.2 Problem Definition

There are a few common wave devices which have found application for sea wave energy generation. These include the Oscillating Water Column (OWC) [16-18], point absorber devices [19-21], surge devices [22-24], attenuator devices [25-27], and the overtopping devices [28-30]. These devices use different concepts in the way they function and are unique in the way they harness and convert the energy. This report will focus on the Bristol Cylinder wave device which is not classified under any of the categories mentioned above.

For the Bristol cylinder, Evans *et al* [15] assumed a submerged cylinder with Cartesian movement where the, work is done in horizontal and vertical directions (two-dimensional theory); McIver et al [31] assumed a three dimensional effect. For

this research, it is assumed that a cylinder placed into the water will moves in circular motion. This is shown in Fig. 1.1. The device requires a very low speed generator system, in the region of 6 rpm if the sea state has a 10 s period. A gearbox can be utilized, or a high pole number generator (as used here). The power (or energy) from this sort of device is likely to pulsate with every wave, the degree to which the energy pulsates needs investigation. In Fig. 1.1, the cylinder is rotating around a central point (the dashed circle) and it is held here at each end by an armature (black). The armature is centrally pivoting on a rigid structure, such as a tower. The other end of the armature is connected to the cylinder and the reaction at this point is created by the generator. The cylinder itself does not rotate on its own axis. In the figure, the generator is shown as a gearbox and small generator although in this thesis a direct-drive generator is proposed.

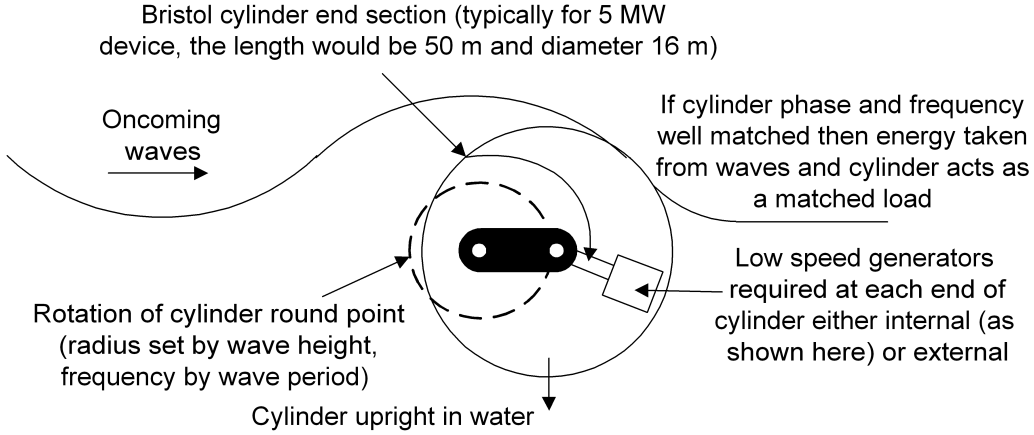

Fig. 1.1. A Bristol Cylinder representation.

When Evans *et al* first conducted their research in the 1970s much of the power-chain mechanisms that are so common today were not available then. Brushless rare-earth magnet machine were still in very early-stage development and the very strong material (sintered neodymium iron boron (NdFeB)) was not available. The electrical power train in this device will probably comprise of a diode or controlled (with metal oxide semiconductor field effect transistors (MOSFETs) or insulated gate bipolar transistors (IGBTs)) rectifier, followed by a direct current (DC) link, then through to an inverter to transform the energy into an alternating current (AC) electrical form for connection to the grid via a transformer and suitable switchgear. By the nature of sea waves, the period could be up to 20 seconds and if

the power is pulsating, this may require substantial electrical energy storage on the DC link in order to smooth the energy output [32].

1.3 Project Objectives

The main objectives of this research are described below:

- To study the wave behaviour and characteristics. The interactions between the wave and the Bristol Cylinder wave device need to be described and understood. The focus will be on the amount of energy transferred from the waves to the wave device and also the torque absorption capability of the wave device. From a modelling point of view, critical inputs (that will serve the purpose of simulation) need to be identified and fed into the system for optimum control.
- To propose and design a lab scale wave tank which will act as a testing bed for the proposed energy caption system.
- To design an AC PMSG that fits into the Bristol Cylinder. This involves the sizing of the rotor and stator, the choosing of raw material, the choice of generator topology or configuration, winding and et al. This generator must be able to function at very low rotational speed. The design will be carried out using Finite Element Method Magnetics (FEMM) and PC-BDC *SPEED* software.
- To develop a control system necessary for the Bristol Cylinder sea wave energy capture device where the issues concerning harvesting a slow, propagating sea wave, and pulsating power will be highlighted. The development, testing and simulation will be completed using MATLAB/Simulink.
- To simulate a grid side converter control technique to maximize the power.
- To conduct a sizing exercise to scale the lab device to a full sized device.

1.4 Outline of the Thesis

The thesis is organised as follows:

Chapter 2 reviews the key aspects of wave energy and the application of the Bristol Cylinder to conversion from the travelling waves of potential energy in the waves to rotational mechanical energy. The quantification of wave power is addressed

in terms of monochromatic waves. Theories that lead to dynamic wave behaviour and their properties are discussed. An overview of the current range of wave devices under development is presented and the principle functions of the Bristol Cylinder wave device is put forward. A lab scale wave tank design is presented; its dimensions based on the wave and wave device characteristics are discussed. A review of typical wave resources in different global locations is completed and a scaling exercise for a full sized device is carried out. Finally the costing of a full scale device is presented.

Chapter 3 reviews the existing permanent magnet (PM) machine technology within the context of application to generators for renewable energy systems; this review concentrates on the application to low speed PM generators. The design aspect of the generator is then presented which includes descriptions of various generator topologies, magnetic materials, windings, and generator sizing. The main considerations are discussed and a generator is designed specifically for the Bristol Cylinder. The designed generator is then analysed using analytical and finite element methods. A generator design, together with its performance assessment, is presented.

Chapter 4 assesses the control strategies needed to ensure that the wave device will be fully utilized in terms of wave power delivery and that the generator energy conversion is high. An overview of the system considerations is given together with the generator speed control system. The control strategies are then simulated using MATLAB/Simulink. The result is simulation of the armature length corresponding to the incident wave. This is to protect the wave device against storm damage where sea conditions will be extreme. A mathematical model of the speed control system is put forward and its effectiveness in maximizing the PMSG output power is discussed. The indirect FOC method is proposed and analysed in this research. A few case studies are outlined at the end of the chapter in order to evaluate the performance of the whole system.

Chapter 5 addresses the importance of grid side converter control. The UK grid code is briefly reviewed. The control loops within the controller are discussed and the control strategy is then simulated using MATLAB/Simulink. The main goal is to maximize the power transmission to the grid. The control system is simulated to

test its performance and to study on the feasibility of connecting the wave device to the grid.

Chapter 6 presents the major conclusions from the research project, and discusses future research opportunities that are highlighted by the work.

Chapter 2

WAVE ENERGY

2.1 Introduction

Wave power actually refers to the energy potential carried by sea surface waves and the conversion of that energy to do meaningful work which includes electricity generation. Wave power is different from other forms of marine energy such as tidal power, ocean current power, tidal power, and power extracted from temperature and salinity gradients [33]. Waves are caused by wind as it blows over the surface of sea. It can be a powerful source of energy which is yet to be not utilized. To date, wave power generation is not a commonly available commercial technology although there have been various attempts to use it. In 2008, the first wave farm was constructed in Portugal which is the Agucadoura Wave Park [34] and yet this wave farm is still in the experimental stage. There have been other systems that predate this which have been individual prototype devices [35]. Issues that have led to the lack of deployment are usually related to fact that actual wave energy is random and low frequency, and it is difficult for energy to be converted successfully and flow into a utility grid. Often the environment is hostile with extreme conditions often occurring. However, the issues concerned with power electronic energy conversion [36], pulsating power [32] and subsea power transmission [37] are being addressed.

Wave energy could play a crucial role in meeting long term renewable energy targets, which will lead us to pollution-free or low carbon emission electricity generation. It is projected that on the Scottish west coast, the mean wave power is often in excess of 60 kW/m of wave front. Offshore wave power potential is projected at 14 GW in Scotland which will provide some 45 TWh annually [38]. Like other renewable energies, wave energy is unevenly distributed over the world as shown in Fig. 2.1. Later in this chapter, wave data for different locations will be addressed for comparison.

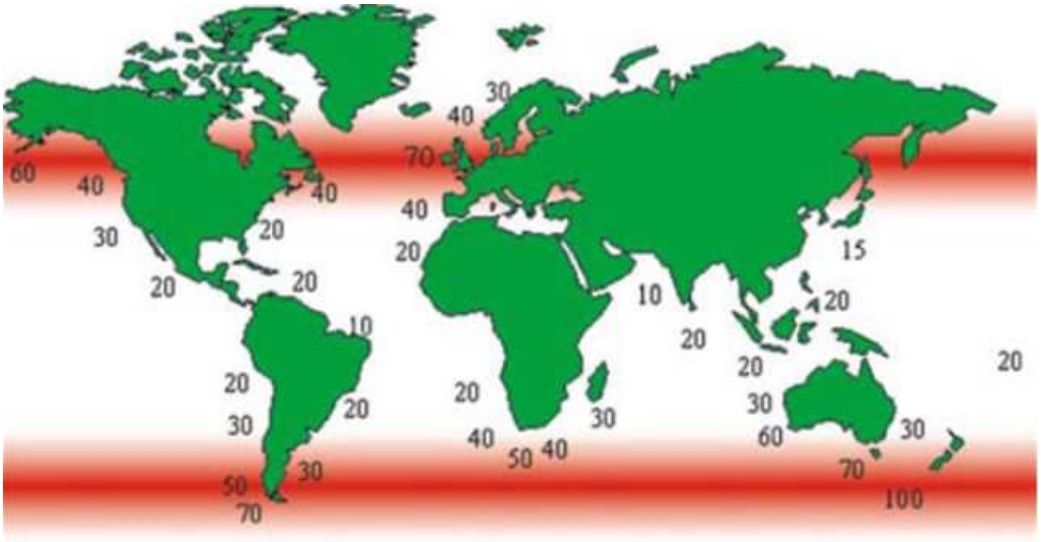

Fig. 2.1. Global wave power distribution in kW/m [39].

The advantages of wave energy are the source is free and available throughout the year and it does not produce pollution such as greenhouse gases. However, the safety risks with wave power generation can be considerable due to the ocean location of the systems. There will be capital costs involved in building a stable system which will act as the power station. There will be components that may be offshore or shoreline (acting as a sea defense), which are the electro-mechanical conversion components; and on-shore components related to the electrical conversion and grid connection. The cost of the former components will attract a construction premium due to their ocean-going nature and need to be storm-proof. Sea foundations or mooring can be very expensive top put in place. The operation and maintenance cost may be low but there may be site access issues in deep sea locations.

The amount of energy available is massive. However, waves can be small, with short wavelength (low energy) or large, with long wavelength (high energy) and they are uncontrollable; sometimes it may be necessary to shut down the system and enter a survival mode during passing storms (in a similar manner to wind turbines that tend to feather their blades and shut down above about 30 m/s to prevent damage). Suitable sites where wave are consistently strong, but manageable, need to be identified; and if there is some sheltering from storms that would be advantageous. The transportation of electricity from the sea onto the land will be an issue. Subsea cabling is expensive and DC transmission may be required when distances between

devices and the on-shore electrical hub and grid connection are long. Since wave energy conversion devices are still at the research and development stage, the cost of producing energy is too high be economically competitive. However, with advancing technology, both in terms of electro-mechanical energy conversion and off-shore power systems, this price should reduce.

It can be argued that the visual impact above water or on shore is considerable, however, this is very much an arbitrary assessment; wind turbines have been subjected to similar discussions. At this stage wave devices do not seem to produce a higher visual impact than wind turbines or shipping. More important is the impact on the environment both in terms of marine life and ecology and impact on the local land and sea. It may disturb marine life, and this needs correct assessment; there will be both vibrations and noise impact. There may also be issues concerned with sea transport in terms of shipping and fishing [40]. Hence there are many challenges to address in the process of harnessing wave energy efficiently and with minimal environmental, social and economic impacts. However, wave devices need to be first researched and developed before their impact can be fully understood.

2.2 Sea Wave Formation

Sea waves are formed by the combination of solar activity, earth gravity, sea surface tension, and wind intensity. It can be argued that sea waves are a derivative of wind, which is in turn a derivative of solar energy, so solar energy is the prime source of wave energy. Fig. 2.2 shows the formation of sea waves. Whenever the wave propagation is slower than the wind speed above it, energy will be transfer from the wind to the waves to set up a sea wave which is a propagating wave of potential energy (although kinetic energy is necessary to set up the rotational motion within the water). The wave size and wavelength is affected by the wind speed and fetch (which is the distance over which the wind excites the waves). It is also affected by the depth and topography of the seabed, which help to focus or disperse the energy of the waves. As the fetch increases then the shape will be more stable and the waves will become good swell waves, which have high amplitude, long period and long wavelength. These are the ideal waves for harvesting by wave devices because they are strong, more constant and predictable in the longer term. In Fig. 2.1 it can be seen that

western continental seaboards in more northerly or southerly locations (for instance, the north Atlantic of Scotland and Ireland, the south western shores of South America and South Africa and the shores of Western Australia and Tasmania) are good locations. Surge waves are due to storms and these are less predictable and can be extreme. These are not good waves for harvesting. Tsunami waves are due to tectonic plate activity rather than winds. These form one single wave of extremely long wavelength which has extremely high energy. These waves cause devastation and are obviously not harvestable.

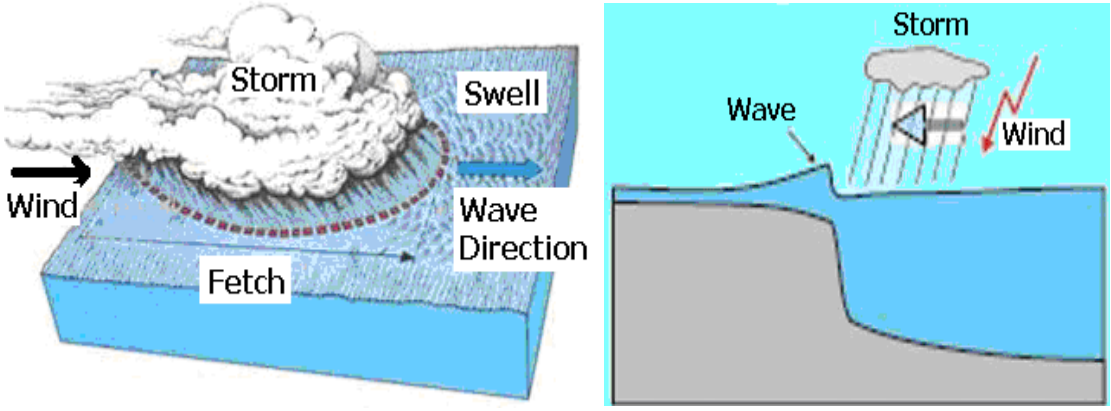

(a) (b)

Fig. 2.2. Sea waves transformation - (a) eagle view [8] and (b) side view showing surge.

2.3 Wave Properties

Fig. 2.3 shows the basic wave mechanics in deep water condition. The still water level refers to the sea surface level in the absence of wind or waves. Wave crests refer to the peak or top of the waves, while the trough refers to the lowest point of the waves. Wavelengths refer to the horizontal distance between the crests or troughs of continuous sinusoidal waves. These are monotonic waves, i.e., the waves are sinusoidal with one frequency. Real sea states have a spectrum of wave frequencies. The wave height H is the vertical distance between the crest and the following trough, while the wave amplitude refers to the vertical distance between the still water level and the crest or trough (i.e., half the wave height). Real sea states will have a range of wave heights at different frequencies and are hence random. This makes their short-term prediction difficult [41] although statistical breakdown over a

time period from a set of location measurements makes their long-term prediction possible.

As the water becomes more shallow, the motion of the water becomes more elliptical and the wave velocity slows, shortening the wavelength and eventually begin to break. At this stage the water is giving up its energy to the beach or sea bed.

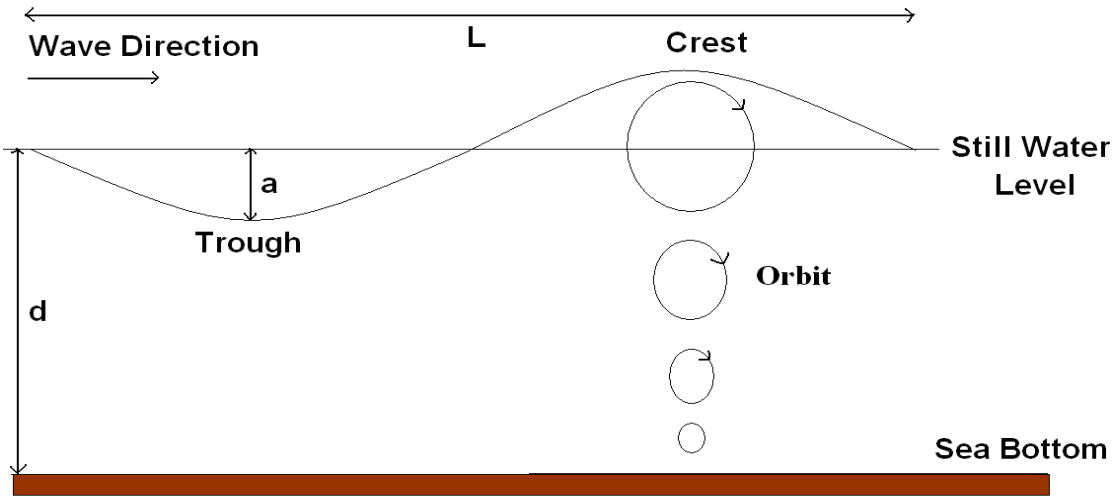

Fig. 2.3. Basic wave mechanics at deep water.

The behaviour of the water is now more rigorously examined in terms of wave theory and the definitions of deep, intermediate and shallow water put forward.

According to the small amplitude theory of surface water waves [42] which was first developed by Airy in 1845, waves can be classified based on the relative depth D_{rw} of the water. D_{rw} can be obtained by using the following equation:

$$D_{rw} = \frac{d}{L} \tag{2.1}$$

where d is the water depth and L is the wavelength. In the case where D_{rw} is more than 0.5, the waves are referred to as deep water waves [31]. Studies [43-45] show that in deep water conditions, the motion of the water particles have only a small net forward displacement; and particles beneath the wave essentially move in circular orbit, this is the an important characteristic in the operation of the Bristol Cylinder. While at shallow water, as already stated, the particles actually move in elliptical orbit. At the surface, the orbit radius is approximately equal to the wave amplitude. At deeper

depths into the water, the orbit radius will decreases as illustrated in Fig. 2.3. Many experimental observations have reported water particle motion; many of these are straightforward experiments employing techniques such as dye or droplet techniques; more sophisticated experiments use of electromagnetic methods, doppler techniques and drag devices. All these techniques have been applied with varying success [46].

Overall, wave energy move faster across the water surface if the wavelength is longer. For deep water waves, this relation can be obtained as shown below [47]:

$$C = \frac{L}{T} \text{ m/s} \tag{2.2}$$

where C is the celerity (wave speed), L is the wavelength in m, and T is the period in s. Compared to the wave period, the wavelength is more difficult to determine in the ocean. If the period can be measured, the wave speed can be estimated as from [46]

$$C = 1.56T \tag{2.3}$$

In deep water, the wavelength, L is given [47]

$$L = \frac{g}{2\pi f^2} = \frac{gT^2}{2\pi} = 1.56T^2 \tag{2.4}$$

where g is the gravitational constant of 9.81 m/s^2 and f is the frequency of the wave.

The intermediate and shallow water depths can also be described. Table 2.1 gives classifications for wave depths where shallow waves are less than L/20 and intermediate water is less than 0.5 L [48]; however, there is also reporting of shallow water being less than L/4 [49].

Table 2.1. Classification of ocean waves.

D_{rw} **(Range)**	**Classification**
< 0.05	Shallow water waves
0.05 - 0.5	Intermediate depth waves
> 0.5	Deep water waves

The wavelength variation was tested in a micro wave-tank constructed in The University of Glasgow. The tank is shown in Fig. 2.4 and the results are given in Fig. 2.5. In shallow water, if the depth d is less than a quarter of the wavelength L then the velocity is

$$V = \sqrt{gd} = 3.13\sqrt{d} \quad \text{m/s} \tag{2.5}$$

so that the wavelength in shallow water becomes

$$L = \frac{\sqrt{gd}}{f} = \frac{3.13\sqrt{d}}{f} \quad \text{m} \tag{2.6}$$

The wavelength was measured using wave probes. When the probe signals were in phase then they were one wavelength apart and this could be measured. The measured wavelengths begin to follow the shallow wavelength curve at about 2 m wavelength. For 400 mm depth then this gives a D_{rw} of 0.4/2 = 0.2. This illustrates that shallow water is being approached at higher values of D_{rw} and this will have an affect on the power available in the waves since the wave power equation is a function of the relative depth. Tests were carried out with no device in the tank. The probes were formed from two parallel metal rods and the wave-height was a calibrated as a function of the probe impedance. A Labview program was developed in order to log the wave heights. One probe was fixed and the one moved until it was in phase. The distance between the probes then gave the wavelength [49].

Fig. 2.4. University of Glasgow micro wave-tank.

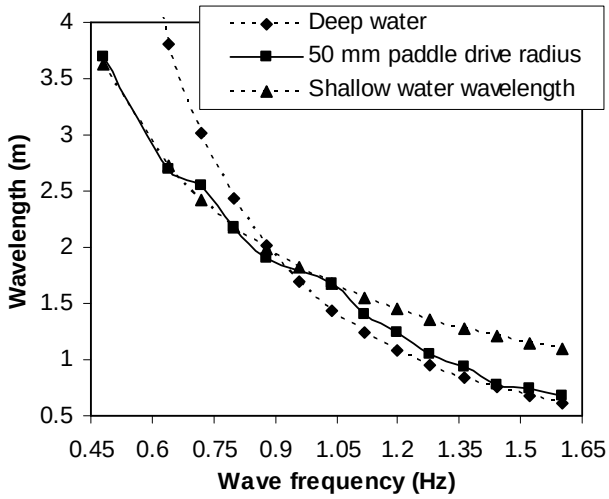

Fig. 2.5. Comparison of measured wavelengths with deep and shallow wavelength predictions for micro wave-tank. The depth is about 400 mm [50].

Returning to the analysis of deep water waves, the mean energy flux crossing a vertical plane parallel to a wave crest, i.e., the energy density of wave E_d, can be determined using the equation [51]

$$E_d = \frac{\sigma g H^2}{8} = \frac{\sigma g a^2}{2} \quad \text{J/m}^2 \tag{2.7}$$

where σ is the sea water density of 1025kg/m^3, a is the wave amplitude in m and H is the wave height in m. The wave power density P_d refers to the energy per wave period and it can be calculated by dividing the energy density by the wave period as shown in [51]

$$P_d = \frac{E_d}{T} = \frac{\sigma g H^2}{8T} = \frac{\sigma g a^2}{2T} \quad \text{W/m}^2 \tag{2.8}$$

Generally, high amplitude waves are more powerful. The wave energy can be determined by wave height, wave speed, wavelength, and water density. Using the standard equation for deep water conditions, the mean power per meter of wave front, P is [52][53]:

$$P = CE_d = \frac{\sigma g^2 H^2}{16\omega} = \frac{\sigma g^2 H^2}{32\pi f} = \frac{981.2H^2}{f} = 981.2H^2T \quad \text{W/m} \tag{2.9}$$

$$\omega = \frac{2\pi}{T} = 2\pi f \text{ rad/s} \tag{2.10}$$

where ω is the wave frequency.

The graphs based on equations (2.1), (2.4), and (2.9) are plotted and presented in Fig. 2.6. This data will later be taken into consideration when designing the wave tank to study the behaviour of the Bristol Cylinder. Overall, larger waves contain more power but wave power is not only determined by the wave height, it is also greatly affected by the wave speed, wavelength, and water density.

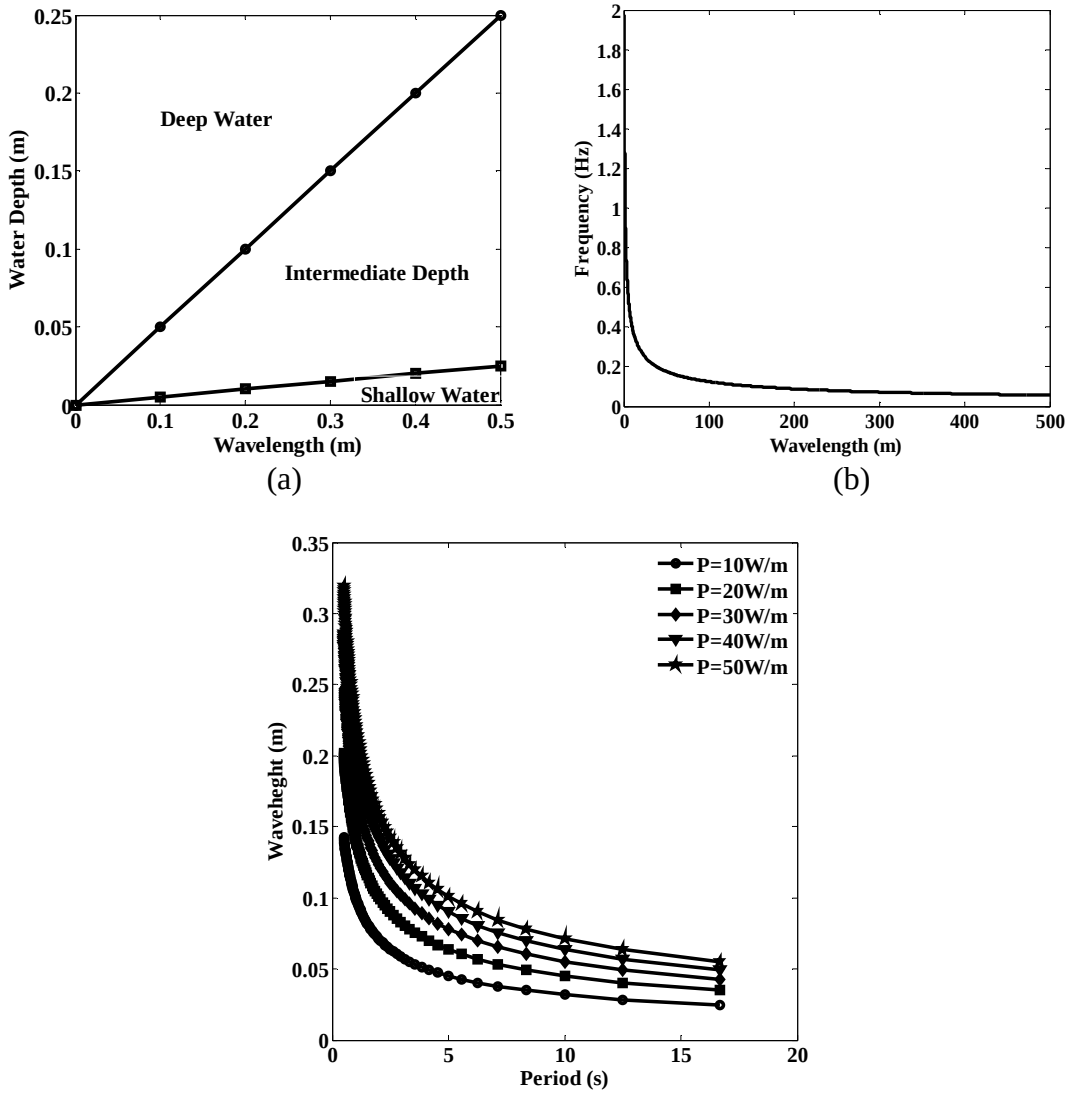

(a) (b)

(c)

Fig. 2.6. Graphs showing (a) the classification of wave based on the water depth and wavelength, (b) The relationship between frequency and wavelength, and (c) The relationship between wave-height and frequency for wave with different wave power.

2.4 Wave Characteristics

Ocean wave theory is the attempt to explain the nature of ocean waves. Because of the irregularity and instability of waves, they have different wave lengths and amplitudes that need to be analyzed; the true nature of a sea state is very complex. Local winds, ocean bottom structures, earthquakes, and storms all have their impact on the resultant waves. Waves of different frequency, magnitude and direction all exist together and are continuously crossing and interacting leading to energy transfer within the wave spectrum [41]. To explain the nature of waves in a mathematical context, it is more convenient to represent waves using linear wave equations with some assumptions.

The first recognizable mathematical solution for finite-height periodic waves of stable form was developed by Gerstner in 1802 [54]. Although Gerstner predicted the rotational movement for the velocity field, the mass transport is not predicted and the particle movements are opposite to that found in other theories. Some findings have proven that it is possible for each water particle to move in a circular orbit, and for them never to collide with each other, and for them to fill out the entire region just below the wave surface [55]. Wahlen in 2007 dealt with the possibility of a periodically-rotational two-dimensional travelling wave with surface tension [56], while Constantin and Strauss in the same year discussed large-amplitude steady-rotational gravity water waves [57]. All these theories proved that the rotational wave device can operate properly.

Linear waves are considered as small amplitude waves which can be linearised. It is assumed that they are monochromatic waves, which means only one incident wave with only one frequency can be studied at any one time. The linear theory is correct if it is assumed that the wave steepness is negligible. If the wave steepness S becomes visible (i.e., high) then non linear effects become significant in some cases, so that non linear theory will need to be considered. The wave steepness is defined by the wave height divided by the wavelength where

$$S = \frac{H}{L} \tag{2.11}$$

The simplest and the most commonly used theory is the Small Amplitude Wave Theory first presented by Airy in 1845. This theory provides equations that define most of the wave profile and do some predictions within useful limits for most practical circumstances. The Airy wave model also proposes a sinusoidal profile in deep water which can be modelled by mathematical equations [58]. To apply this theory, few main assumptions are required [59][60]:

- The water is homogeneous and incompressible, and surface tension forces are negligible.
- The water is nonviscous and irrotational.
- The water depth d is uniform. This means the sea bottom is stationary, impermeable and horizontal. Thus, not adding or removing energy from the flow or even reflecting wave energy.
- The pressure along the air sea interface is constant. No pressure is exerted by the wind and the aerostatic pressure between the wave crest and trough is approximately the same.
- The wave height is small compared to the wave length and water depth.

The following dimensionless parameter, called the wave number, is often used in equations defining the wave characteristics:

$$k = \frac{2\pi}{L} \tag{2.12}$$

The surface wave elevation η is the height of the water particle which is elevated above or below the still sea level. According to the linear small amplitude wave theory

$$\eta = a\cos\left(kt - \omega t\right) \tag{2.13}$$

where t is the time.

The horizontal particle velocity u is expressed as

$$u = \frac{2\pi a}{T} \frac{\cosh\left[k\left(z+d\right)\right]}{\sinh\left(kd\right)} \cos\left(kx - \omega t\right) \tag{2.14}$$

where z is the water particle distance, which is the vertical distance from the still water level. z is positive when in it above the still water level and negative when the water level is below still water level.

The vertical particle velocity w is

$$w = \frac{2\pi a}{T} \frac{\sinh[\left[k\left(z+d\right)\right]}{\sinh\left(kd\right)} \sinh\left(kx - \omega t\right) \tag{2.15}$$

while the horizontal particle acceleration $\dot{u}$ is defined by

$$\dot{u} = \frac{du}{dt} = \frac{4\pi^2 a}{T^2} \frac{\cosh\left[k\left(z+d\right)\right]}{\sinh\left(kd\right)} \sinh\left(kx - \omega t\right) \tag{2.16}$$

and the vertical particle acceleration $\dot{w}$ becomes

$$\dot{w} = \frac{dw}{dt} = \frac{4\pi^2 a}{T^2} \frac{\sinh\left[k\left(z+d\right)\right]}{\sinh\left(kd\right)} \cosh\left(kx - \omega t\right) \tag{2.17}$$

Once the linear displacements, velocities and accelerations are defined, the dynamic pressure p is expressed as

$$p = \sigma g a \frac{\cosh\left[k\left(z+d\right)\right]}{\cosh\left(kd\right)} \cos\left(kx - \omega t\right) \tag{2.18}$$

While the Small Amplitude Wave Theory has certain limitations, particularly related to the water depth, Stoke's second order theory can be applied to deep water waves moving towards being the shallow water waves [61]. The equations for Stoke's second order wave theory are listed below [42][62].

From Stoke's second order theory, the surface elevation η_s becomes

$$\eta_s = \frac{H}{2}\cos(kt-\omega t) + \frac{H^2\pi}{8L}\frac{\cosh(kd)}{\sin^3(kd)}\left[2+\cosh(2kd)\right]\left[\cos\left(2(kx-\omega t)\right)\right] \tag{2.19}$$

The horizontal particle velocity u_s is

$$u_s = \frac{H\pi}{T}\frac{\cosh\left(k(z+d)\right)}{\sinh(kd)}\cos(kx-\omega t) + \frac{3H^2\pi^2}{4\pi L}\frac{\cosh\left(k(z+d)\right)}{\sinh^4(kd)}\left[\cos\left(2(kx-\omega t)\right)\right] \tag{2.20}$$

and the vertical particle velocity w_s is

$$w_s = \frac{H\pi}{T}\frac{\sinh\left(k(z+d)\right)}{\sinh(kd)}\sin(kx-\omega t) + \frac{3H^2\pi^2}{4\pi L}\frac{\sinh\left(2k(z+d)\right)}{\sinh^4(kd)}\left[\sin\left(2(kx-\omega t)\right)\right] \tag{2.21}$$

The horizontal particle acceleration $\dot{u}_s$ can then be denoted by

$$\dot{u}_s = \frac{2H\pi^2}{T^2}\frac{\cosh\left(k(z+d)\right)}{\sinh(kd)}\sin(kx-\omega t) + \frac{3H^2\pi^3}{T^2L}\frac{\cosh\left(2k(z+d)\right)}{\sinh^4(kd)}\left[\sin\left(2(kx-\omega t)\right)\right] \tag{2.22}$$

while the vertical particle acceleration, $\dot{w}_s$ becomes

$$\dot{w}_s = -\frac{2H\pi^2}{T^2}\frac{\sinh\left(k(z+d)\right)}{\sinh(kd)}\cos(kx-\omega t) - \frac{3H^2\pi^3}{T^2L}\frac{\sinh\left(2k(z+d)\right)}{\sinh^4(kd)}\left[\cos\left(2(kx-wt)\right)\right] \tag{2.23}$$

Again, after defining the linear displacements, velocities and accelerations, the dynamic pressure, p_s is expressed as:

$$p_s = \frac{\sigma g H}{2}\frac{\cosh\left(k\left(z+d\right)\right)}{\cosh\left(kd\right)}\cos\left(kx-\omega t\right) + \frac{3\pi\sigma g H^2}{4L\sinh\left(2kd\right)}\left[\frac{\cosh\left(2k\left(z+d\right)\right)}{\sinh^2\left(kd\right)}-\frac{1}{3}\right]\left[\cos\left(2\left(kx-\omega t\right)\right)\right] \quad (2.24)$$

Using the equations above, as set of waveforms can be developed to compare the sea wave representation. These are plotted and presented in Fig. 2.7 for the velocities and vertical displacements. Fig. 2.8 shows the acceleration and pressure waves.

Overall, both theories provide similar values for the wave parameters in deep water condition. However, the differences are clearly observed in the vertical particle velocity and dynamic pressure. In contrast to linear small amplitude theory, Stokes theorem states that the phase velocity of sea waves depends on the wave amplitude due to the non-linearity of the waves. The parameters used to plot the graphs are shown in Table 2.2.

Table 2.2. Wave parameters.

Parameters	**Value**		**Parameters**	**Value**
Gravity, g	9.81 m s^{-2}		Wave Period, T	1 s
Water Density, σ	1025 kg m^{-3}		Water Particle Distance, z	0 m
Wave Height, H	0.15 m		Wave Amplitude, a	0.075 m
Water Depth, d	0.75 m			

In summary, waves travel as propagating wave of potential energy. Kinetic energy is needed to set up a rotating motion in the water. Within the framework of Airy wave theory, the orbital motions are circles in deep water and ellipses in finite depth. The Bristol cylinder wave device harvests energy from the propagating wave of potential energy formed by the sea wave. The power in the wave is a function of the square of the wave height and proportional to the wave period.

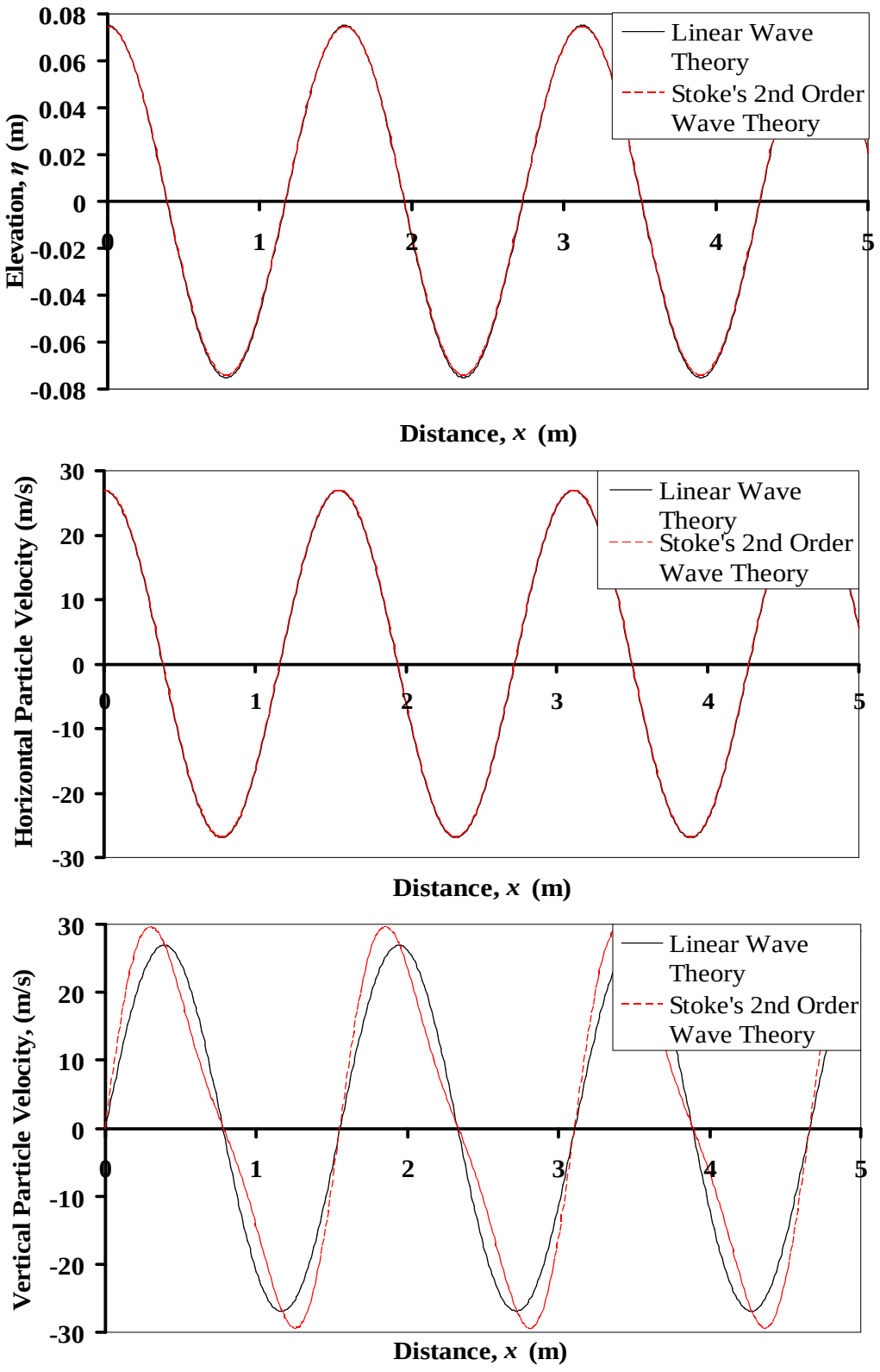

Fig. 2.7. Graphs showing the wave parameters comparisons between Linear Wave Theory and Stokes 2nd Order Theory. From the top, the wave elevation, the horizontal particle velocity, and the vertical particle velocity.

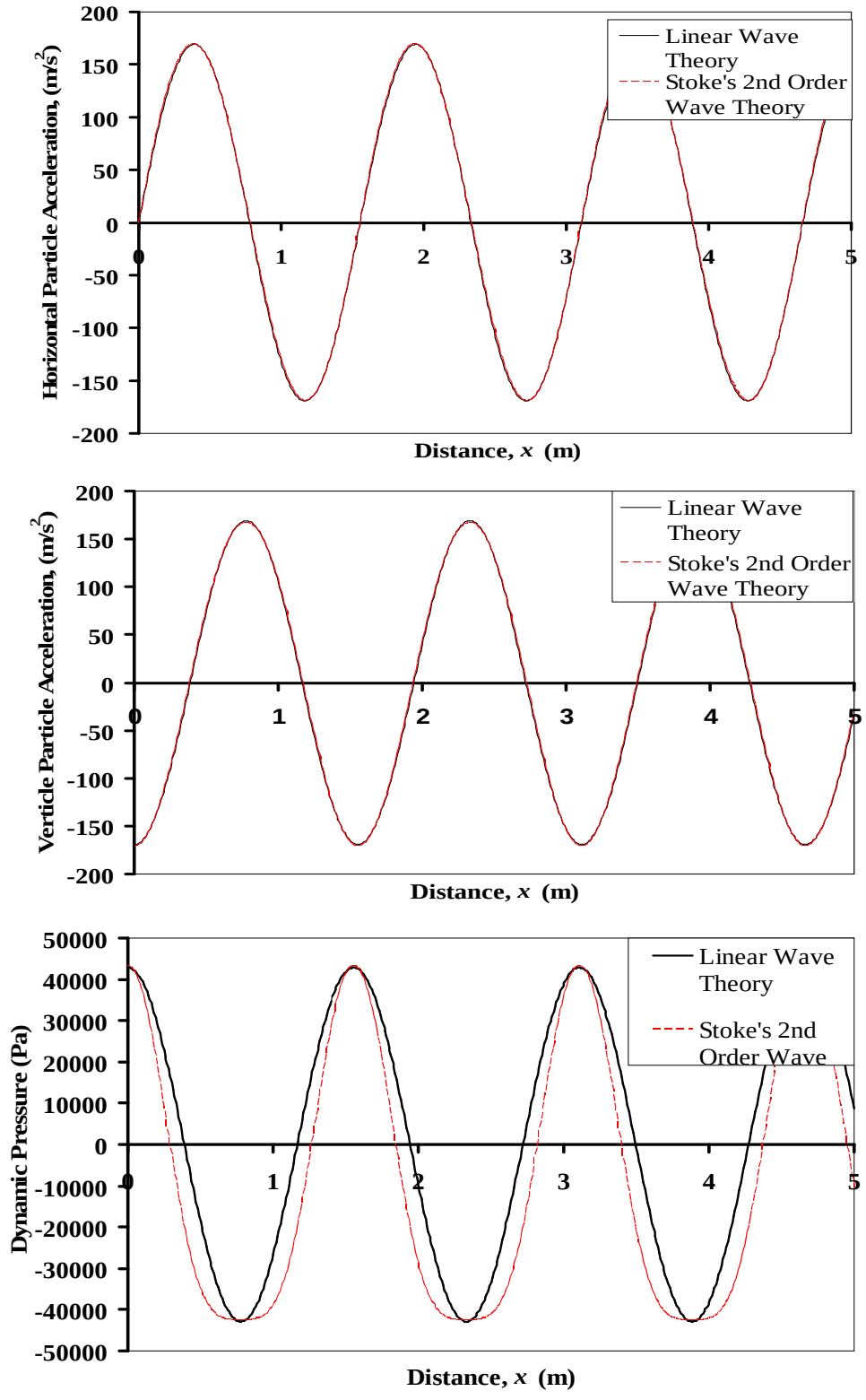

Fig. 2.8. Graphs showing the wave parameters comparisons between Linear Wave Theory and Stokes 2nd Order Theory. From the top, the horizontal particle acceleration, the vertical particle acceleration, and the dynamic pressure.

2.5 Wave Energy Devices

Modern day research on wave energy devices can be traced back to between 1970 and 1980 when several governments started initiatives in response to the oil crisis at that time. Throughout the 1980s, many of the research projects were stopped or reduced in scale due to several issues and problems encountered. These were both political (with cheaper oil and nuclear power) and technical (reliable power electronic energy conversion was still being developed and relied on thyristor technology, and also new forms of materials suitable for light-weight low-cost high-strength turbines were still being developed). Recently, a number of small companies have tried to develop and commercialize a range of varying wave energy devices, and promote the devices as a non-polluting source of energy. The research in this field is now receiving increasing amounts of funding from various governments and related organizations.

The functions of a sea wave energy device are to harness the energy of sea waves and convert the energy into useful forms of energy for domestic or industrial use. It is therefore known as wave energy converter. There are several significant reviews of wave energy devices which describe and discuss the various forms of device developed which attempt to harness sea wave energy. Basically, wave devices can be categorized into several types of device; These categories are:

1. The OWC.
2. The point absorber.
3. The flap or surge device.
4. The attenuator or contouring device
5. Overtopping devices.
6. Other types that are unique and do not fall into any category above.

The OWC operates much like a wind turbine, applying the principle of wave-induced air pressurization in an enclosed chamber. It has a semi-submerged structure forming an air chamber with a top outlet though which reciprocating airflow flows through it; this drives the bi-directional turbine. As the incidents wave surface rise inside the chamber, the air will be compressed and go through the top outlet. Some

examples of OWCs and component bidirectional turbines are the Limpet and the Breakwater Turbine developed by Wavegen [63][64], the Denniss-Auld Turbine developed by Oceanlinx [64], the Ocean Energy Buoy developed by Ocean Energy Ltd.[66], the OWC developed by SeWave Ltd. [67], and several others. They are a relatively simple device to construct in terms of prototyping, hence their popularity.

Point absorbers refer to a buoy that is small relative to the wavelength of the waves, and floats at or near to the wave surface. Wave energy from all directions can be absorbed by the vertical movement of the buoy as the waves pass. Depending on the configuration of the resistance, the power take-off and the type of device-to-shore transmission, the resistance can be in various forms. Examples of point absorber wave devices are the PowerBuoy by the Ocean Power Technologies [68], the CETO by Carnegie Wave Energy [69], the Linear Generator by Seabased [70] and several others.

Surge wave devices harness energy from the horizontal movement of the water particles in waves. They are normally situated in shallower water and close to shore. In shallow water, the circular movement of the water becomes elongated into horizontal ellipses. Examples for this form of device are the Oyster by Aquamarine Power [71], the WaveRoller by AW-Energy [72] and others.

Attenuator/Contouring devices are elongated floating devices that are parallel to the wave direction. When incident wave propagates along the device, movement within the device is generated which produces energy. Examples are the Pelamis by Pelamis Wave Power [73], the Wave Star by Wave Star Energy [74], the Anaconda by Checkmate Seaenergy [75] and others.

Overtopping devices rely on using a funnel or barrage arrangement on the device to elevate part of the incident waves above the mean sea level to fill a raised reservoir. The seawater returns to the sea via a low-head turbine. Examples of this device are the Wave Dragon by Wave Energy AS [7], the Multiple Stage Overtopping Device by Wave Energy [76] and others.

Some of the wave energy devices need gears and hydraulic systems to generate electricity, while some are direct drive wave energy devices [77]. The wave

devices each have their own advantages and disadvantages when compared to the others. The Bristol cylinder device falls under the sixth category because it is considered a unique and direct drive device. This will be the device under study for this research and will be further describe in the next section.

2.6 Bristol Cylinder Wave Energy Devices

The Bristol Cylinder wave device that is studied here does not come under any of the categories discussed above. It is a semi-submerged device that is marginally buoyant which rotates synchronously with the incident wave, given an appropriate speed control. The wave power absorption characteristic of a submerged cylinder was studied in [15] and [31], and these proved that power generation by such a device is feasible and worthy.

The dynamic behaviour of the wave energy conversion system needs to be analysed in order to quantify the rotational motion of the Bristol Cylinder when driven by the waves. As mentioned earlier, the kinetic energy transmitted to the Bristol Cylinder by the potential and kinetic energy of the sea wave passing produces a rotational motion. Therefore, the rotational torque can be utilized as the driving torque for the electrical generating system within the Bristol Cylinder system. The torque depends on rotational velocity which is related to the properties of the sea waves, i.e., the wave height and period. If power increases with wave period then this means that the power in the device increases as the cylinder rotational velocity decreases. This is an interesting issue for the electrical power train because in rotating electrical machinery, there is usually a torque limit so that power increases with velocity, not decreases. This represents a challenge electrical energy conversion system within the device.

For the study of the system motion, a monochromatic sinusoidal wave model is used. Two main theories, the Small Amplitude wave theory and Stokes Second Order wave theory, will be studied for the monochromatic sinusoidal wave modelling. In order to maximize the energy produced, the motion characteristics of the system have to be considered and analyzed. The rotational behaviour of the cylinder depends on the incident waves. It can be observed that the efficiency of the energy conversion

process performed by the cylinder only reaches an optimum level when the cylinder and incident waves are synchronized and there is appropriate wave height. The rotational cycle period has to be near to the period of the incoming waves bearing in mind that the waves themselves, in a real sea state, will be constantly varying in height and period with an approximate mean frequency. The efficiency of energy conversion will change according to the incident wave frequency and height. Hence, real sea wave conditions are far from ideal for energy exploitation because the actual motion of waves is very unpredictable. In other words, it is more desirable to control the Bristol Cylinder to react according to the incident wave rather than choosing the device to function only at a specific wave frequency and wave height because it will reduce considerably (possibly to zero if unsynchronized) the total amount of the energy produced during a period of time characterized by a variable wave motion. This is similar to a synchronous machine, which needs to rotate synchronously with the supply frequency and the excitation is similar to the wave height in its role. The radius of cylinder rotation will vary with wave height and this issue is solved with a flexible dual-armed Bristol cylinder that is able to change its rotational radius. This is illustrated in Fig. 2.9. As already stated, the basic idea is to adjust on the rotational period of the cylinder to the period of the waves. In this way, it will be possible to maximize the energy conversion from a large range of wave frequencies and heights. From the technical point of view, it is difficult to realize a system for flexible arm because the marine environment is a hostile location and not compatible with the mechanical complexity of such a system. Hence it is still under development. Fig. 2.9 shows a mechanical armature system although in [13] an artist's impression shows the cylinder anchored using four hydraulic or pneumatic variably-linear actuators. This is not an unrealistic option – the Pelamis [73] used hydraulic actuators on to give resistive hinging between its sections.

The result of the procedure is that both the rotational radius of the Bristol cylinder and momentum of inertia will need to be continuously adjusted for successful operation. With a flexible arm characteristic as part of the cylinder arrangement, it is possible to obtain the desired period and radius of rotation of the sea wave energy converter. A prototype is being developed and a basic arrangement is shown in Fig. 2.9. Fig. 2.10 shows the basic working principle of the wave device. Assuming the incident wave comes from the left to the right, the position of the vertical slider will

be set, the rotational radius will be calculated and the position of dual arm locked, and the Bristol cylinder will rotate clockwise in circular motion. More details about the working principle of the Bristol cylinder will be explained and shown in section 4.2 later in the thesis. The prototype device as initially developed by Green Cat Ltd. and unsuccessfully tested is shown in Fig. 2.11. This shows a very high gearing mechanism (greater that 10: 1 step up) to drive a small DC machine (floor, bottom right). This turned out to be a consistently weak point in the system.

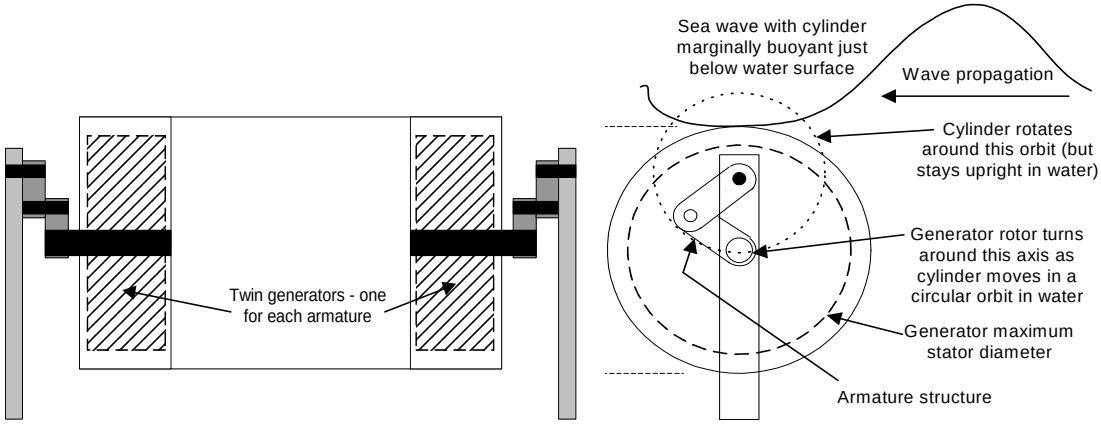

(a) (b)

Fig. 2.9. Bristol cylinder arrangement – (a) front view (facing waves) and (b) side view.

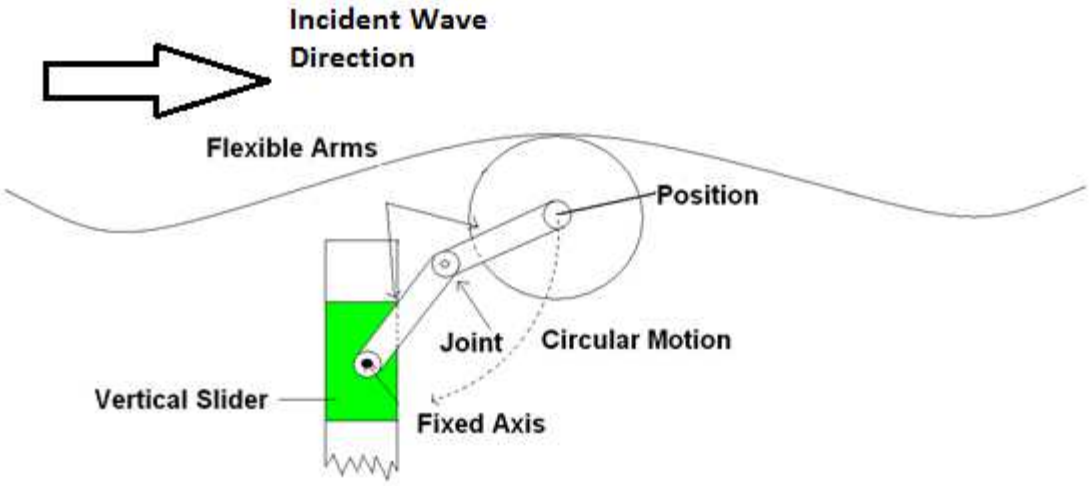

Fig. 2.10. Dual arm Bristol Cylinder.

Fig. 2.11. Green Cat prototype (10:1 gearing in cylinder and DC machine).

The moment of inertia J of a Bristol Cylinder rotating just below the sea surface can be treated as a solid cylinder rotating about an external axis. This gives

$$J = m\left(D_c^2 / 8 + r^2 \right) \tag{2.25}$$

where D_c is the cylinder diameter, r is the rotational radius and m is the cylinder mass.

The simulations in this study will use three sizes of device. There is a small size of device that is simply used in a micro wave tank for cross checking cylinder device, its movements and functionality. There is the Green Cat prototype. This size of device is used for the simulation work which constitutes the largest contribution to this study. Finally there is a full sized device used for costings and simulations in the next section. These will be related to a sizing exercise later in this chapter.

2.7 Proposed Wave Tank Design

In order to probe the performance of micro systems, including the Bristol Cylinder, a basic arrangement for a micro wave tank is constructed at The University of Technology Sydney. An initial design is shown in Fig. 2.12. This was a similar arrangement to that originally constructed at The University of Glasgow and uses an overtopping beach. Earlier, the wave measurements are taken from the wave tank in The University of Glasgow.

For this newly proposed wave tank, a length of 2*L* is chosen from the paddle to the cylinder to make sure only completed wave reach the Bristol Cylinder so that a length of greater than about 4*L* or more is needed for the paddle to beach. This distance should be large to avoid wave reflections from the cylinder to paddle and from beach to cylinder; these will cause turbulence and interference with other waves. Ideally there should be no reflected waves. The lack of these will make the waves more monochromatic and increase the accuracy of the experiment. The width can be set to about 1 m since the wave power is always calculated for 1 m wavelength. It is also advantageous to conduct experiments in a 2 dimensional plane with no end effect, which will greatly reduce the complexity especially when it involve generator, a wave tank width of 0.5 m can be considered as well.

Initial construction photos of the system are shown in Fig. 2.13 and drawings of the system are included in Appendix 1. This wave tank is constructed at The University of Technology Sydney. There are limitations to the size of the wave tank in the given area but it is aimed at being able to give 100 mm waves at 1 Hz. The system was used to test the behaviour of a simple cylinder as shown later.

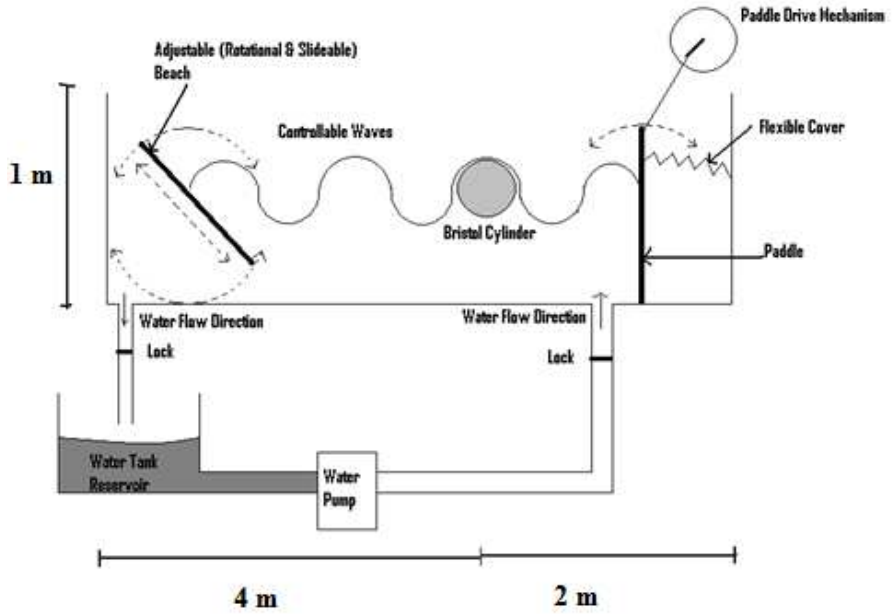

Fig. 2.12. Proposed wave tank design.

Fig. 2.13. UTS Micro wave tank construction.

2.8 Device Scaling

The device scaling is an important part in this research as it is impractical to build the sea going device directly. It is more practical to construct a small scale device. However, the performance of the small scale device can be scaled to study the performance of the sea going device. The scaling of the device performance can be done using the Froude number.

The Froude number is defined by [78]:

$$F_R = \sqrt{\frac{\text{inertial force}}{\text{gravity force}}} = \sqrt{\frac{\sigma D^2 V^2}{\sigma D^3 g}} = \frac{V}{\sqrt{Dg}} \tag{2.26}$$

where V is the wave velocity. We can neglect the viscous effects which are negligible [78]-[79]. For similarity of the two conditions the relationship should be satisfied:

$$\frac{V_l}{\sqrt{D_l g_l}} = \frac{V_{FS}}{\sqrt{D_{FS} g_{FS}}} \tag{2.27}$$

where the suffix *l* is the laboratory model and the suffix *FS* represents the full sized device. These are used through the analysis below. It is assumed that the gravitational acceleration is the same [80].

The mean average wave speed in the cross section of the full scale device should be used for calculation of the Froude numbers [81]. The water depth is the major factor to distinguish the two conditions and thus the geometric scaling factor λ is defined by:

$$\lambda = \frac{D_l}{D_{FS}} \tag{2.28}$$

From (2.27) and (2.28), and from [82], the scaling factor for the wave periods is

$$\frac{T_l}{T_{FS}} = \frac{V_l}{V_{FS}} = \sqrt{\frac{D_l}{D_{FS}}} = \sqrt{\lambda} \tag{2.29}$$

while the scaling factor for the wave surface elevations is:

$$\frac{H_l}{H_{FS}} = \frac{D_l}{D_{FS}} = \lambda \tag{2.30}$$

The power is proportional to LH^2T therefore if we scale all three linear distances and the time then we find that the power scales by $\lambda^{3.5}$. Essentially λ is the linear scaling factor. However it may be that one linear direction or the wave periods are not scaled according to the Froude number.

2.9 Full Sized Prototype Costings

Fig. 2.9 illustrates these dimensions and extends the radius of rotation of the cylinder to clearly show the cylinder motion. There is considerable inertia in the cylinder; for an ocean-going device the cylinder could be 15 m in diameter and 50 m in length and marginally buoyant. From equation (2.7), it can be calculated that for a 5

MW device and 3 m 10 s waves, the power is 50 × 981.2 × 32 × 10 = 4.5 MW. In order to assess the validity of the system a first pass costing exercise was carried out as shown in Table 2.3.

The main cost of operation of such a wave energy farm will be related to the structural manufacture and installation of the device offshore. According to a report by Green Cat Renewable Ltd., in UK a unit size of 4 MW of this particular wave device will need capital cost of £6.35M for installation, and estimated operational cost of £210,000/annum. The electrical generation cost will be £100/MWh without the capital grant (£90/MWh with 10% grant). This figure shows that it is already close to competing with offshore wind energy generation of approximately £75/MWh. In the long term, it is likely to be competitive with Nuclear and other power plants although at this point, this is very subjective. The capital costs estimates are shown in Table 2.3.

Table 2.3. Cost Estimation of Installation of Commercial Wave Device (Resource: Green Cat Renewable Ltd.)

Component	**UK Price (4 MW Commercial Machine)**	**Sources**
Turbine	1,500,000	Northead Ltd
Power Take-off	250,000	Score Europe
Generation & Power Conditioning	700,000	Peebles, Alstom power converters
Towers & Control Cabin	800,000	Corus, Score Europe
Foundations	600,000	Amec
Grid & Substations	1,000,000	Scottish & Southern
Control	500,000	Trac International
Other	1,000,000	Various
Total	6,350,000	

2.10 Sea Resources

To assess the size of the full sized device it is necessary to assess real sea states and the statistical analysis of the frequency and height probability spectra. One likely location is in the North Atlantic and a significant wave height and wave

direction for the 2nd October 2011 is given in Fig. 2.14. However the significant wave period or frequency is still not given in this map.

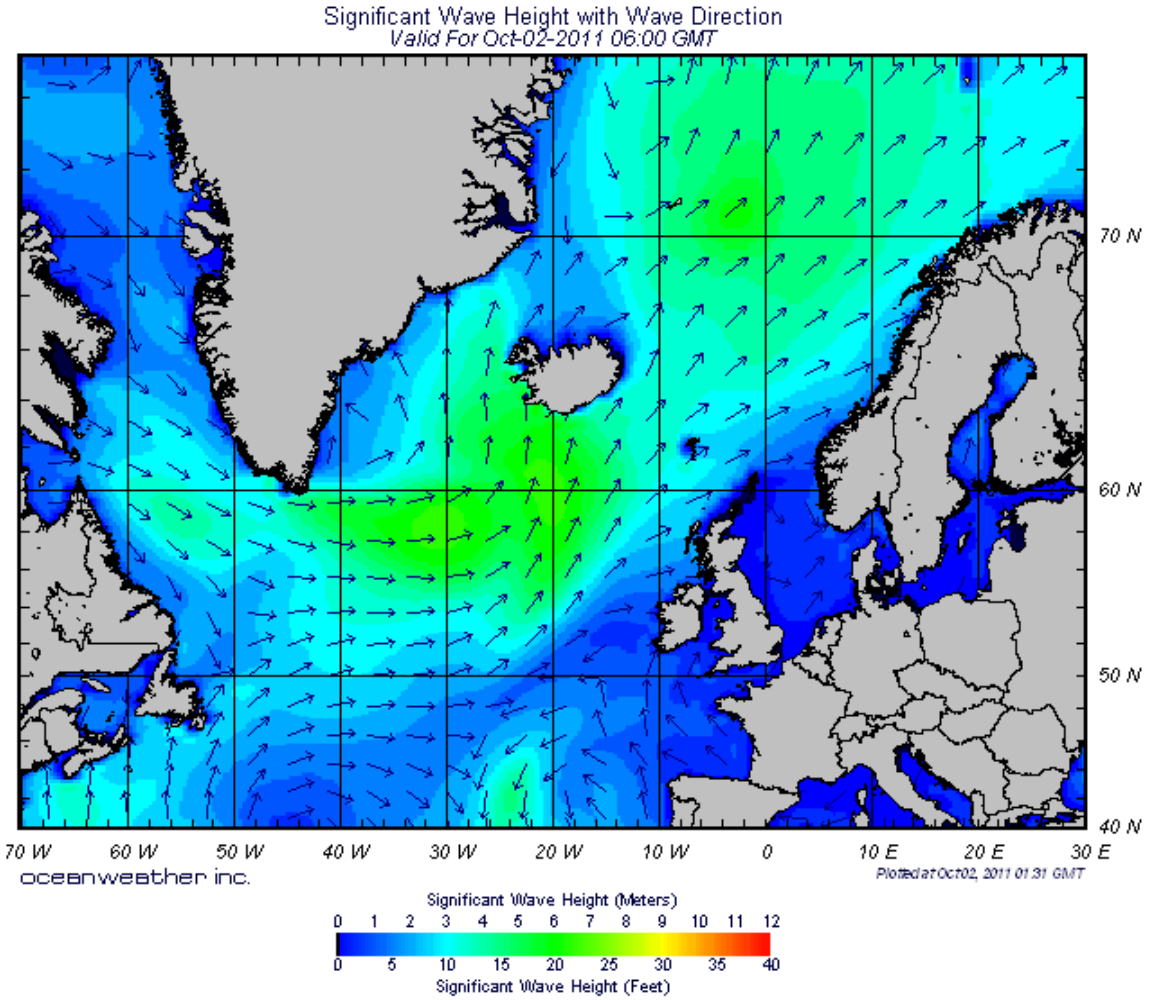

Fig. 2.14. Wave height data for North Atlantic region on 2/10/2011 (Ocean Weather Inc.).

A more detailed, and typical, plot is shown in Fig. 2.15, again this is for the North Atlantic. This shows that a reasonable rated wave device would be designed for 3 m 10 s waves. While 1-2 m 7.5 s waves are statistically more common these are lower in power and the peak power rated would be slightly above this. It is also worth looking at other locations. A second location is shown in Fig. 2.16 and this is for a location near Taiwan. This location should have lower wave energy resource and indeed, 1-2 m 7.5 s waves would appear to be a more reasonable device design point.

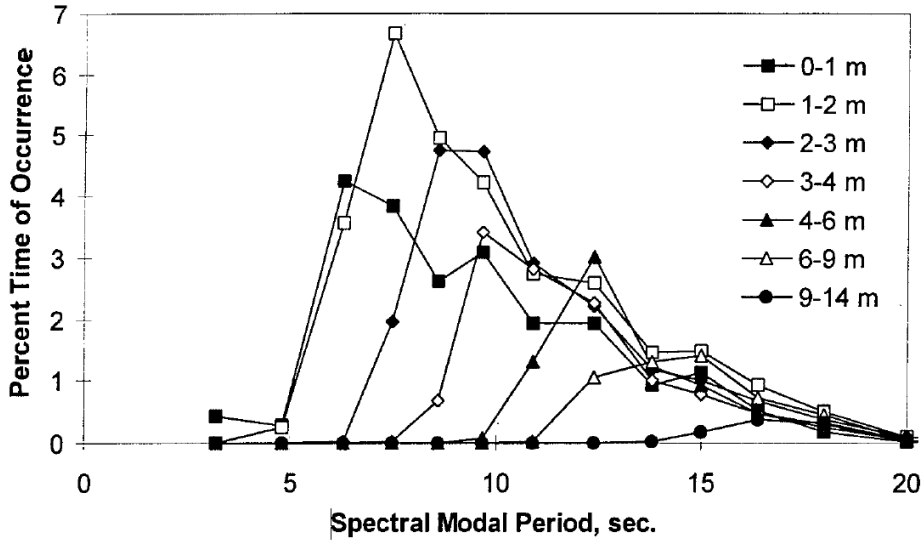

Fig. 2.15. Percent time of occurrence of spectra in the North Atlantic as a function of spectral modal period for different significant wave height bands [82].

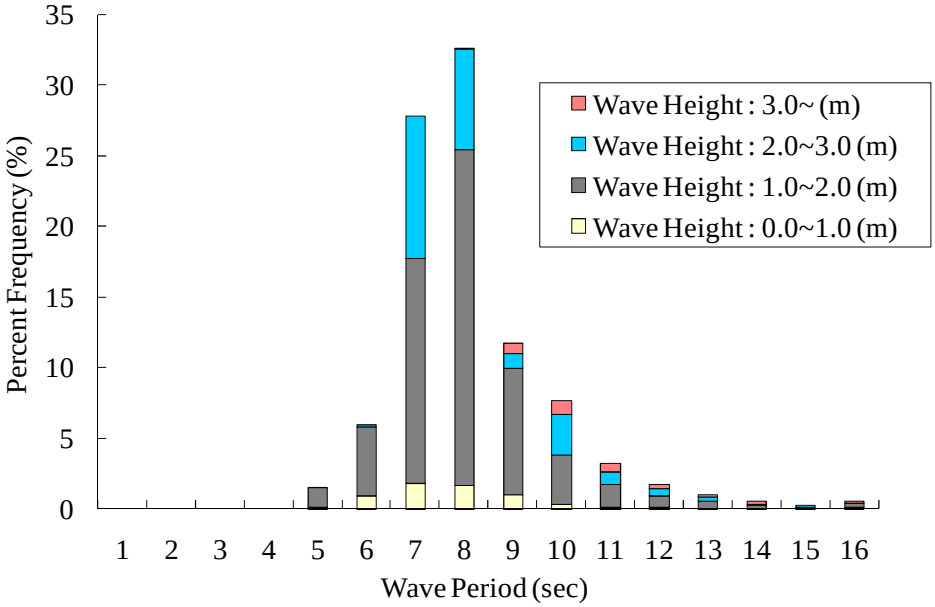

Fig. 2.16. Probability of waves of Chenggong, Taiwan [82].

With reference to the scaling procedure in the previous section we have the comparative data in Table 2.4. For the wave device with 4.5 MW as the input power, it is estimated that at 50% power conversion rate, the output power can be found as 2.25 MW. The rated torque which is the required torque to turn the wave device at the rated speed and producing the rated power can then be calculated.

Table 2.4. Comparison of small prototype and full scale device – key outline parameters.

Parameter	**Full scale device**	**Small prototype (Fig. 2.11)**
Target wave period	10 s	3 s
Target wave height	3 m	0.16 m (using ratio of diameters)
Diameter	15 m	0.8 m
λ (using diameters)	---	0.5333
Length	50 m	1.5 m (short compared to λ)
Wave power per m	90 kW/m	75.4 W/m
Device input power	4.5 MW	113 W
Output power	2.25 MW (50 % eff.)	28.3 W (25 % efficiency)
Rated torque	3581 kNm	13.5 Nm

Chapter 3

DESIGN OF A DIRECT DRIVE PERMANENT MAGNET SYNCHRONOUS GENERATOR

3.1 Introduction

Recently, the application of brushless PM machines has increased rapidly with the development of rare earth magnet and power electronic drive technology. This leads to compact and high-efficiency machines. These machines roughly lie in two groupings – brushless permanent magnet AC machines and brushless permanent magnet DC machines. The former has multi-phase sinusoidal current sets. The back-electromagnetic force (EMF) in the windings should be close to sinusoidal and if position sensing is used then a shaft encoder with high resolution is required. These machines are used in high performance servo drives and generators and their theory of operation is derived from synchronous machines, hence they are often referred to as permanent magnet synchronous generators (PMSGs). The brushless permanent magnet DC machine uses trapezoidal current waveforms and the back-EMF should be close to trapezoidal. If position feedback is utilized then this will be via Hall Effect position sensors since only the switching positions are required. The theory of operation is derived from DC machine theory. While they can give higher torque densities they can suffer from torque pulsations. They tend to be used in power drives.

In reality, many brushless PM machines have intermediate characteristics and can be used with either AC or DC control depending on the position sensing and control strategy [83]. Both types of machine can have very different types of rotor design which can use magnets on the surface rotor or interior permanent magnets (IPMs). IPMs can give advantageous characteristics in terms of additional reluctance torque components (useful for very high density and efficient drives) and extended speed operation, well into the field weakening region (useful for vehicle drives [84]).

In this application the machine is being used as a generator. The aim is to design a generator to fit into the end voids in the prototype shown in Fig. 2.9. These were initially used for a gearing arrangement and small PM machines as shown in 2.11, but these were found to be unsuccessful. By the nature of the application it was deemed that a direct-drive surface-magnet PMSG would be suitable; and that two would be needed, one for each armature. The reason for using surface magnets is that these machines are very high pole number and the precision needed for the encoder to enable full utilization of the rotor saliency would be too high. Fitting IPM magnets in narrow pole pitches is also difficult.

In this chapter the design procedure for the generators is described. This is a theoretical exercise. The prototype cylinder is a design goal. The company involved (Green Cat Ltd.) had limited resources to enable construction of what would be expensive prototypes and the priorities of the company changed as this PhD study was beginning. Therefore it was decided to continue the project as a design exercise. Before the design procedure is described, the development of brushless PM machines is discussed.

The main reasons for the growth of the brushless PM machine market are the developments in new materials with better magnetic characteristics, and the reduction of the cost and improvement in performance of the power electronic converters (as already mentioned). Brushless generators constructed with the permanent magnets have several advantages, such as minimal rotor losses, elimination of the external source required to create the rotor magnetic field (either the DC-current field winding via slip rings or brushless exciter in the synchronous machine, variable AC-current field winding via slip rings in a doubly-fed induction generator, or additional flux-vector stator magnetizing current in a cage induction generator), no commutator, larger torque per volume, minimal maintenance of the rotor (since there is no armature or slip rings), high efficiency when designed correctly with high energy rare-earth magnets, as well as several other reasons. As a result, PMSGs have been developed for different applications. These include wind turbines [85]-[87], marine devices [88]-[90], hydro power plants turbines [91]-[93] and other renewable energy fields. The disadvantage to these machines is that the field cannot be controlled leading to variable voltage operation and, by the variable nature of the speed, the

frequency is also variable too, so considerable power conditioning is required. This is usually in the form of a rectifier (controlled or diode bridge), DC link (possibly with some DC voltage control using a chopper) and a grid-connected inverter.

An electrical power system is built from many individual elements. When connected, they form a large and complex system whose functions will be to generate, transmit and distribute electrical energy over large areas for consumption. Synchronous generators are the important components of the system, where it will be the main source of electrical energy. These are still mostly standard constant-speed grid-connected embedded generators of very large size. There have been several books addressing brushless PM motor design and control [94][95] but comparatively few that address brushless PM generators [91]. However, detailed modelling and analysis of the synchronous generators has been studied from the 19th century. The theory and performance of synchronous generators have been covered in many books (e.g., [96]-[106]) spanning a considerable length of time and often within the context of power system operation. Therefore the design procedure and analysis techniques for large, low-speed PMSGs are less defined even though they have the desirable characteristics of reduced size and weight, improved efficiency (eliminating gears), easier maintenance (no brushes or gearbox) and reduced noise.

3.2 Generator Technologies

Two different generator technologies are reviewed in this section for comparison, these are the PMSG and induction generator. The discussion is limited to radial flux configurations. Axial flux configurations are not discussed here; these tend to be limited to smaller applications although there are some large examples of these in ship propulsion [107].

Induction generators are closely related to induction motors and their construction is a very mature electric motor technology [108], spanning over a century of development. Induction motors are the workhorse of industry and the generators are now extensively used in wind and hydro generation. Before the widespread use of power electronic converters, induction machines were often used as one half of the motor/generator set in a Ward-Leonard system and their role was both

as a motor and a generator. Cage induction machines (which are over 90 % of induction machines) have no internal source of excitation (the motor flux) or any external way of applying a rotor current to set up excitation. This has to come via the stator windings. Magnetic fields are related to stored energy and this in turn is related to reactive power consumption (which is the cycling of stored energy in an AC circuit). Therefore an induction motor requires reactive power to operate; hence it is inductive. To supply this reactive power, early developments in induction generators were made using fixed capacitors (as sources of reactive power) because in traditional power systems there are only two sources or reactive power – capacitors and synchronous machines; if there are no synchronous machines on the system, then capacitor excitation is required. In modern power electronics, the STATCOM is often used to control the reactive power. As a result, the power output was unstable since the excitation could not be adjusted as the load or speed deviated from the nominal values. Hence it was not a popular way of generating electricity. With the higher availability of high power switching devices today, the induction generator can provide stable power with the use of adjustable excitation control and operate in stable manner with appropriate controls.

The induction generator also consists of two electromagnetic components (as with all rotational electrical machines) which is the rotor and the stator. The rotor is obviously the rotating component. For a cage machine, it is formed from a high conductivity cage structure of high strength bars located in a slotted laminated iron core to form a squirrel cage. It can be formed from copper bars that are inserted into the slots and end-rings brazed on, or it can be cast in aluminium or (more lately), copper. Large machines tend to have fabricated rotors while small machine are often cast. The stator is formed from slots where the winding is inserted. This is usually a three phase winding although single phase machines are very common for small pump drives. The slotted nature of the stator and distributed winding are similar to the PM machine in terms of fabrication although the theory of the winding arrangement can be very different, particularly compared to a fractional-slot brushless PM machine. Fig. 3.1 shows the cross sectional view of a typical induction generator.

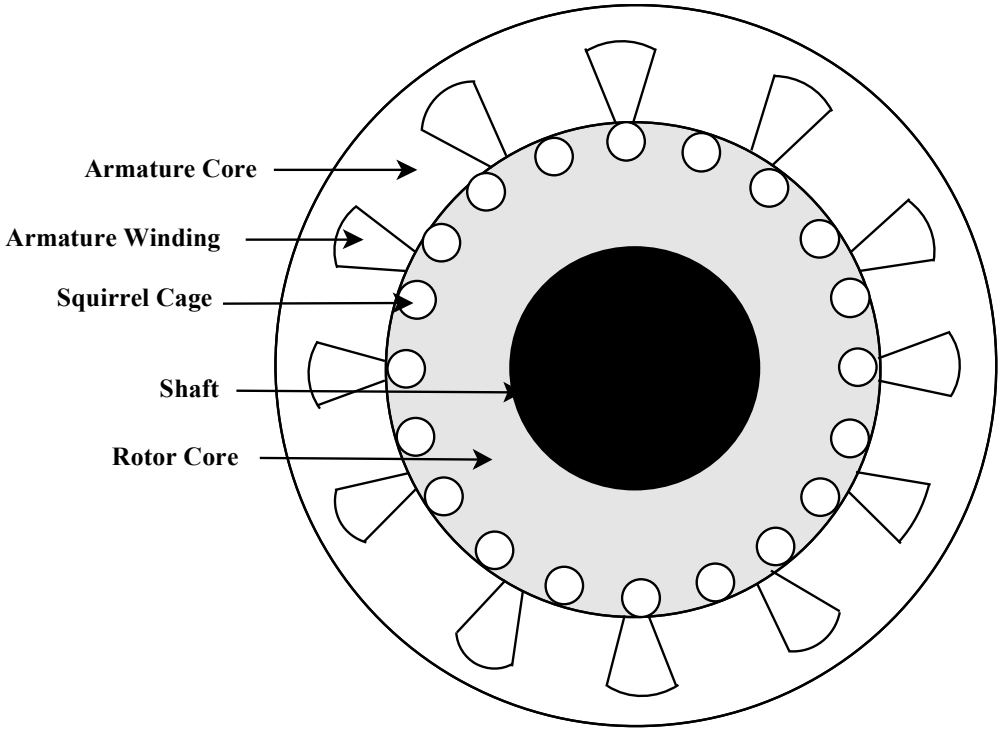

Fig. 3.1. Cross sectional view of induction generator.

For an induction generator, as already discussed, the voltage and frequency output have to be regulated. Invariably they are three phase machines, even if they are not directly connected to the grid.

If the machine is grid connected, the control of the voltage is via closed loop operation where the terminal voltage and torque are adjusted to generate constant output voltage and frequency regardless of variations in speed and load. The magnitude and frequency of the excitation current is determined by the control system. However, operation at high slip is inefficient so the speed range for grid-connected cage induction generators is very narrow (often less the 1 % from the synchronous speed) so they are effectively fixed speed generators and often fixed load. The only advantage they offer over a synchronous machine is that they do not need synchronizing and separate field control.

If the machine is not grid connected then this allows variable speed and load operation. This is a more modern use of the induction generator. This means the frequency, and hence the speed (because the machines should operate close to the synchronous speed), is free to vary. The usual constraint if the voltage/frequency

characteristic is linear up to the speed where field weakening is used (to extend the operating speed range). This requires current control both in terms of magnitude and phase (hence the use of strategies such as flux vector or direct torque control). Speed and current feedback are both required. In this form the induction generator represents an alternative option to PM generator operation or variable speed synchronous machine operation. All of these options require extensive power electronic converter control.

To reduce the size of the required converter then doubly-fed induction generators (DFIGs) are often used in applications such as wind turbines. The stator winding is now grid connected but the rotor is wound (with a similar three-phase winding) rather than cage-type and the converter is connected to only the rotor windings via slip rings. In this way the converter transmits about 25 % of the generated power. These machines do have a reliability problem due to the slip rings.

Low speed machines require a high pole number otherwise the frequency of winding flux linkages is low which means the induced voltage will likewise be low unless prohibitively high coil turns are used. In addition multi-pole induction generators have low magnetizing reactance so the power factor is poor. In practical terms the stator slots per pole also tends to be low due to the small pole pitch. This means that it is hard to realize a winding that has low spatial harmonic content. This is very important in an induction machine. If there is a high spatial harmonic content then the machine will have poor operating characteristics since the winding harmonics will interfere with torque production. However, for brushless PM machines there is not the same requirement to have a winding with low harmonic content. Indeed, fractional-slot windings, as found in many brushless PM machines, can have sub-harmonics too. Sub-harmonic current frequencies appear when the system is generating frequencies which are less than the system frequency. These will not interfere with torque production. They will affect the leakage reactance which will be in series in the circuit (affecting the power factor), although for a surface magnet machine, the effective air-gap length is high so the reactance is low. Therefore, generally, induction generators for low-speed direct-drive applications are seldom used [109] and PM machines are the only real alternative.

The PMSG consists of two electromagnetic components. The rotor is the rotating magnetic structure. The permanent magnets set up a rotating magnetic flux wave that rotates synchronously with the rotor. The stationary stator is constructed from electrical steel laminations and the windings are inserted in the slots. There are not the same constraints on the winding arrangement so that often there is not an integral number of slots-per-pole or pole-pair. Fig. 3.2 shows the cross sectional view of a typical radial flux permanent magnet generator (PMG).

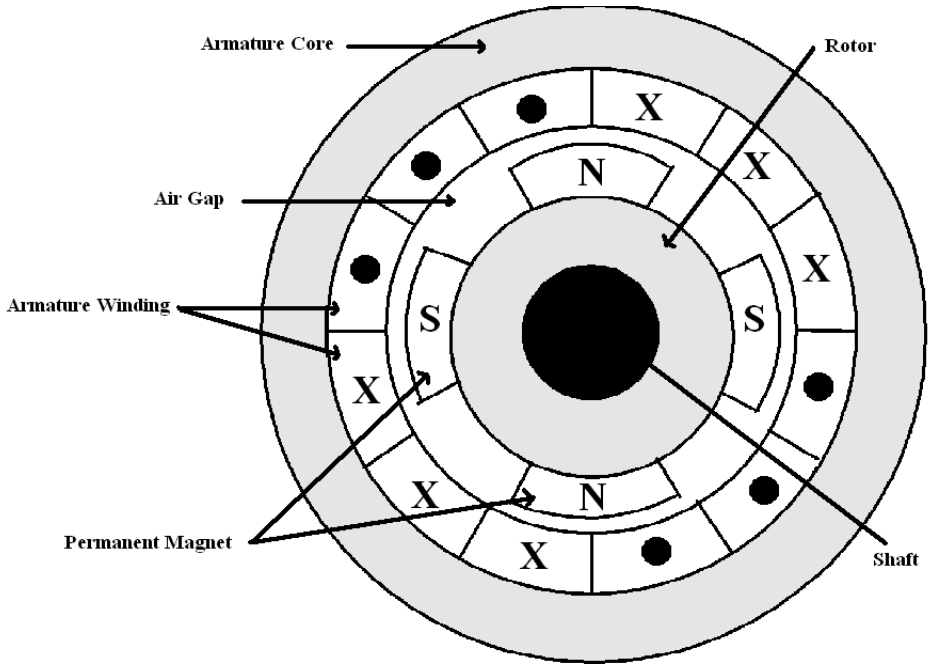

Fig. 3.2. Cross section view of radial flux PMG.

Older PMSGs were manufactured using ferrite magnets but these are low energy magnets and they can be easily demagnetized. In modern PMSGs, higher energy magnets are used. The permanent magnets are manufactured using high energy rare earth materials such as NdFeB or Samarium Cobalt (SmCo). Retention of the permanent magnets on the rotor can be an issue. They are either glued or high strength metallic or composite containment rings can be utilized. The stator core is made from laminated electrical grade steel. Usually the copper loss dominates although for high frequency operation (often in the flux weakening region) the iron loss can be an issue where the steel grade needs to be carefully addressed. The electrical windings are made from high purity copper wire conductors which are coiled and insulated from one another and from the iron core using enamel coatings (often called electrical varnish) and slot liners (made from material such as Nomex). This winding system is

suitable for low voltage windings. The entire stator assembly is impregnated using high temperature resin or epoxy. In high voltage machines the winding system is more sophisticated. The conductors are rectangular and formed into a rigid coil. The conductors are taped, held in a fixed position and encapsulated in resin to maintain an insulating distance. They are slid into slots (which are totally open) as a complete rectangular-section coil side; there will be a corona screen. There are not many PMSGs that require this sort of winding system. The voltage output of the generator is unregulated AC and usually there are three phases. The voltages will vary according to the speed and load. In the normal case, the voltage output is connected to a power electronic conditioning system before being transmitted or distributed.

Low speed PMSGs have been used in wind turbines [110][111]. Generally, multi-pole synchronous generators are recommended for low speed operation but these can be wound field machines as well as PM machines. Generator systems that utilize multi-pole wound rotors are manufactured by Enercon, Germany [112] and M Torres, Spain, although this form of generator is still not widespread. As already discussed, in a low speed generator, permanent magnets are usually utilized because of the high magnetic field (or effective field ampere-turns). The increased efficiency due to this high energy field and reduced thermal problems (since there are no rotor currents) on the rotor side are the consequent characteristics that relate to the increasing popularity of this form of machine. Currently, PMG systems are being manufactured for on-shore applications. Examples of these are the Leitner generators in South-Tyrol, Italy [28] (this reference claims that the M Torres generators are PM but investigation on the manufacturers website suggests they are wound rotor synchronous machines), the Siemens generator in Scanwind, Norway [113] (bought by GE in 2009 – the GE 4.1 – 113 4 MW wind turbine is the first wind turbine to be specifically design for off shore use), Lagerwey generators, Netherlands [114] and Innowind, Saarbruecken, Germany [109] (this company is really involved in technology innovation rather than commercial wind turbine manufacture). The normal design for PMSG rotors utilizes surface-mounted permanent magnets with distributed three phase stator windings, with either an inner or outer rotor. The stator yokes are quite thin and the active mass is low in these machines due to the high pole number. A good review of the various geometrical properties for low speed wind turbine generators is given in [115]. Most of these generators are of the inner rotor design.

PMGs do not require magnetising current in the constant torque region and this increases the efficiency and yields a higher power factor compared to the induction generator. In the field weakening region the stator currents can be used to weaken the field by use of phase advance. The PMSGs eliminate the use of slip rings or brushes. This improves the reliability of the generator. For generators with equivalent power output, the use of permanent magnets tends to reduce the weight of the generators. This leads to increase in the torque to inertia ratio and increase in the power density.

Rare earth magnets are costly and magnets can suffer from corrosion and demagnetization under fault conditions; this will not happen for the induction generator. Induction generators are generally robust and inexpensive. In addition to the issues discussed above, another disadvantage of the induction motor generator is that the generator size tends to be larger compared to an equally rated PMSG. The control is quite complicated and expensive too. Comparisons between the PMSG and the induction generator have been made by several researchers [94][116][117]. This further underpins the choice of the PMSG over the induction generator. The aims of designing a PMSG for this application are to design a low cost, eliminate the need for a gearbox, increase the efficiency of the drive, lower the cost of the turbine maintenance, and produce a high performance and light weight generator. Since the rated speed is low, a large diameter and high pole number machine is required. This will require a large amount of magnet material which will impact on the cost.

Under the category of PMSG, slotless PM generators have been developed. High energy rare-earth magnets mean that the air-gap can be large and this facilities the use of air-gap windings. The slotless machines eliminate the rotational cogging torque and can decrease the core losses. As a result, they can increase the generator efficiency and provide a good torque to volume ratio; it also produces a linear current versus torque relationship. Slotless generators can reduce the noise and vibration as well. They also allow more magnet surface area to drive the flux across the relatively large air-gap [118]. Because of the large air-gap they tend to have low stator inductance and the inertia is higher than an equivalently rated slotted machine due to more PM material in the rotor (this is useful for mechanical energy storage). The disadvantages of this type of stator winding are that there is more eddy current loss in

the windings which can necessitate the use of very thin wire (Litz wire) and it can be difficult to wind. If the frequency is low then this may not be an issue. There can also be a restriction in the area available for the winding. In a slotted machine the slots can be made deeper to accommodate addition copper but this is not really possible in air-gap wound machine. Increasing the air-gap length with weaken the air-gap flux from the magnets, thus negating the effects of increased winding turns or cross section. However, the advantages of low armature reactance can override the restriction in winding window space and eddy currents because the power factor may be significantly increased, which can reduce the required current and back-EMF for a given power. It may also allow the use of a diode bridge rectifier rather than a controlled rectifier.

3.2.1 Cogging Torque and Torque Ripple

Cogging torque is due to the alignment of stator slots with magnets. If there is an integral number of slots per pole then in a direct-drive high-pole number machine this may be substantial. It can be reduced or removed with careful magnet pitch and skew. Cogging torque was discussed in [83] and this cogging torque occurs when the machine is open circuit and can get transferred through to ripple on the load torque. This may interfere in the machine operation particularly when the machine is generating and the load is low (i.e., the waves are small).

In terms of winding analysis, with the lack of stator slots cogging is not an issue. Therefore it is possible to use fully pitched coils and integral number of coils per pole per phase with a slotless stator and air-gap windings. The use of fully pitched windings allows a high fundamental winding coefficient with low harmonic content.

Torque ripple is not only due to cogging torque. For a three-phase PMSG, the current is controlled to be sinusoidal, or it is fed through a diode bridge. The back-EMF induced into the windings by the PM excitation should be sinusoidal, if it is not sinusoidal then there will torque ripple. Therefore it may be advantageous to use a fractional number coils per pole per phase so that the EMF induced into successive coils will be phase shifted, which will produce harmonic cancellation without a large reduction in the winding harmonic if they are arranged correctly. For a high pole

number machines it may also be good to use fractional slot windings because the pole pitch is quite small and it may be difficult to wind the stator with three coils per pole-pair, which is the minimum for a fully-pitched winding so that this needs to be carefully considered.

Therefore the choice of a slotted or slotless brushless PM machine still appears to be the correct choice for this application with both exhibiting advantages and disadvantages. Fractional and integral coils per pole-pair are also alternative options.

3.2.2 Permanent Magnet Materials

The selection of the PM material depends mainly on the cost, availability, remanent flux density and coercitivity. Recently, the use of rare-earth magnet material has become common in many electrical machines. This is due to the reduction of the cost of the material and improved magnetic characteristics. However, the price of this material is still relatively high and there are issues related to the supply chain of the material from China. Rare-earth magnets are the strong permanent magnets constructed from the alloys of rare earth elements. They are stronger than ceramic/ferrite or alnico magnets. The short circuit magnetic flux density produced by the rare-earth magnets (the remanent flux density) can be in excess of 1.2 T, while the ceramic magnets typically produce magnetic fields of less than 0.5 T. There are two types of rare-earth magnets: NdFeB magnets and SmCo magnets. They can be sintered or bonded; sintered magnets have much higher energy levels. Bonded magnets tend to be used when more complicated shaping is required. Sintered magnets are usually simple rectangular blocks or arcs and are often pre-magnetised before assembly because of issues and weaknesses concerned with magnetizing high energy magnets in-situ. They must be coated to protect them from breaking and chipping because they are vulnerable to corrosion. PM materials have been extensively discussed by others [119]-[121] and these treatises include discussions of many of the new developments and improved properties of the magnets. The key important properties which are used to compare the permanent magnets are the strength of the magnetic field, the remanence (B_r), and the material resistance to becoming demagnetized, i.e., the coercivity (H_c). The material properties for various permanent magnets are illustrated in Fig. 3.3 and tabulated in Table 3.1.

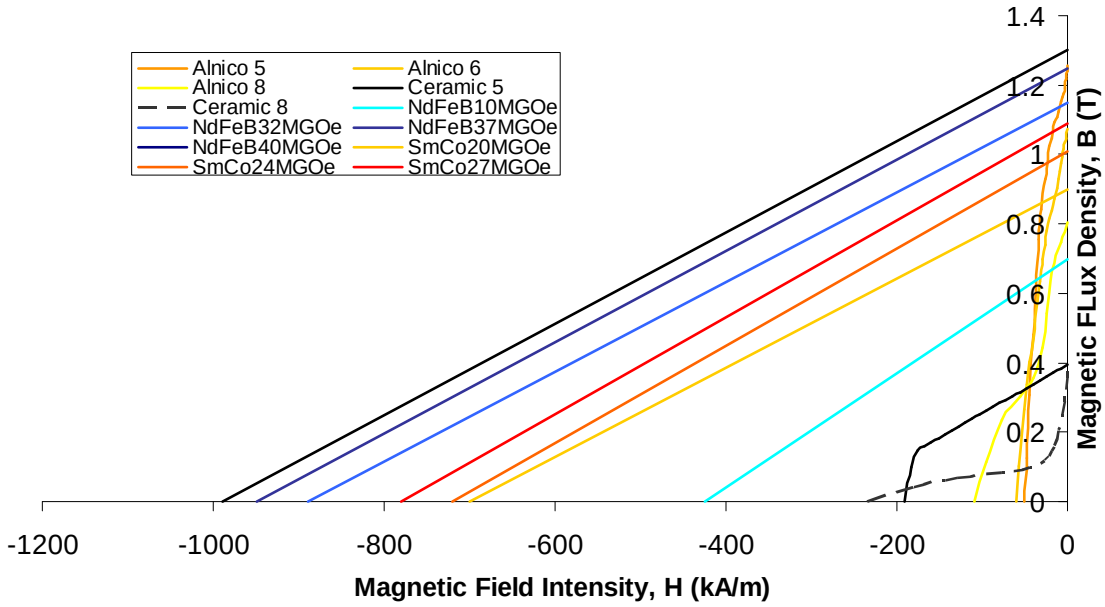

Fig. 3.3. Graph showing the typical *BH* curve for various PM materials.

Table 3.1. Comparison of parameters for various PM materials.

PM Materials	**Remanence B_r (T)**	**Coercitive Force H_c (A/m)**	**Relative Permeability μ**	**Electric Conductivity γ (MS)**
Alnico 5	1.254	50988.0	1.500	2.25
Alnico 6	1.075	59928.2	3.300	2.25
Alnico 8	1.804	109301	6.678	2.25
NdFeB 32 kJ/m^3	1.160	883310	1.045	0.667
NdFeB 37 kJ/m^3	1.251	950000	1.048	0.667
NdFeB 40 kJ/m^3	1.290	979000	1.049	0.667
NdFeB 10 kJ/m^3 (Bonded)	0.685	445634	1.223	0
Ceramic 5	0.394	191262.1	1.886	0
Ceramic 8	0.391	233567.9	1.438	0
SmCo 20 kJ/m^3	0.901	693000	1.034	1.176
SmCo 24 kJ/m^3	1.010	724000	1.110	1.176
SmCo 27 kJ/m^3	1.070	772000	1.103	1.176

From Fig. 3.3, it can be seen that alnico allows a high air-gap density and high operating temperatures. However, the demagnetization curve is very steep. Therefore it is very easy to both magnetize and demagnetize the magnet making it really only suitable for low energy instrumentation applications. Ceramic magnets are low cost magnets and have very high resistance which can be an asset to suppressing eddy currents but they are low energy. NdFeB and SmCo types of rare earth PM are both shown in Fig. 3.3; NdFeB has better magnetic properties than SmCo at the room temperature and this makes it the usual material choice for high energy magnet

applications. All the permanent magnets have advantages and disadvantages. The mega gauss-oersteds (MGOe) parameter used in Table 3.1 refers to the energy stored in the magnet; this is the maximum energy product. It can also be seen that NdFeB magnets have an almost linear demagnetization curve in the second quadrant. The knee of the coercive force curve is located in the third quadrant of the *BH* curve at the room temperature. This makes them hard to permanently demagnetise.

In addition to the performance of magnet materials, economic considerations must be addressed. If low cost is the most important criterion then ceramic magnets may be the most suitable material. However, in this study, high performance and high torque are desired, so that rare earth magnets should be used. Therefore, as dictated by the most recent consensus, NdFeB material was chosen in order to get a good relationship between the performance and cost.

3.2.3 Soft Magnetic Materials

Soft magnetic materials are usually in the form of rolled laminations or soft magnetic composites (SMC). SMC material consists of iron powder particles that are coated with the insulating film coating and pressed into shapes under high pressure. They tend to be used in small inductor cores and there is a push to use them in larger machines. SMC material has the advantage of allowing three dimensional flux paths but their relative permeability is still quite low compared to laminated magnetic steel. Hence they have not been adopted in electrical machines to any great extent. The traditional method for fabrication of electrical machines is to use the more standard lamination. The relative permeability is much higher since the steel is higher in density and the insulation coating is only on the lamination surface. This does give higher eddy current loss. For 50 or 60 Hz flux then lamination thickness may be in the region of 0.35 to 0.5 mm, whilst in aeronautical steel, designed for 400 Hz operation, the lamination thickness is much less and can be as low as 0.05 mm. This limits the eddy current loss. The resistivity, mechanical and ferromagnetic properties of the soft magnetic material depend on the iron powder particle size, density, insulation coating, compaction or rolling process and heat treatment cycle. Depending on the application, magnetic steel lamination material can be adapted to suit a specific application. A good generator with laminated silicon steel cores can achieve good magnetic

properties along planar flux paths. Lamination can be grain oriented, but this tends to be only used in transformers. For cylindrical machines, non grain orientation is required. The most suitable type of magnetic lamination for a PMSG is ferromagnetic material based on the iron and nickel, which is aimed at use in low frequency applications.

Steel cores increase the flux for a given magnetising force and decrease the device size and weight for a given rating. SMC cores are made by highly compacting insulated high quality spongy iron powder. So the eddy current losses are greatly reduced due to the high resistivity. However, as already stated, they have a low relative permeability so substantial redesigning is required for a given application in order to utilize it properly. Alloy powders could be used; they are a mixture of nickel, iron, copper and molybdenum. The higher the percentage of iron, the higher the saturation flux density and the higher the losses become [122]. The magnetic material properties for various materials are shown in Fig. 3.4 and Table 3.2.

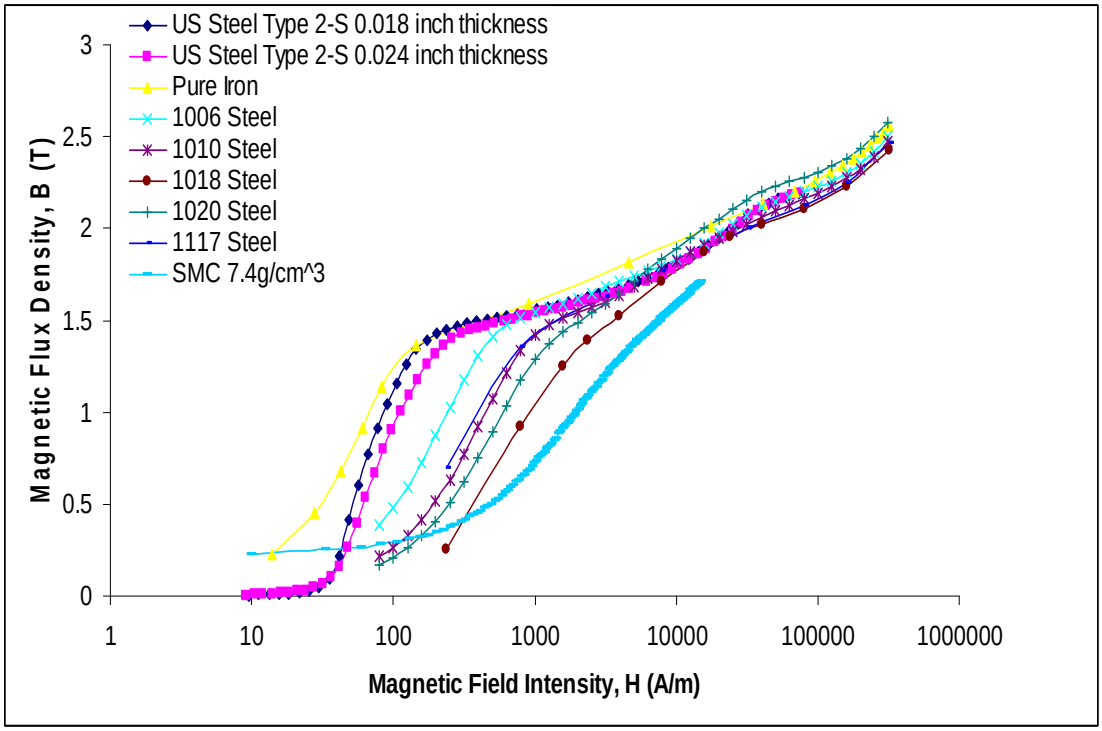

Fig. 3.4. Graph showing the typical *BH* curve for various Soft Magnetic materials.

Table 3.2. Comparison of parameters for various Soft Magnetic materials.

Soft Magnetic Materials	**Saturation Flux Density, B_{sat} (T)**	**$H(\mu_{max})$ (A/m)**	**Relative Permeability μ**	**Electric Conductivity γ (MS)**
US Steel Type 2-S 0.018 inch thickness	1.906	77.340	9400	6.25
US Steel Type 2-S 0.024 inch thickness	1.957	84.980	7400	6.25
Carpenter Electrical Iron	NaN	221.74	2065	7.69
Pure Iron	2.01	27.796	14872	-
1006 Steel	2.164	119.36	1404	0
1010 Steel	2.275	318.31	902.6	0
1018 Steel	2.43	795.77	529	0
1020 Steel	NaN	238.73	760	0
1117 Steel	2.13	238.73	1777	0

Fig. 3.4 shows the typical *BH* curve characteristics for the different soft magnetic materials. Table 3.2 shows comparative data for the main classes of soft ferromagnetic materials under consideration. The indexing of the steel is the grading system of the steel according to the Society of Automotive Engineers (SAE). The first digit indicates the main alloying elements which is the carbon steel. The second digit indicates the secondary alloying elements with 0 as plain carbon steel and 1 as the resulfurized carbon steels. The last two digits indicate the amount of carbon by weight. Generally, the materials with high saturating flux densities B_{sat} offer higher inductance capabilities (i.e., higher flux per amp) but at the expense of higher core eddy current and hysteresis losses.

3.2.4 Permanent Magnet Configuration

The PM rotor configurations in PM motors and generators have been discussed in many books and papers; a range is given in [83][94][95][123]-[125]. The main considerations will be the machine application, desired torque per rotor volume, torque ripple and cogging torque, power factor, and several others. The two most common configurations for the rotor are surface magnets and embedded magnets. The main advantages of embedded permanent magnets are that magnetic flux concentration is possible, and also there is *q*-axis saliency which can introduce a reluctance torque and also help in the field weakening region to extend the speed range (both of these effects utilize phase advance of the current so that there is both *d*

and *q* axis current, not just *q*-axis current). Cheaper magnets, such as ferrite magnets, can be used to get the same magnetic flux in the air-gap or high torque can be obtained with phase advance [84]. With appropriate design of the rotor, a near sinusoidal shaped flux waveform can be obtained with either surface or embedded magnets.

Lampolas [126] studied various surface PM locations for low speed machines. His findings show that arc magnets are the best solution followed by straight magnets located adjacent to each other. In this study, arc rare earth magnets in a surface PM configuration are chosen.

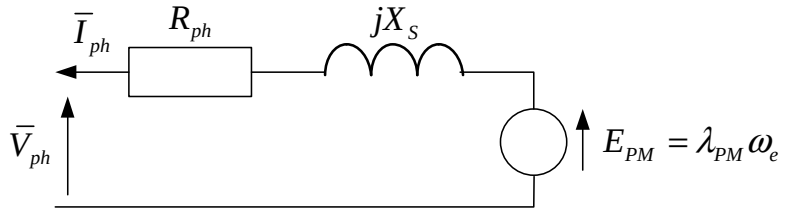

(a) Per-phase equivalent circuit for non-salient pole PM generator

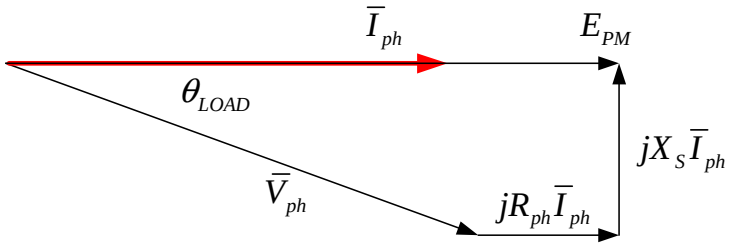

(b) Phasor diagram for non-salient pole PM generator with current on q axis

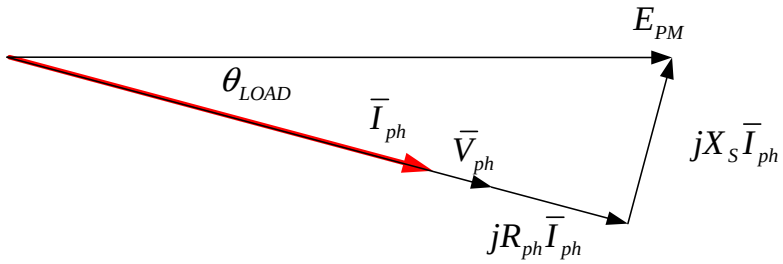

(c) Phasor diagram for non-salient pole PM generator with resistive (diode bridge) load

Fig. 3.5. Per-phase circuit and phasor diagrams for PMSG with surface magnets.

One advantage of the surface magnet PMSG is that it leads to a simple rotor design with low weight. It also has low armature reactance and there is no separation between the *d* axis (magnet-centred) or *q* axis (centred on the inter-pole position)

inductances so that $X_d = X_q = 2X_S/3$ = the winding self inductive reactance. This assumes that the mutual reactance between the phases is equal to half the self inductance in magnitude and negative (since there is a spatial rotation of 120º elec so that the linkage is scaled by cos(120º) = -0.5) and that there is a balanced sinusoidal 3-phase current set. In Chapter 4 the analysis considers *d-q* axis theory and transposition from 2-phase to 3-phase. This allows transient analysis – the analysis in the chapter considers only steady-state operation.

3.3 Analytical Method

An analytical method can be used to calculate the magnetic properties of a PMSG. These are couched in terms of machine and steady-state operation. We can use the geometry shown in Fig. 3.6. This is for a slotless machine with air-gap windings since this arrangement is adopted for the machine design.

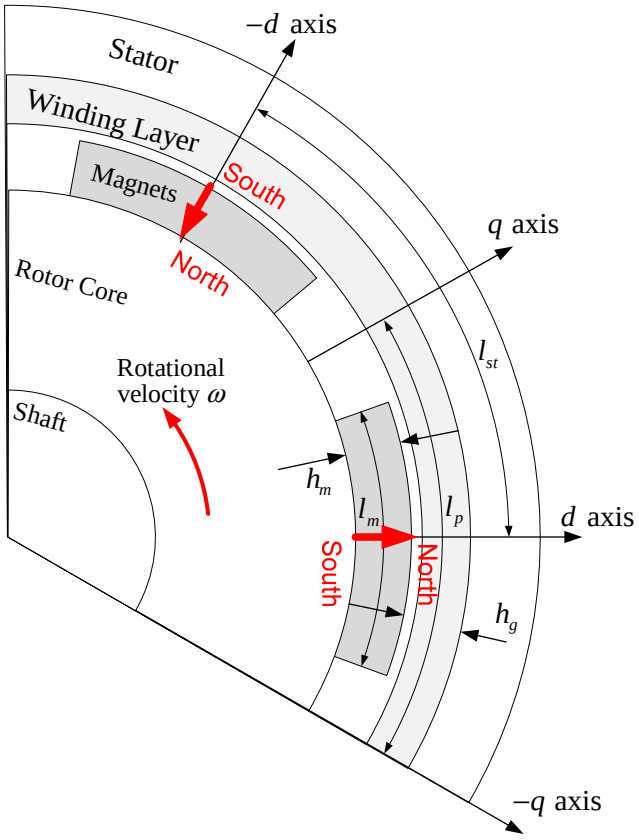

Fig. 3.6. Slotless machine geometry (2 poles of a 6 pole machine).

The equivalent reluctance circuit for a surface magnet synchronous machine is shown in Fig. 3.7 [127]. This allows us to study the magnetic performance of the machine. However, the equations in [127] are incorrect; the correct set of equations for the magnetic circuit is set out below.

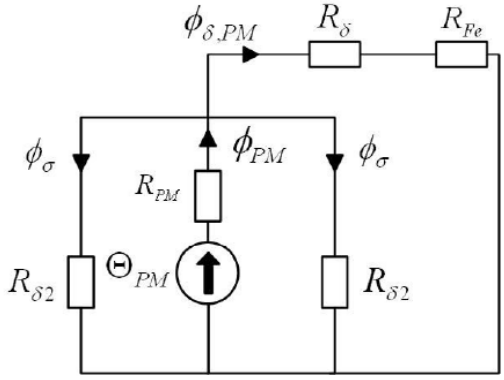

Fig. 3.7. Equivalent reluctance circuit for a PMSG with surface mounted magnets.

The parameters shown in Fig 3.7 are defined as the air-gap magnetic flux ϕ_δ, PM flux ϕ_{PM}, the magnet reluctance R_{PM}, the magnet end-region leakage fluxes ϕ_σ, the leakage reluctance in the inter-magnet region $R_{\delta 2}$, the air-gap reluctance between magnet and stator R_δ, and stator yoke reluctance R_{Fe}. The total magnet flux can be calculated and thus the air-gap flux, which can be used to calculate the EMF induced into the windings. Using the geometry in Fig. 3.6., the air-gap reluctance is

$$R_\delta = \frac{h_g}{\mu_0 \times l_p \times L_{stk}} \tag{3.1}$$

where h_g is the effective air-gap length between the PM and the stator core (for an air-gap winding this includes the thickness of the winding layer), μ_0 is the permeability of free space, l_p is the pole width at the mean air-gap radius and L_{stk} is the stack length of rotor (it is assumed that the stack length is the same for the rotor and stator). The PM reluctance is the reluctance of the magnet so that

$$R_{PM} = \frac{h_m}{\mu_0 \times \mu_{PM} \times l_m \times L_{stk}} \tag{3.2}$$

where h_m is the magnets thickness, μ_{PM} is the relative magnet permeability (generally, for a sintered NdFeB magnet this is in the region of 1.05 to 1.1), and l_m is the magnet width. The leakage reluctances either side of the PM can be put in parallel and treated as one reluctance; hence:

$$\frac{R_{\delta 2}}{2} = \frac{h_m}{\mu_0 \times \mu_{PM} \left(l_p - l_m \right) \times L_{stk}} \tag{3.3}$$

This is corrected from [127] by a factor of two due to the flux from adjacent magnetics. The stator teeth (if there are slots) will also have an effect if the length of the flux path is long and/or there is saturation. This reluctance is calculated through an iteration process if necessary to account for the non linear steel characteristics, although here the theory is being outlined. If the reluctance of the iron core is assumed to be constant (i.e., the flux density is below the knee of the BH curve), the air-gap flux due to PM is calculated using the equation:

$$\varphi_{\sigma PM} = \frac{\Theta_{PM}}{R_\delta + R_{Fe} + \frac{2R_{PM}}{R_{\delta 2}} \times \left(\frac{R_{\delta 2}}{2} + R_\delta + R_{Fe} \right)} \tag{3.4}$$

where R_{Fe} is the teeth and stator yoke reluctance and Θ_{PM} is the magnetomotive force (MMF) of the magnet. Again this is corrected from [127]. Since the demagnetization curve of the magnet is virtually straight line, the MMF can be expressed as

$$\Theta_{PM} = H_c \times h_m \tag{3.5}$$

where H_c is the PM coercive force and h_m is the magnet thickness. The flux depends on the magnetic potential differences along the different flux paths. For completeness we can also add in the stator yoke and tooth (these regions often saturate, particularly the teeth) so that the magnetic potential differences are:

$$\Theta_{t(i)} = H_{tooth} \times h_{tooth} \tag{3.6}$$

$$\Theta_{s(i)} = H_{yoke} \times l_{st} \tag{3.7}$$

where $\Theta_{t(i)}$ and $\Theta_{s(i)}$ are the MMFs (or magnetic potential differences) across the stator teeth and yoke, h_{tooth} is the stator tooth height (not shown in Fig. 3.6 because it is a slotless arrangement), l_{st} is the pole pitch arc length at the mean stator yoke radius, and H_{tooth} and H_{yoke} are the stator teeth and yoke coercive forces. Once the magnetic potential differences have been calculated, the tooth and yoke iron reluctances are added together using

$$R_{Fe(i)} = \frac{\Theta_{t(i)}}{\varphi_{PM}} + \frac{\Theta_{s(i)}}{\frac{\varphi_{PM}}{2}} \tag{3.8}$$

If an iterative technique is being used to account for steel saturation in the stator, with this new value of reluctance, the air-gap flux is calculated again by equation (3.4). This loop is repeated until the differences in fluxes densities from one step to the next one are less than an establish quantity.

One of the most important quantities is the per-phase back-EMF induced into a phase winding. This can be calculated from [94]:

$$E_{PM} = \frac{2\pi}{\sqrt{2}} \times f \times k_f \times N_1 \times \varphi_{\delta PM} \tag{3.9}$$

where k_f is the winding factor, N_1 is the total turns number per phase and f is the frequency of the induced back-EMF. The winding factor is a critical factor in assessing the effectiveness of the winding layout, especially in a fractional slot machine. This can be calculated from

$$k_f = k_p \times k_d \times k_{sk} \times k_s \tag{3.10}$$

where k_p is the pitch factor, k_d is the distribution factor and k_{sk} is the skew factor and k_s is the slot opening factor for a slotted stator or the spread of the air-gap coil for an air-gap winding . In this study, the skew is zero so k_{sk} = 1. Referring to Fig. 3.8, the different coefficients are defined below. It should be remembered that these are aimed at the general case where coils may have different number of turns and their pitch and position can also change. There are several references that review winding theory,

such as [95]. There are slight variations in the theory, particularly if double layer lap windings are used.

The pitch factor for coil *c* is defined can be defined as

$$k_{p(c)} = \sin\left(\frac{n\alpha_c}{2}\right) \tag{3.11}$$

where *n* is the harmonic number. And the distribution factor for a number coils that is average of the term for each coil

$$k_{d(c)} = \cos\left(n\phi_c\right) \tag{3.12}$$

where ϕ_c is the coil offset. This often completes the winding analysis in a slotted machine when the slots openings are narrow. However, if we have an air-gap winding we can account for the actual width of the conductor bundle where

$$k_{s(c)} = \frac{2\sin\left(\frac{n\beta_c}{2}\right)}{n\beta_c} \tag{3.13}$$

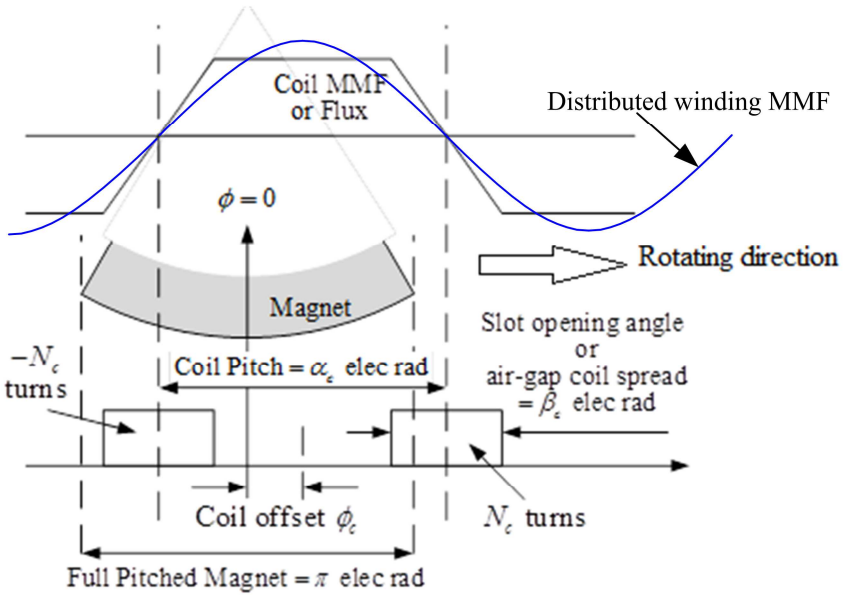

Fig. 3.8. Angular definitions for winding coefficient calculation (centre is stator series-connected phase winding is at centre of magnet).

If all the coils for one phase are in one spatial position with respect to the pole then k_d = 1. If the coil is fully pitched then k_p = 1. However, when there are several coils in different spatial locations with respect to the pole, different pitches, and different number of turns, then we can calculate the total winding factor as

$$k_f = k_{sk} \times \frac{\left(\begin{array}{l} N_1 \sin\left(\frac{n\alpha_1}{2}\right)\cos(n\phi_1)\frac{2\sin\left(\frac{n\beta_1}{2}\right)}{n\beta_1} \\ +N_2 \sin\left(\frac{n\alpha_2}{2}\right)\cos(n\phi_2)\frac{2\sin\left(\frac{n\beta_2}{2}\right)}{n\beta_2} \\ +....+N_C \sin\left(\frac{n\alpha_C}{2}\right)\cos(n\phi_C)\frac{2\sin\left(\frac{n\beta_C}{2}\right)}{n\beta_C} \end{array} \right)}{N_1 + N_2 + ... + N_C} \tag{3.14}$$

3.4 Finite Element Analysis (FEA)

Compared to the analytical method, the magneto-static field FEA solution offers a more accurate way of determining many of the PMSG parameters. The FEA method has been used by many researchers to verify the performance of the PM machines; some examples are listed in [128]-[132] although the number of references is very large. The air-gap flux in PMSG is due to the two sources of MMF - the permanent magnets and stator current (often called loading). The presence of magnetic saturation together with complex geometry and non-regular windings in fractional slot machines can make the determination of the machine flux distribution and resultant torque and flux linkages in the PMSG complex. However, all these can be solved using the two-dimensional (2D) FEA. For a surface PM rotor, the influence of magnetic saturation may be neglected in the rotor, and even in the stator, if only a low current loading is applied in a very high torque density design [131]. In a slotless machine, a 2D magneto-static model can be used to calculate separately the air-gap flux distribution produced by the PM and stator MMF. This is done by solution with open-circuit conditions and load conditions. This assumes that iron saturation has little effect on the magnet flux linkage, which may not always be the case; this is discussed later. In this type of magneto-static simulation, constant currents are set in

the machine to represent a snap-shot in time and the static flux and flux linkages are calculated. It is possible to conduct a number of simulations where the rotor is rotated and the current cycled to produce a set of results represented one rotor revolution or cycle through the current. It should be highlighted that this is not a full magneto-dynamic simulations, where the electrical circuit is voltage fed and both the flux and currents are calculated.

There are many ways to calculate torque in an FEA solution. This may involves using Maxwell stress tensors or Virtual Work methods. The Virtual Work method uses the computation of magnetic energy and co-energy and these are crucial for good torque calculation. The flux distribution within the generator is important because the magnetic energy and co-energy are dependent on this. The magnetic flux distribution can be found analytically through assumption and basic calculations and a simple lumped magnetic circuit. In an FEA solution, the device is discretely divided geometrically into small elements so that magnetic flux is calculated to a more detailed level, leading to more accurate solutions.

A magnetic field is formed from two vector quantities which are the flux density B and field intensity H. The flux density is the amount of magnetic flux flowing through a given area of material, while the field intensity refers to change in intensity of magnetic field due to the interaction of the flux with the magnetic properties of the material through which it is flowing. In the generator design, it is common to assume that B and H are collinear if it is modelled using a lumped magnetic circuit as outlined in Section 3.3. In other words, they are oriented in the same direction within a given material. B and H are related to the material permeability μ where

$$B = \mu H \tag{3.15}$$

For non magnetic materials the relationship is linear where $\mu = \mu_0$. If the material has magnetic properties than the permeability will be much higher (possible several thousand times) but there will be a maximum flux that is possible before the material domains are aligned and it saturates, creating the “knee” in the BH curve in Fig,. 3.4. The magnetic flux Φ flowing perpendicularly through a volume is the sum of the

magnetic fluxes that flow through each element in the volume so that it is the integral (or sum) of the flux components:

$$\Phi = \int B_z(x, y)dxdy \tag{3.16}$$

Faraday's Law states that the voltage induced into a circuit is equal to the rate of change of the magnetic flux linkage. The flux linkage can be viewed as the product of the number of winding turns *N* and the flux linking them. The flux linkage Ψ will alternate when the rotor rotates and the PM flux passes through the circuit coils in synchronism or in succession if there is spatial displacement between the coils. The voltage induced by the rotation is referred to as the back-EMF *e* so that

$$e = N\frac{d\Phi}{dt} = \frac{d\psi}{dt} = \omega_m \frac{d\psi}{d\theta} \tag{3.17}$$

$$\omega_m = 2\pi \times \frac{N}{60} \tag{3.18}$$

where ω_m is the angular velocity in rad/s, θ is the angle of the rotor with respect to the reference axis and *N* is the speed of the rotor in rev/min. Later, it is illustrated how in the FEA, by taking the difference between the magnetic vector potentials *A* of the "go" and "return" conductors of a coil, the flux linking the coil can be obtained in a 2D solution.

3.5 Generator Design

Low rotor speed can be a drawback for an electric generator because it is torque-limited; so that to obtain high power then high torque will be required. Standard generators (with two four or six poles) cannot be used in this case. Therefore, there is a need to develop a generator specifically for this application. A direct-drive generator must be designed with a large rotor diameter and a high number of poles. The high pole number is required to get a suitable frequency ratio to generate high torque. Wound rotor synchronous machines are used in direct drive generators in wind turbines, as already discussed, although many manufacturers are looking at PM solutions. Wound field synchronous machines need additional electric loading on the

rotor and suitable DC current control which adds complexity; these are in addition to the required slip rings. Given that the application is a marine application and simplicity is highly advantageous, then the only real solution is a high pole number PM generator. The next decision is to decide whether to use slots or air-gap windings. As already discussed it was decided to attempt an air-gap-wound slotless machine design. This gives low armature reaction. Even with high pole number the back-EMF frequency is relatively low so that winding eddy-current lost should not be a major issue. This will mean that the back-EMF will be low. Since the air-gap is relatively large due to the air-gap windings then the flux density and rate of change of flux linkage may be low so that the back-EMF has to be carefully addressed.

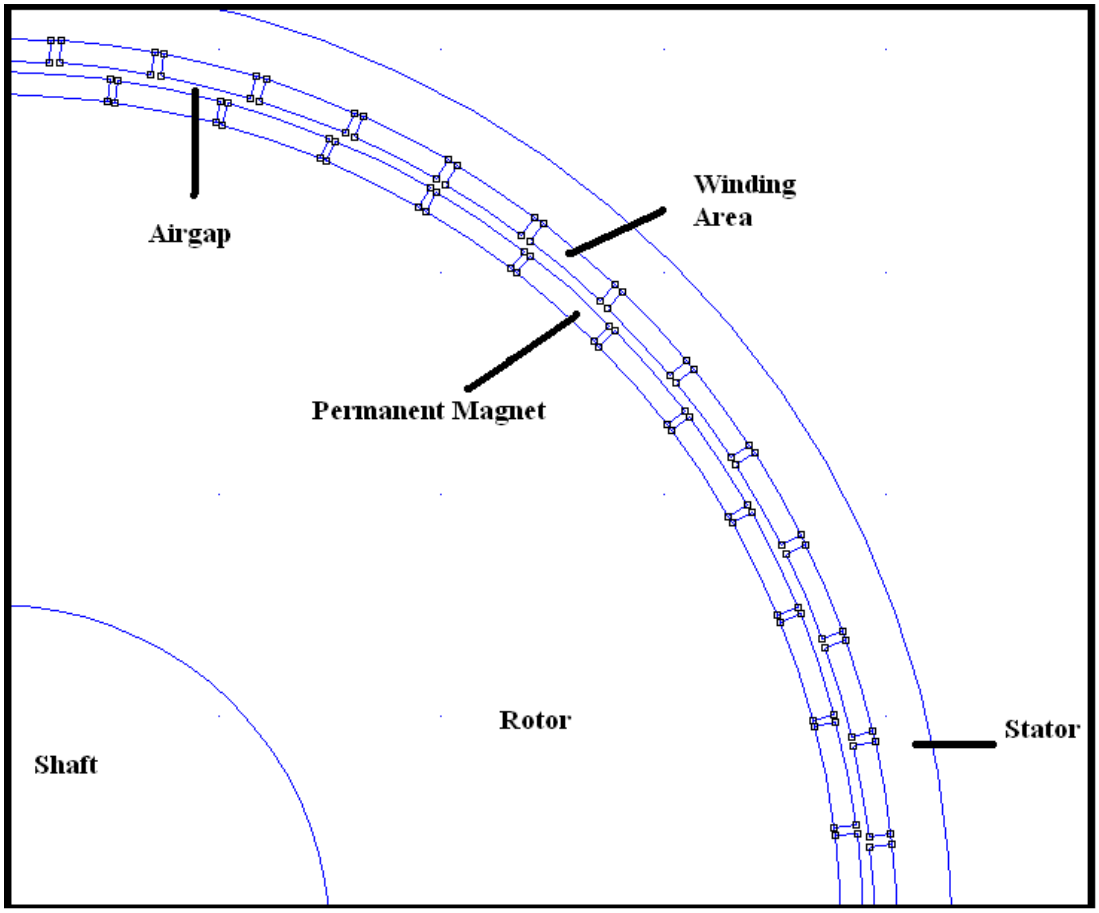

Fig. 3.9. Illustration of a slotless stator generator topology.

The generator designed is a three-phase machine. While higher phase number machines are used there is little advantage in this instance. It is also a radial flux type with an inner rotor. There are an increasing number of axial flux machines appearing; and these often have air-gap windings and sometimes no stator core. However, these

are either for use in small wind turbines with lower pole numbers or in high speed or frequency machines where the low flux density level is compensated for by high frequency.

The windings are wounded on the surface of the stator. Fabricating this sort of winding is not straight forward. The coils will probably need to be rigidly formed and potted in resin so that that they can be glued onto the stator surface. Dimension tolerances need to be set and adhered to so that the inner surface of the winding layer is circular and there is not rubbing on the rotor. As already mentioned, this slotless generator design has the advantage of minimal cogging torque and it poses lower winding inductance which can improve the power factor and allow use of a diode bridge rectifier. However, it also has some disadvantages as already discussed. The high pole number means that the winding area for a coil side in air-gap may be low. Therefore it may be worth moving a fraction number of coils per pole although double-layering may be advantageous to maintain a good winding factor.

A cross-sectional view of the generator designed is shown in Fig. 3.9. The machine consists of a rotor and a stator and this shows a FEA geometry in the FEMM package which is a freeware package and suitable for analysing these types of machine. High energy NdFeB 40 MGOe magnets are surface mounted on the rotor outer radius. The permanent magnets are uniformly magnetized in the radial direction and alternate in magnetization direction.

The mechanical position and speed refer to the respective position and speed of the rotor shaft. When the rotor shaft makes one complete cycle, it can be said as completing a 360 mechanical degrees angle. It will then be at the reference zero angle again. Other than the mechanical position, the rotational position is often defined by the electrical angular position and this has already been used several times. The use of electrical degrees is more relevant to the control because this spatial variation maps to the phase of the magnetic excitation, stator current phasor, and terminal voltage. The relationship between electrical and mechanical degrees is related to the number of magnet poles on the rotor [52]:

$$\theta_e = \frac{N_m}{2}\theta_m \tag{3.19}$$

where N_m is the number of magnet poles on the rotor, θ_e is the electrical position and θ_m is the mechanical position. For the generator designed, there are 48 poles (discussed later), so the mechanical pitch for 360 electrical degrees is:

$$360^{O} = \frac{48}{2}\theta_m$$

$$\theta_m = 15^{O}$$

If there was an integral number of coils-per-pole-per-phase then the analysis of the generator could be limited to 15 mechanical degrees because the magnetic orientation will repeat itself after that angle. However, if a fractional coil winding is used then the machine section that needs to be considered will be more. Fig. 3.10 illustrates one pole section. With a fractional slot winding then it can be seen that there winding does not correspond to a single pole.

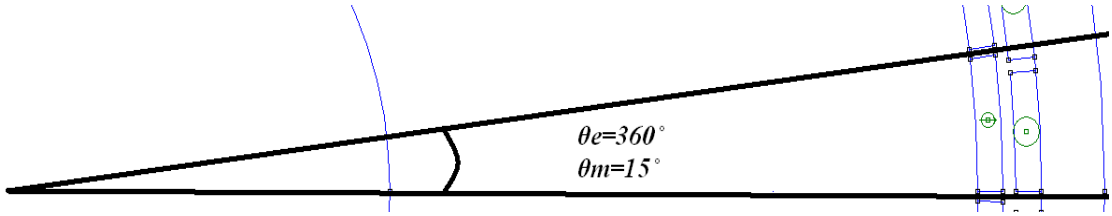

Fig. 3.10. Single pole representation and partial winding of a fractional slot machine.

3.5.1 Generator Sizing – Choice of Geometry Size

At this stage it is worth addressing some basic sizing equations. These give approximations for the output power and torque and were used for the first pass design sizes. The parameters chosen are given in Table 3.3 and the choice of these is discussed below. The outer diameter and axial length are dictated by the prototype cylinder in Fig. 3.11. However, were treated as guidelines. It will be seen that the axial length and diameter can be varied to maintain performance and the design should be close the enclosure volume.

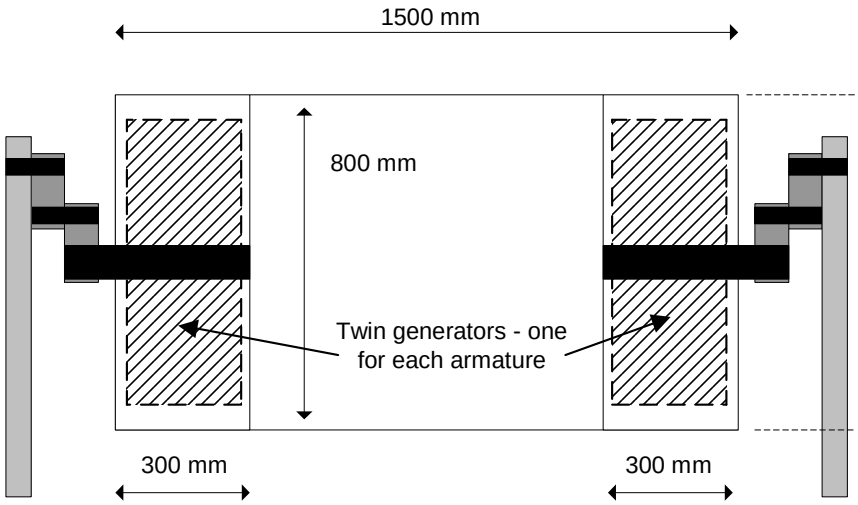

Fig. 3.11. Generator enclosure size.

The relationship between torque and torque-per-unit-rotor-volume is

$$TRV = \frac{T}{\frac{\pi}{4} D_r^2 L_{stk}} \tag{3.20}$$

The targeted wave period is 3 s. However, the wave device is meant to function for wave with different periods. For the lab scale device, it may functions within the range of wave period from 1 s to 4 s. To calculate the PMSG size, the best option is to choose the lowest speed where the device will be rotating which will happened when the wave period is 4 s. The median performance is aimed at the wave heights of 0.65 m at the wave periods of 4 s, the wave power than can be calculated using equation (2.9) as 1.66 kW/m at the 4 s period. This means that the torque requirement at this slower speed, with 25% mechanical energy harvesting, is about 200 Nm (this is per generator since there are two). According to Harris [133], the TRV for a PM machine is approximately 30 kNm/m^3 (as calculated above); and Miller [134] suggests that a machine with natural cooling system will have TRV value which can range from 7-30 kNm/m^3. We will assume that the TVR is a low value of 9 kNm/m^3 so that higher power operation will be possible in transient conditions. From the diameter and axial length, one of these has to be set. To enable the use of just one axial magnet layer and to allow a reasonable length (the magnet length will then be the same as the core length) it was decided to set the axial length to 50 mm. Hence:

$$D_r = \sqrt{\frac{4T}{\pi L_{stk} \times TRV}} = \sqrt{\frac{4 \times 200}{\pi \times 0.05 \times 9 \times 10^3}} = 0.76 \text{ m}$$

This is close to the enclosure diameter. However, this is for guidance as mentioned above. An iterative process can be conducted to design the machine in terms of air-gap winding and magnet thickness.

Thick magnets are needed for an air-gap-wound machine so the thickness was set to 10 mm. A similar thickness was used for the winding layer thickness. It was shown in [83] that the reluctance for a rare earth magnet machine can be high due to the strength of the magnets so that the load line can be less steep than for, say, a ferrite magnet machine. Since there are air-gap windings, which will not form a machined-surface bore, from a practical point of view a larger air-gap is needed due to air-gap winding tolerances. Hence the air-gap was set to 5 mm. A stator yoke is required and this was set to 15 mm thickness. In a high pole machine the yoke thickness will not necessarily be required for the magnetic circuit but it is needed for structural rigidity and integrity. This leads to an overall diameter of 860 mm which is slightly above the 800 mm of the cylinder diameter. The magnet width is 50 mm so that the magnets will be square, or they can be divided into two so that there are two 25 mm wide magnets per pole. Generally, the core length to pole pitch of an electrical machine lies in the region of 1:1 to 3:1. This gives good design features. If the ratio is too low then there can be excessive end effects in terms of leakage flux and high resistance coils because the coil ends are longer than the coil sides in the air-gap. If the machine is too long then there can be issues with flux-linkage and fabricating coils with very narrow pitch; there will also be high leakage between the magnets. It can be seen that with 50 mm axial length the ratio is 1:1. For the 100 mm the axial length this is now 2.88. These two designs probably lie at either end of the design limits. Obviously there are exceptions to this rule, for instance spindle machines, but these tend to be niche applications where the shape is dictated by the volume available and these machines will have compromise designs.

The design in Table 3.3 is maintained for the analysis below but the issue of the over sized diameter can be addressed. The generator enclosure is 300 mm wide;

usually the core length is about one third to one half of the machine length. Therefore we can set the axial length to 100 mm which gives:

$$D_r = \sqrt{\frac{4T}{\pi L_{stk} \times TRV}} = \sqrt{\frac{4 \times 200}{\pi \times 0.1 \times 9 \times 10^3}} = 0.53 \text{ m}$$

The magnet, air-gap, winding and yoke thicknesses should be maintained so that the overall diameter is 610 mm which is now suitable for fitting into the cylinder generator enclosure.

Table 3.3. Slotless generator specification.

Generator Parameter	Value	Generator Parameter	Value
Number of turns per winding area	150	Winding area	418 mm^2
Number of poles	48	Winding fill factor	27%
Number of winding areas	54	Magnet material	NdFeB 40 MGOe
Axial length	100 mm	Magnet relative permeability	1.049
Shaft radius/ Rotor inner radius	150 mm	Magnet Coercivity	97900 A/m
Rotor outer radius	380 mm	Magnet Conductivity	0.667 MS/m
Stator inner radius	405 mm	Coil	18AWG Copper
Stator outer radius	430 mm	Coil relative permeability	1
Electromagnetic air-gap	5 mm	Coil electrical conductivity	58 MS/m
Number of phases	3	Coil diameter	1.024 mm
Magnet thickness	10 mm	Stator and rotor yoke material	1117 Steel, low carbon, high manganese
Back-emf (V_{ph} peak) Constant [V/rpm]	1.88	Rated current [A] (10 A/mm^2 max –forced cooling)	1.6
Rated line-line voltage (rms) [V]	134.7	Rated speed [rpm] (3 s wave)	20 rpm

3.5.2 Generator Sizing – Performance Based on Size and Ratings

In this section we use further analysis to assess the machine performance at higher transient.

Gieras [94] used the magnet volume and suggested that it is proportional to the maximum generator power. He uses the equation

$$P_{\max} = \frac{\pi^2}{2} \times \frac{\xi}{k_f k_{ad} (1+\varepsilon)} f \times B_r \times H_c \times V_m \tag{3.21}$$

which contains many variables. Some of these can be approximated. k_f is the form factor of the rotor flux. This is in the range of 0.7 to 1.3 depending on the rotor topology. As an approximation we can assume it is unity. k_{ad} is the *d*-axis armature reaction factor and this is unity for a surface magnet machine. ε is the relation between no load induced EMF and net voltage, for a low armature reactance then this may be high. Although for a small machine like this there may well be high per-unit resistance. As a rough estimate take this as 0.8. f is the frequency of the back-EMF, B_r is the remanent magnetic flux density (1.05 for a the chosen rare earth magnet), H_{cu} is surface current density, V_M is the magnets volume (for the parameters below = $\pi \times (400^2 - 380^2) \times 50 = 2.45 \times 10^6$ mm^3 and ξ is the magnet utilization coefficient. This is quoted as being in the range 0.3 to 0.7. For air-gap windings then the utilization may be lower so as an approximation of 0.5 is taken. This leaves an equation

$$P_{\max} = \frac{\pi^2}{2} \times \frac{0.5}{1 \times 1 \times (1+0.8)} f \times 1.05 \times H_{cu} \times 2.45 \times 10^{-3} = 3.52 \times 10^{-3} f H_{cu}$$

The target speed for the cylinder is 1/3 = 0.33 Hz. There are 48 poles so that the frequency = 0.33 × 24 = 8 Hz which is low. However, in the simulations the frequency is taken up to 1 Hz so that the frequency is 24 Hz. To obtain good performance, higher frequency is required to increase the back-EMF. However, in practice this would be hard to realise because the pole pitch would be very small. H_{cu} is the surface current density in A/m. The winding is 10 mm thick. If we allow 10 A/mm^2 in the conductor (high for natural cooling but there may be forced cooling or this is considered a transient high point) and the fill factor is 27 % then the linear current density is 10 × 10 × 0.27 = 27 A/mm = H_{cu}. At 1 Hz:

$$P_{\max} = 3.52 \times 10^{-3} \times 24 \times 27 \times 10^3 = 2280 \text{ W}.$$

This does appear a crude sizing exercise with several approximations.

For radial machines, Hendershot and Miller [95] give an explanation for the sheer stress on the rotor surface and relate this to the diameter and axial length. The torque is

$$T = KD_r^2 L_{stk} \tag{3.22}$$

where T is the torque, K is the output coefficient and D_r and L_{stk} are the rotor diameter and stack length respectively. If σ is the sheer stress then

$$T = \sigma \frac{\pi D_r^2}{2} L_{stk} \tag{3.23}$$

and the sheer stress $\sigma = B_{gap} \times H_{cu}$ N/m^3. If it is assumed, conservatively, that the air-gap flux density is half the remanent flux density then

$$\sigma = \frac{B_r}{2} \times H_{cu} \tag{3.24}$$

Putting in the values in a similar to above gives

$$T = \frac{1.05}{2} \times 27 \times 10^3 \times \frac{\pi 0.76^2}{2} \times 0.05 = 643 \text{ Nm}$$

At 1 Hz this is a power of 643 × 2π = 4040 W which is higher than Gieras. The relationship between torque and torque per unit rotor volume is given in (3.20). If we use these high values for the performance then we find that the TRV is 28.3 kNm/m^3; this is a maximum and a transient condition and fits in with the range given by Miller [134].

The flux is limited by the saturation level and the geometry of the stator steel. The *BH* curve of the chosen stator steel is shown in Fig. 3.4. It shows the flux density *B* in the steel as a function of the magnetic intensity *H*. From the *BH* curve, it is found that the saturation is about 1.7 T and this should be a localized value. This needs to be checked in the FEA solutions.

3.5.3 Generator Winding

There are many different winding topologies available for brushless PM machines. It has already been mentioned that PMSGs do not need low harmonic windings in the same manner as induction machines. Broadly they can be split into integral slots-per-pole and fractional slots-per-pole (or coils for an air-gap winding). In addition there can be a divided in distributed windings (where the phase is made up of coils with different spatial position so the back-EMFs induced will have phase differences – this helps develop a sinusoidal waveform so they are suitable for brushless AC permanent-magnet machines) and concentrated windings (where all the coils have the same back-EMF induced into them which is more suitable for trapezoidal back-EMF waveforms; hence this makes them suitable for brushless DC PM machines – the coils can be fully pitched or short pitched around one stator tooth). Distributed windings may also provide better dissipation of heat together with the improved sinusoidal waveform, whereas concentrated windings may provide a larger back-EMF magnitude [135] because of the higher winding factor. Here a two layer concentrated winding configuration was chosen. This doubles the number of coils possible. The three phase winding set is star connected and spatially displaced by an angle of 120˚ electrical. The winding layout is shown in Fig. 3.12, where the red, yellow, and blue colour represent phases a, b and c respectively. Detailed information on the direction of the coils and the number of turns is listed in Table 3.4. The positive sign shows a coil in the "go" direction down the axial length of the machine while the negative sign shows a coil in the "return" direction where the current returns back along the axial length of the machine. A fractional slot arrangement is used so that the pitch of the coils is not too small. All together there are 54 "virtual" slots (air-gap coils sides). Only the details of first 18 virtual slots are shown because the winding will repeat itself in the same sequence twice.

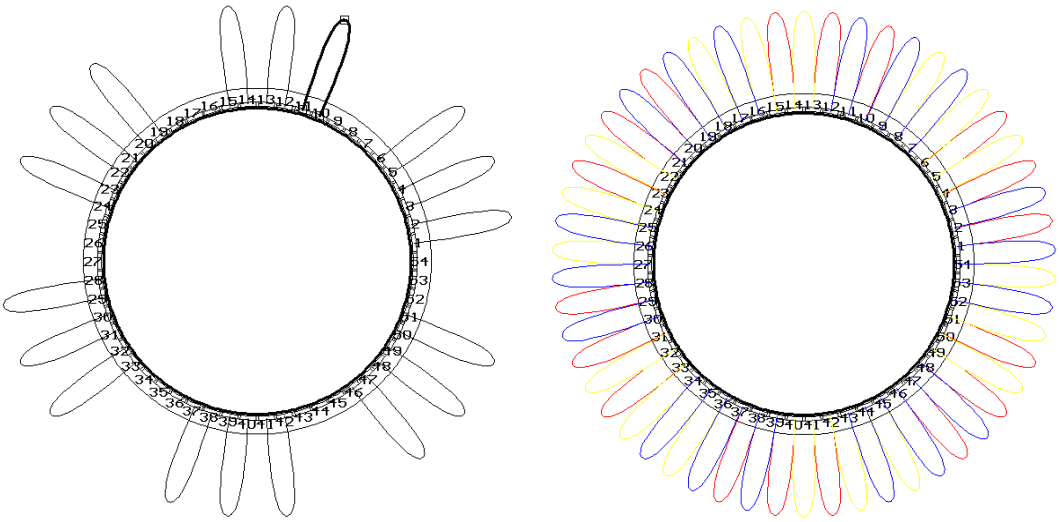

(a) (b)

Fig. 3.12. Winding diagram for (a) Single phase and (b) Three phase.

Table 3.4. Information on two layer concentrated windings.

Virtual Slot	Phase a	Phase b	Phase c	Total Number of Turns
1	75	0	-75	150
2	-75	0	75	150
3	75	0	-75	150
4	-75	75	0	150
5	75	-75	0	150
6	-75	75	0	150
7	0	-75	75	150
8	0	75	-75	150
9	0	-75	75	150
10	75	0	-75	150
11	-75	0	75	150
12	75	0	-75	150
13	-75	75	0	150
14	75	-75	0	150
15	-75	75	0	150
16	0	-75	75	150
17	0	75	-75	150
18	0	-75	75	150

The winding factors can be calculated for this winding. The exact angular values are shown in Fig. 3.13. There is no skew so that we can neglect the skew factor and in (3.14), all the coils have the same turns so that

$$k_f = \frac{\sin\left(\frac{\alpha_c}{2}\right)\frac{2\sin\left(\frac{\beta_c}{2}\right)}{\beta_c}\left[\cos(\phi_{\alpha 1})+\cos(\phi_{\alpha 2})+\cos(\phi_{\varepsilon 3})\right]}{3}$$

$$= \frac{0.985\times 0.76\times(1+0.766+0.766)}{3}$$

$$= 0.985\times 0.76\times 0.844 = k_p \times k_s \times k_d$$

$$= 0.63$$

This may seem low; however, the coil spread factor k_s will always be lower for an air-gap winding to the spreading of the coil side within the air-gap rather than concentrated in a slot. In addition, the lower distribution factor k_d is a result of requiring a good sinusoidal back-EMF and this is demonstrated later.

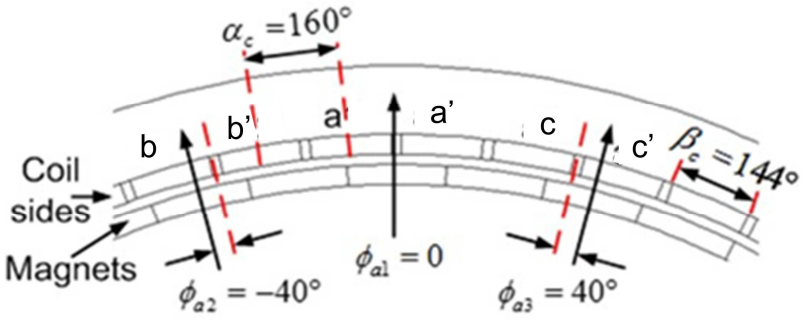

Fig. 3.13. Winding angular parameters for 54 coil winding.

The Goerges diagram of the coil is shown in Fig. 3.14. This is a good way to show the phasing of the back-EMFs induced into the coils and how the phasors add. The three phases are balanced and the phase sequence is red, followed by yellow and then blue which represent phase a, b and c respectively. They are 120˚ degree apart from each other. If the back-EMFs contain harmonics then this is a way of reducing the harmonic content of the total voltage; and hence produces a more sinusoidal phase voltage.

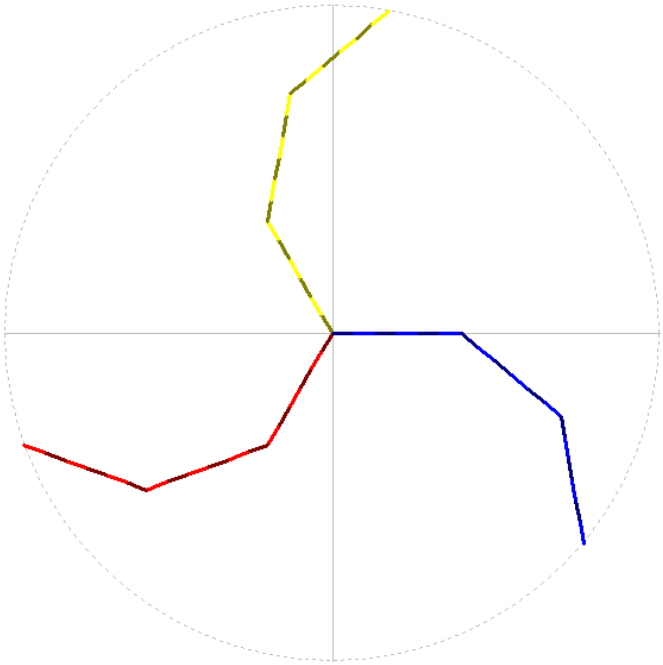

Fig. 3.14. Goerges diagram.

3.5.4 Generator Modelling and Analysis

The 2D meshed geometry of the PM generator is shown in Fig. 3.15. It is actually the discretization of the PMSG. To differentiate the components in the generator, different mesh sizes were used for different components. Mesh size of 0.1 is assigned to the coil, 0.5 to the magnet, 1 to the air and 1.5 to the steel. This yields a FEA model for the complete generator consisting of 53187 nodes. It is necessary to reduce the size of the mesh elements where there is complex geometry and the flux changes magnitude and direction sharply.

The flux distribution is shown in Fig. 3.16. The flux starts from one pole, crosses the air-gap and winding area before reaching the stator core, it then flows round to the adjacent opposite pole and re-crosses the winding area and air-gap and returns to the rotor. As the rotor rotates, the flux links the three phase windings of the stator in sequence. The magnetic flux plots are produced by post-processing after simulation. Pre-processing is necessary before simulation and this includes selection of material and magnetizing direction of the magnets, and definition of the winding. A 2D magneto-static simulation is performed to obtain the flux line/contour plot, the density/colour plot (shown in Fig. 3.16(a)), and the vector/arrow plot (shown in Fig.

3.16(b)). The air-gap flux density of the designed generator can also be obtained, as illustrated in Fig. 3.17.

After the successful completion of the magneto-static simulations, the post-processing is performed to obtain the flux linkage and induced waveforms. After each simulation, the rotor and current phasors are advanced to carry out the next simulation. The flux linkage waveforms for the 3 phases are shown in Fig. 3.18. The result shows sinusoidal flux linkage waveforms which peak at 0.7 Wb. As already stated, this was carried out using the FEMM freeware software. An LUA program was developed to carry out the simulations and rotate the current phasor and rotor automatically. The code is given in Appendix 2. The induced back-EMF E_{ph} results from both the FEA and analytical analysis are shown in Fig. 3.19. The analytical analysis was carried out using the *SPEED* software from the University of Glasgow. This allowed quick calculation. The rotor of the generator rotates at 60 rpm. The FEA results show a peak output voltage of approximately 110 V at no load, while the analytical analysis yields a back-EMF of approximately 100V only. For this generator, the back-EMF is almost sinusoidal.

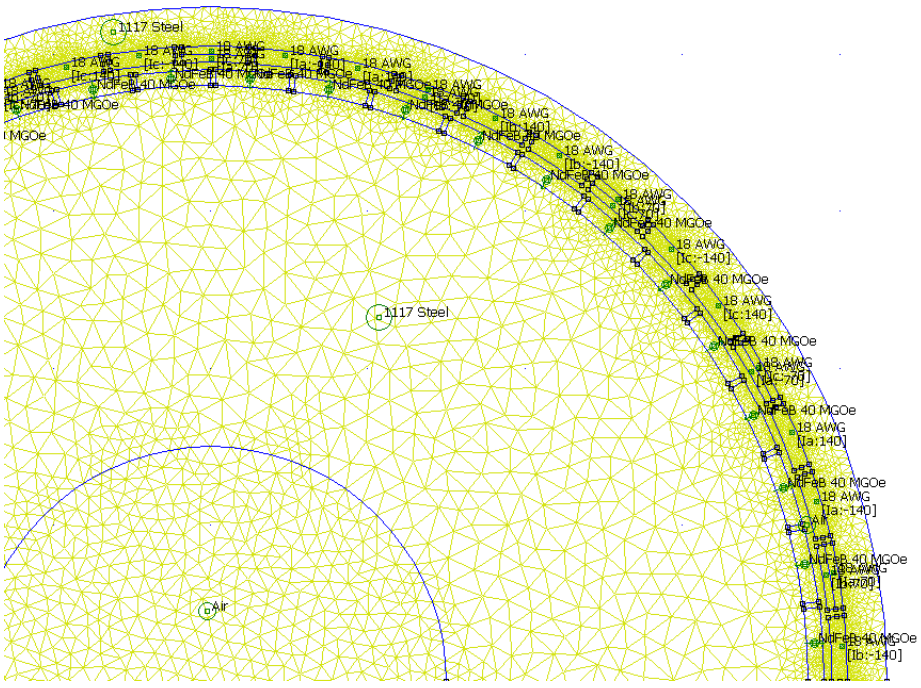

Fig. 3.15. 2D Finite element modelling.

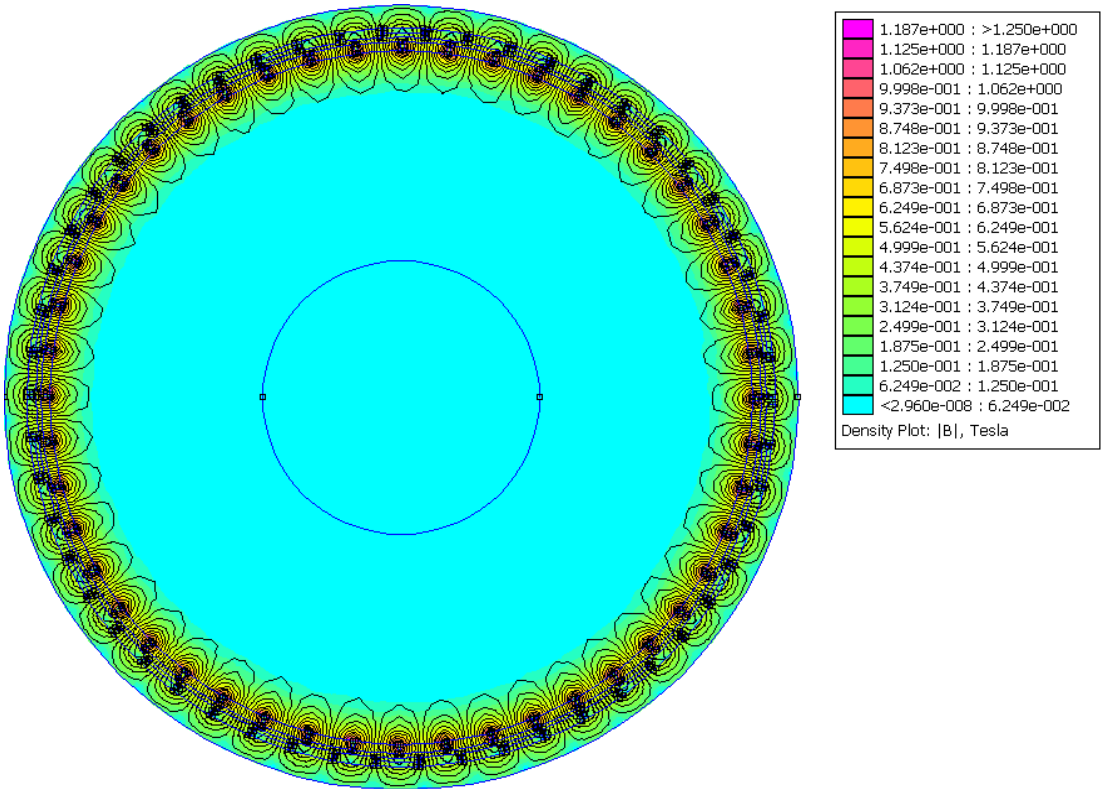

(a)

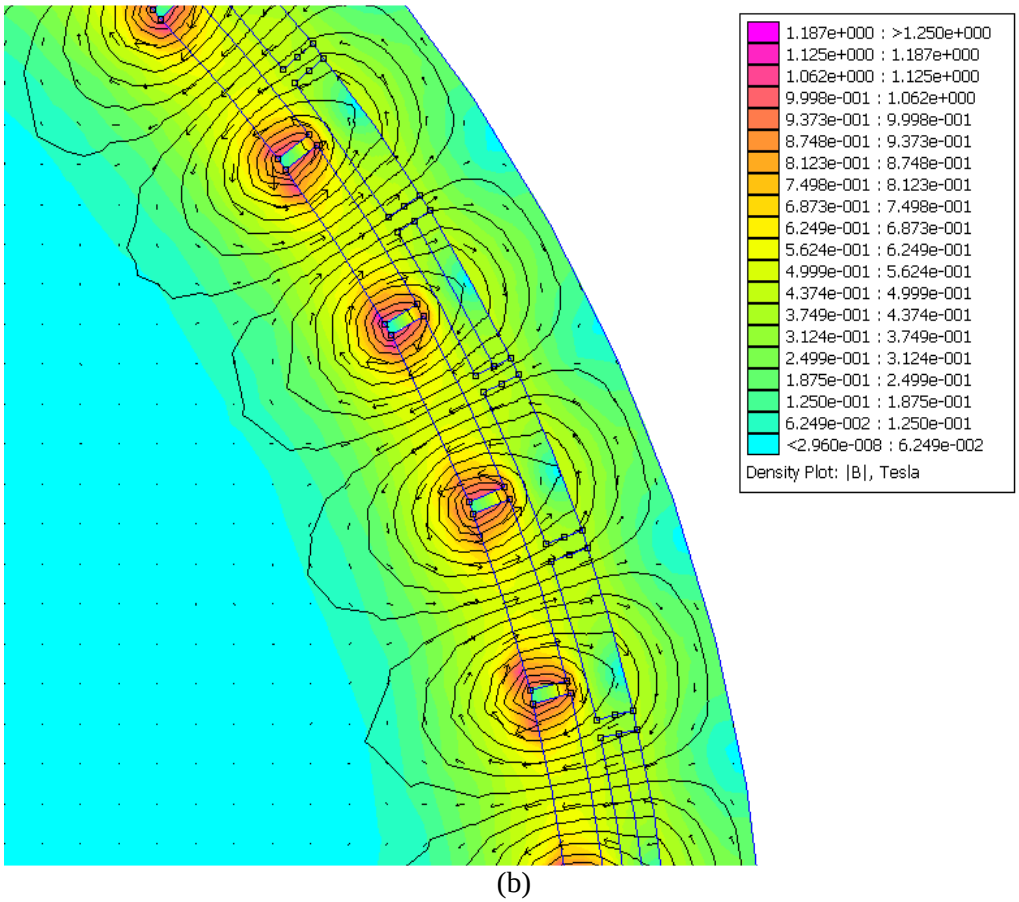

(b)

Fig. 3.16. Finite element analysis of generator showing open circuit (a) flux lines and flux density (b) vector plot.

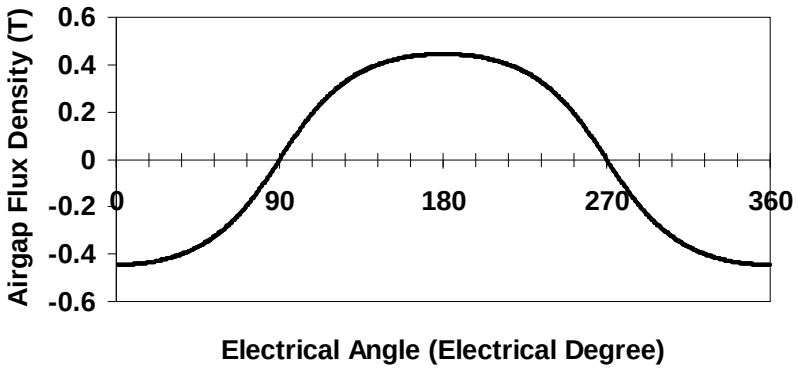

Fig. 3.17. Airgap flux density against the electrical angle.

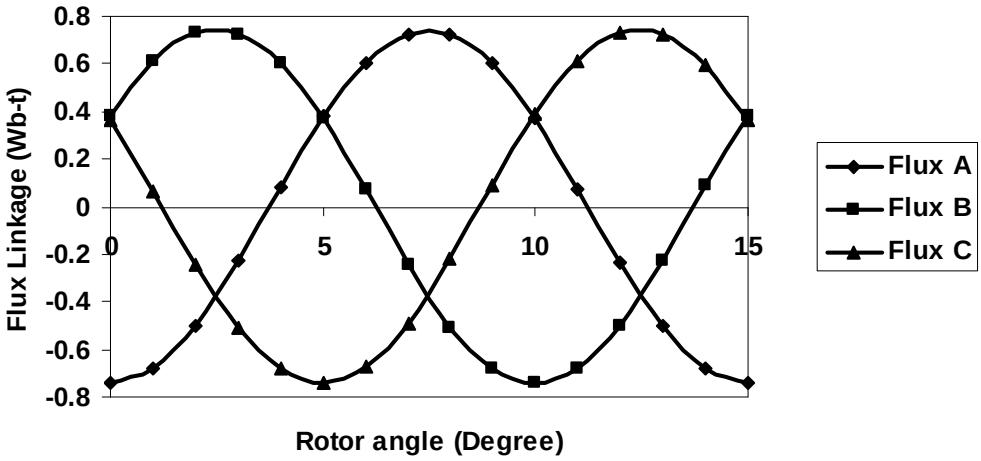

Fig. 3.18. Flux linkage waveforms of designed generator.

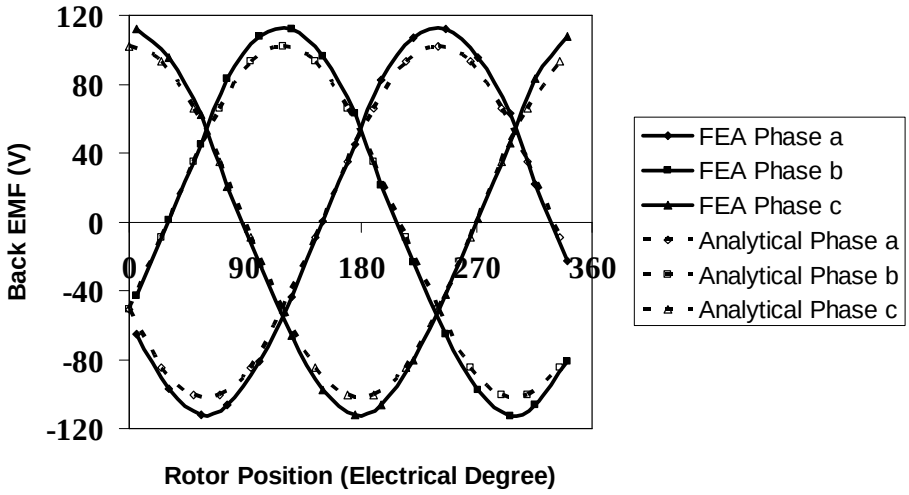

Fig. 3.19. Induced back EMF waveform at no load (60 rpm).

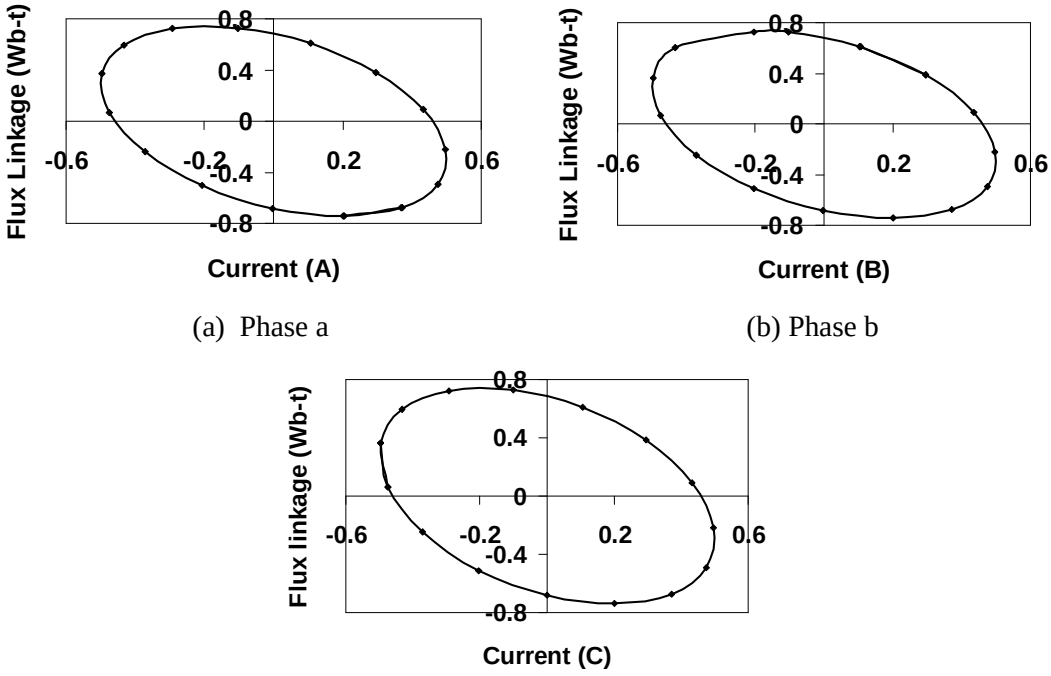

(a) Phase a

(b) Phase b

(c) Phase c

Fig. 3.20. I-Psi Loop at I_p=0.5 A.

The machine was simulated at 60 rpm with a peak AC current of 0.5 A in the winding and the current phasor located on the *q*-axis. The phase resistance is calculated to be 4.1 Ohm. The phase currents are sine waves and the frequency for the current at the winding is 24 Hz. The flux linkage-phase current (I-Psi) loops are shown in Fig. 3.20 and the area is 1.14 J which gives a power conversion of 82.1 W. The same calculation can be carried out using the back-EMF and peak current where the power = $3 \times 110 \times 0.5 \div 2 = 82.5$ W which illustrates that the simulation is correct and the results correlate well. However, the copper loss is $3 \times 4.1 \times 0.75^2 \div 2 = 4.6$ W. At a wave period of 4 s, the mechanical energy harvested is 200 Nm. So the power required is $200 \times 2\pi \div 4 = 314$ W. If this is taken as the electro-mechanical power conversion then the peak current is 1.9 A at that 60 rpm. At this point the copper loss is $3 \times 4.1 \times 1.9^2 \div 2 = 22$ W which is 7 % of the energy conversion. If the speed drops to 15 rpm (4 s wave period) with the same power the current increases to 7.6 A peak so the copper loss is now is $3 \times 4.1 \times 7.5^2 \div 2 = 355$ W, which is higher than the mechanical input power of 314 W. To improve the design, more poles are required to increase the voltage constant. The problem with low frequency high pole number machines was discussed in [50] and in previous sections. To allow simulations with

reasonable generation the phase resistance was reduced by 10 times on some simulations. If the machine was scaled up the per-unit resistance would be much less. In terms of the design here, the fill factor is only 25 % and there is a 5 mm air-gap. With precision in terms of coil manufacture, the fill factor is increased to about 0.7 (maybe using rectangular conductors) and only a 1 mm air-gap then the area can be increased by about 4 which would reduce the resistance to 1.05 Ohm. The fundamental issue is still with the pole number being too low.

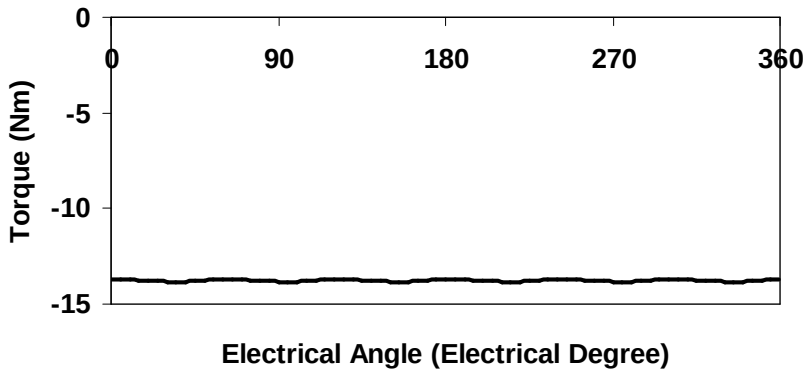

Fig. 3.21. Total machine torque.

The PMSG total machine torque is obtained from the FEA simulations as illustrated in Fig. 3.21. It is found that the machine torque had little torque ripple around the mean value of -14 Nm. The minus sign shows that it is in generating mode.

The inductance and reactance of the winding coil can now be calculated. Walker [136] suggested to calculating the flux linkage using the frozen permeabilities method so that the back-EMF is calculated under loaded rather than unloaded conditions. While Gieras [137] has compared the analytical approach and FEA method in calculating the PM machines reactance. The accuracy of FEA in reactance calculations were also determined [138]. Here, the inductance and reactance value are calculated using the flux linkage method [139][140] under FEA, the inductance and reactance can be estimated. To calculate the flux linkages in the FEA, let A_p represent the average magnetic field, A over the positive part of the coil for phase a, and A_m represent the average A over the negative part of the coil.

The flux linkage can then be found as $N\times(A_p - A_m)$ where N is the number of turns of the coil. First, the flux linkage with just the magnet ϕ_{PM} is obtained and then

the flux linkage with magnet and coil current (I_c = 5 A) is obtained, this is ϕ_{PM+C}. To get the flux linkage due to current in the coil (ϕ_C) we can use

$$\phi_c = \phi_{PM+C} - \phi_{PM} \tag{3.25}$$

The winding inductance L can be found from FEA result where

$$L = \phi_C / I_C \tag{3.26}$$

This includes the self and mutual inductances. For a surface PM machine the reactance then can be calculated using

$$X_d = X_q = 2\pi fL \tag{3.27}$$

The results are shown in Table 3.5. The flux linkage of the permanent magnet are acceptable and the inductances of the machine are rather low which shows typical characteristics of a PMSG. It does meet the specification needed for the machine designed in this research. The final design of the PMSG is shown in Fig. 3.22.

Table 3.5. Generator parameters.

Parameters	**Value**
ψ_{PM+C}	-0.3553 Wb-t
ψ_{PM}	-0.3718 Wb-t
ψ_C	0.0165 Wb-t
L	3.3 mH
$L_q = L_d$ (self inductances only)	2.2 mH
$X_d = X_q$ (including mutuals with other phases)	3.6 Ω

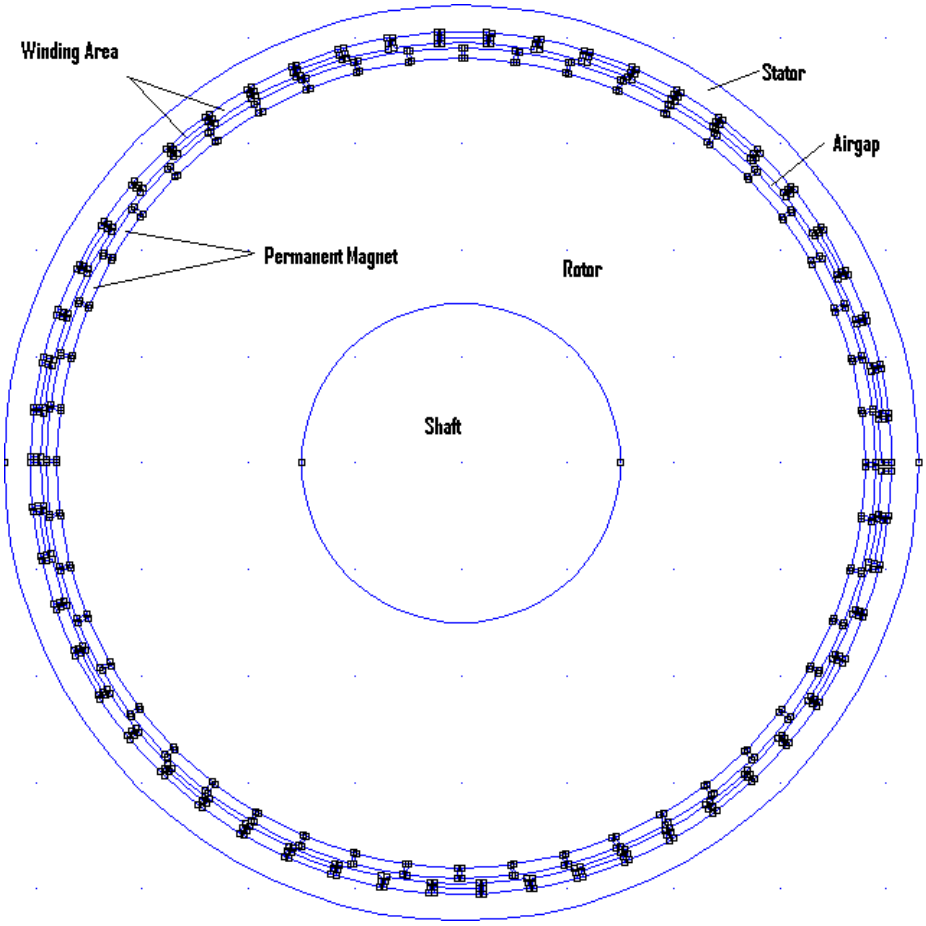

Fig. 3.22. Final design of PMSG.

Chapter 4

BRISTOL CYLINDER CONTROL

4.1 Introduction

The amount of power obtained from a wave energy conversion system not only depends on the characteristics of the incoming waves at the site, but also on the control strategy used for the wave energy system. The control strategy being applied in each device varies according to the type and functionality of wave devices. In order to improve the power delivered by the Bristol Cylinder, the rotational speed of the turbine should be able to vary depending on the period of the sea wave. The best wave energy extraction is achieved by running the wave device in a variable speed mode which should be synchronous with the incident wave speed. How the torque varies as the cylinder rotates in its orbital motion is still not clear from the literature and should be the focus of further work.

Large multi-pole generators are needed for low speed gearless operation of a PMG used in a wave energy device [141], as discussed in the first half of this thesis. Therefore it is very wise to maximize the power capability of the generator to prevent unnecessary additional generator size and cost. Several different types of control strategy have been proposed for a wind turbine with a multi-pole PMSG [142]-[146]. All major wind turbines function in similar manner in terms of the way wind energy is converted to electrical energy by the turbine; which rotates at a speed that is a function of the wind speed (assuming it is a variable speed turbine). In other words, the control strategy applied to one wind turbine may be adapted to another wind turbine by making some necessary minor changes.

Unlike the wind turbine, wave energy can be tapped by different wave devices which operate in very different ways to each other. For example, the Wave Dragon device is controlled by regulating the floating height of the device to the optimal level for the sea state to maximise the power flowing over the ramp [147][148]. In an OWC, the rotational speed of the turbine can be achieved by adapting one of several turbine

speed control methods used in wind turbines since there are similarities in the way it functions [149][150]. An optimal switching control is applied to the ocean wave energy device to determine the lock and unlock switching times [151][152].

4.2 System Consideration

Unlike most of the cases where the position of the turbine is always fixed from the reference axis, the Bristol Cylinder wave device have a turbine which is attached to the fixed axis through 2 flexible arms. So the rotational axis will be changing according to the incident wave to maximise the power caption. However, the radius will be kept constant throughout a full rotation cycle. As a result, the moment of inertia of the Bristol Cylinder rotating on the sea surface can be treated as a solid cylinder rotating about an external axis. Thus the moment of inertia can be calculated using equation (2.25) as described earlier.

The diagram in Fig. 4.0 (a) illustrates the cylinder physical dimensions and extends the radius of rotation of the cylinder to clearly show the cylinder motion. There is considerable inertia in the cylinder. As already described in Chapter 2, for and ocean-going device the cylinder is marginally buoyant and could be 15 m in diameter and 50 m in length (typically, for a 5 MW device and 3 m 10 s waves, the power is $50 \times 981.2 \times 3^2 \times 10 = 4.5$ MW).

The orbital movement of the cylinder is assumed circular, and in perfect monochromatic waves they would indeed be so. However, in reality there will be a spectrum of wave frequencies and they will be travelling in different directions. A flexible connection is required to allow the orbital radius and rotational velocity to change quickly. The armature and double generator method here does allow this within an arc of wave directions. The device was discussed by Boyle [153] and a set of hydraulic dampers was used in the illustration in [153] as shown in Fig. 4.0(b). When the UTS micro-wave-tank was being developed travelling and standing waves were produced because waves were reflected from the beach due to its steepness. A small free-moving cylinder was tested and it could be seen in Fig. 4.0(c) which it rotated in an elliptical orbit. Hence excellent control is required for this application.

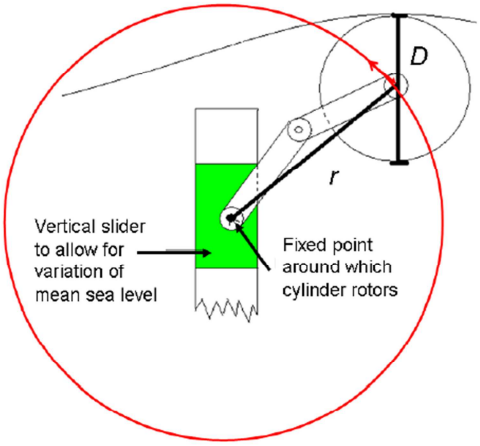

(a) System arrangement with dimension variables.

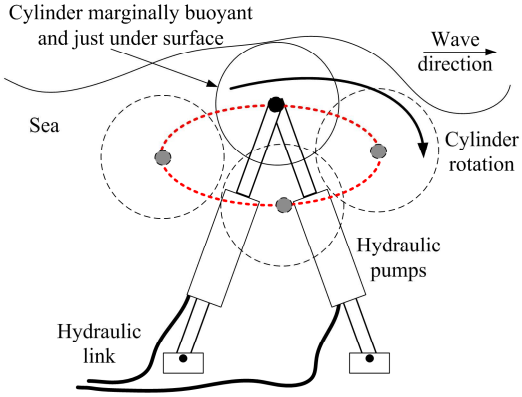

(b) Alternative arrangement as reported by Boyle [13].

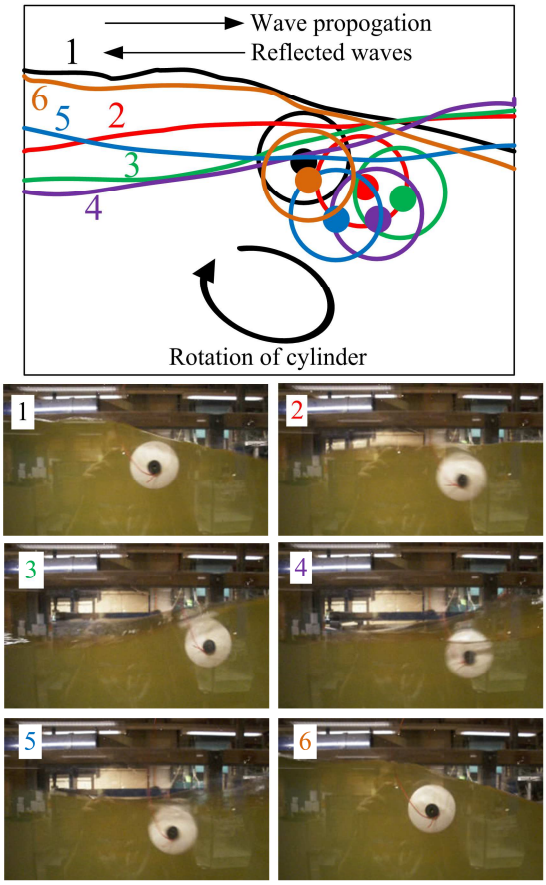

(c) Tests in UTS micro-wave-tank with component of standing waves showing eliptical orbit.

Fig. 4.0. Cylinder arrangements and simple testing in micro-wave-tank.

High-energy sea waves have long wavelengths and periods as mentioned previously. Typically, deep sea wave periods are in the region of 10 to 20 seconds. Increasing power with decreasing frequency is the inverse of the usual demands of a drive/generator system.

Electrical machines tend to be torque limited so that as the speed increases so does the power flow through the machine. These two points create a challenging machine design and control [154]: i) it is very slow speed (even slower than a wind turbine) and ii) the power delivery requirement increases with decreasing speed. In addition the power delivery over one cycle will pulsate and the degree of this pulsation is still under investigation; the speed may also vary.

4.2.1 Control System Simulation Arrangement

The control strategy for a variable speed wave generator is illustrated in Fig. 4.1. This is realized in the MATLAB/Simulink environment. The main goal of the control is to improve the maximum power conversion of the system over a range of typical wave heights and periods.

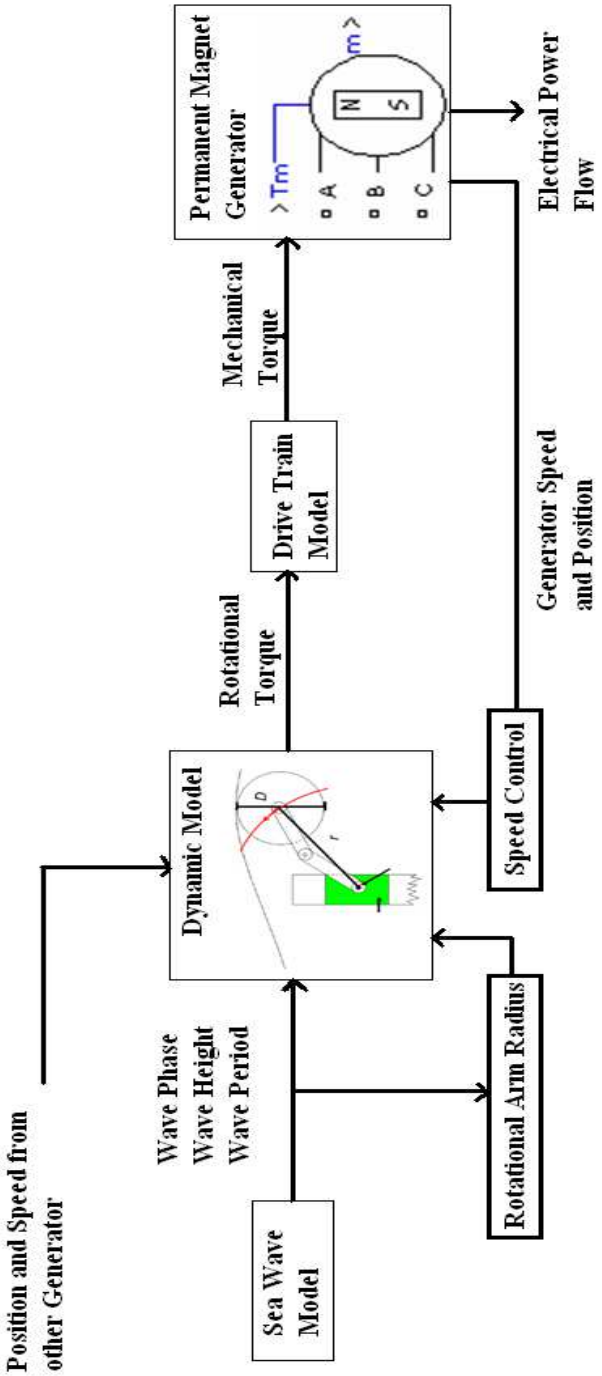

Fig. 4.1. Wave generator representation in MATLAB/Simulink.

The system begins by predicting the sea wave parameters and feeding the information to the wave device. In reality, waves are random so that when designing the wave generator control system, some critical issues have to be addressed; these are related to the difficulty in predicting and measuring the waves accurately as they approach the Bristol cylinder. The random nature of the incident wave heights and periods [155] are such that the cylinder will track a prevailing wave. A number of researches have been made in forecasting irregular waves. Forsberg [156] introduced an autoregressive with moving average model with fixed time horizon prediction. Halliday et al. [155] use the fast Fourier transform to generate prediction of waves over distance. In the laboratory, the monochromatic waves can be generated, but this is usually far from the case in open-sea conditions. However, in early-stage development these are used for system testing.

The input from a mechanical torque source will serve as the prime mover which actually turns the PM synchronous generator in circular motion. The two main device controls involved in this stage are the control of the rotational radius and the speed control of the generator. The PM synchronous generator model from MATLAB/Simulink is chosen for simulation as shown in Fig. 4.2. The generator does not take into consideration the saturation effect in the iron because the air gap in the generator is large enough to prevent from saturation problem. The mechanical torque input is a negative value because the machine model is simulated using the motoring convention.

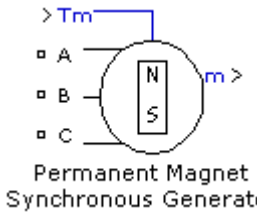

Fig. 4.2. PMSG block from MATLAB/Simulink.

Since this is an AC generator, the flux established by the PM in the stator is sinusoidal and this is further proven when analysing the generator designed. The block uses the *d-q* axis equations listed below:

$$\frac{d}{dt}i_d = \frac{1}{L_d}v_d - \frac{R}{L_d}i_d + \frac{L_q}{L_d}p\omega_r i_q \tag{4.1}$$

$$\frac{d}{dt}i_q = \frac{1}{L_q}v_q - \frac{R}{L_q}i_q + \frac{L_d}{L_q}p\omega_r i_d - \frac{\lambda p\omega_r}{L_q} \tag{4.2}$$

$$T_e = 1.5p\left[\lambda i_q + (L_d - L_q)i_d i_q\right] \tag{4.3}$$

where L_q and L_d is the q and d axis inductance respectively, R is the resistance of the stator windings, i_q and i_d is the q and d axis current respectively, v_d and v_q refer to the q and d axis voltages respectively, and ω_r refers to the angular velocity of the rotor, λ is the amplitude of the flux linkage from the PMs of the rotor in the stator, p is the number of pole pairs and T_e is the electromagnetic torque. These equations are used for vector control of generator drives. The current vectors will usually sit on the q-axis for a non-salient pole surface-magnet motor, where $L_d = L_q$, or it may be advanced in the salient-pole surface PM motor to utilize reluctance torque. Phase advance will also help in field weakening for the non-salient pole machine to enable extended operating range. In generator mode this can be advanced to the lower half-plane so that there is negative q-axis current. This requires controlled rectification.

The power from the rotation of the wave device rotor is transferred to the generator through the drive train [157] as shown in Fig. 4.3.

The electromechanical equations that relate the parameters [156] are:

$$J_s\frac{d^2\theta_s}{dt^2} = T_s - K\left(\theta_s - \theta_g\right) - D\left(\frac{d\theta_s}{dt} - \frac{d\theta_g}{dt}\right) \tag{4.4}$$

$$J_g\frac{d^2\theta_g}{dt^2} = T_e + K\left(\theta_s - \theta_g\right) + D\left(\frac{d\theta_s}{dt} - \frac{d\theta_g}{dt}\right) \tag{4.5}$$

where T is the torque in Nm, J is the moment of inertia in kgm^2, θ_s is the torsion angle of the Bristol cylinder and θ_g is the torsion angle of the generator in rad, K is the stiffness coefficient in Nm/rad and D is the damping coefficient in Nms/rad.

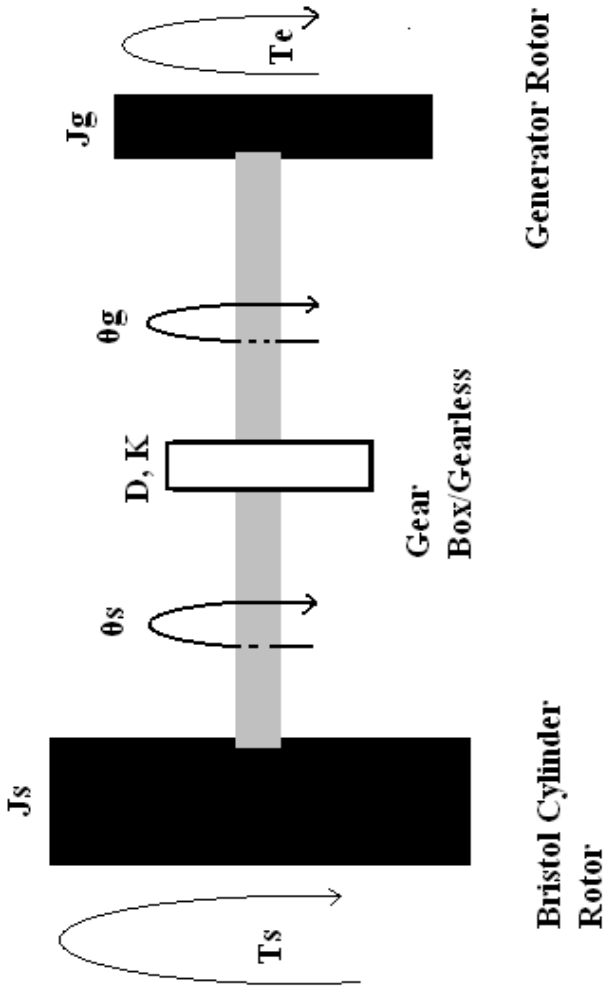

Fig. 4.3. Drive train model.

4.3 Outline Control of Bristol Cylinder

The control is a critical issue in determining the performance; the aim is to maximize the power generation from the waves through to the load. Different control strategies need to be applied to the different system components. In order to obtain the maximum power from the waves, two different control methods were implemented in the simulations over a spread of operating conditions. Even though the typical theoretical power curve for a wind turbine can be adapted for Bristol cylinder device, the control of the Bristol cylinder is more complicated than a wind turbine because there is variation in both wave period and wave height, and also there is a spectrum of waves. A typical theoretical power curve for a Bristol cylinder wave turbine is shown in Fig. 4.4, this is similar for many variable speed generators systems. *H* represents

the wave height, $H_{cut\text{-}in}$ is the wave height where the device can start to harvest energy, H_n is the nominal wave height and $H_{cut\text{-}out}$ is the wave height where the device will stop working.

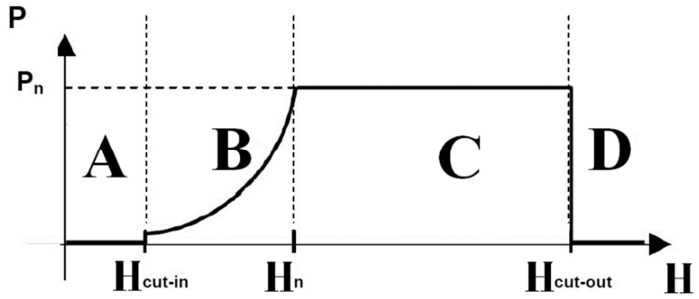

Fig. 4.4. Theoretical power curve (power vs. wave height).

The power curve can be divided into different power regions. Region A is the system idling region; there is insufficient wave resource to generate useful energy. Region B is the constant torque region which extends up to the base speed. Region C is the constant power region. This is often called the field weakening region where the objective is to limit the output power at its nominal value. This is actually limited by the maximum amplitude of the armature connecting the Bristol cylinder and the fixed axis attached to the vertical slider. In area D, the output power from the Bristol cylinder is zero. The sea state is too energetic for generation and steps should be taken to sink the cylinder and avoid storm damage. As can be seen, the power profile in Region B increases with wave height. This is the region that shows the counter effect for a wave system where the wave energy increases with decreasing wave velocity, and the generator speed is locked into the wave frequency for a Bristol cylinder unless a gearbox is used.

4.4 Effect of Armature Length

The study on the effect of armature rotational radius length is necessary to control the Bristol Cylinder rotor speed. The purpose of this study is:

- To produce as much power as possible in the low speed range. The armature amplitude needs to be varied in a dynamic fashion since the incident wave parameters are constantly changing.

- To keep the hydrodynamic power constant at its rated value so that the design limits are not exceeded when the wave period is low and wave heights are high.

The armature radius may work in three possible states within the working zone: maximum radius; minimum to maximum radius; and minimum radius (which is the length of the single armature assuming that both the arms have equal length).

Using the wave period and wave height, switching between generating states changes the armature rotational radius position so that the desired value is generated in the output. The first and the third cases are fixed; this occurs with Regions A and D. In the second case, the rotational radius is obtained from [158]:

$$R_r = He^{\frac{2\pi}{L}Ds} \tag{4.6}$$

where R_r is the rotational radius, H is the wave height, L is the wavelength and D_s is the rotational axis depth.

Fig. 4.5 shows the Simulink model to study the rotational radius effect of the Bristol cylinder.. The saturation block functions as the radius limiter between minimum and maximum radius. If the radius value calculated is lower than 0, which is unlikely to happen, or when it is higher than the maximum radius, which again depends on the armature length, the signal will be clipped to the lower and upper boundaries. When the input signal is within the range specified, the input signal will pass through unchanged. A rate of change limiter is needed to limit the rate change of radius to protect the armature from damage due to rapid changes.

Fig. 4.6 shows some results from the simulation. The applied wave height varies from 0.1 m to 0.8 m in 0.1 m steps. These steps were filtered to include the effect of rise/fall time for the changing of the incident wave state. In the second graph of the figure, rotational radius is shown for the case where for large Bristol cylinder where the armature length is more than 1.5 m and the maximum rotational radius can reach more than 3 m. For the case of the lab-scale Bristol Cylinder, where the size is relatively smaller, the results of the rotational radius are shown is the third graph, where the armature length is only 0.3 m and the maximum rotational radius can reach 0.6 m. This was carried out to test and illustrate the armature radius corresponding to

the incident wave. All the simulations were carried out with constant wavelength and depth.

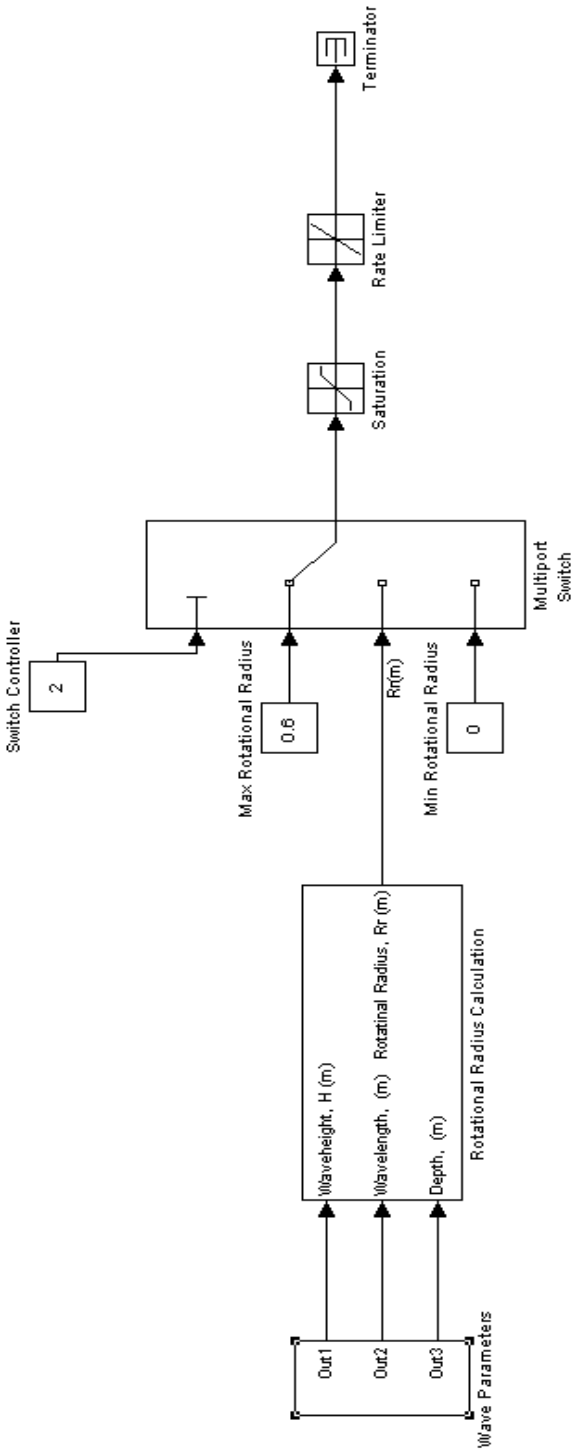

Fig. 4.5. Bristol Cylinder Rotational radius corresponding to incident wave.

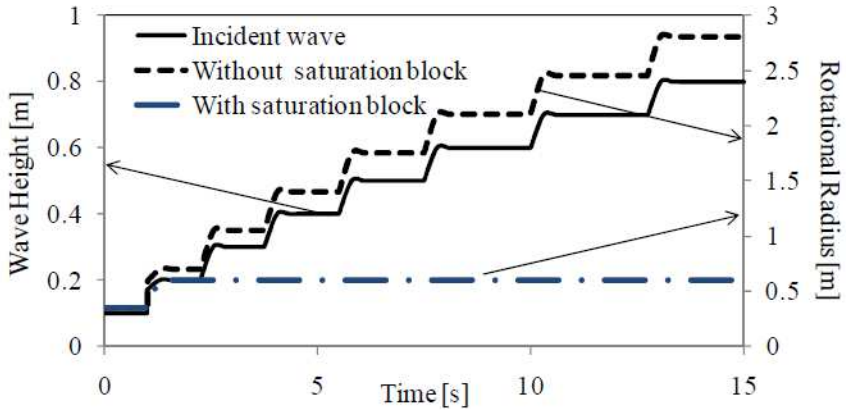

Fig. 4.6. Rotational radius respond: (a) Incident wave and corresponding rotational radius; (b) Without saturation block (for large wave device); and (c) With saturation block (for small scale wave device).

4.5 Bristol Cylinder Speed Control

Variable speed generators are required for this device due to the fact it was to run synchronous with the waves. Energy extracted does not depend solely on the wave characteristics at the site but also on the control strategy used for the generator. Generally, the motion or speed control of a PMSG poses many similarities with that used for motoring applications. Operation of the synchronous machine can be controlled using nested speed and current (torque) loops, using different torque control algorithms depending on the power electronic converter used [159].

The speed control of the PMSG can be carried out using the vector control method [160]. Vector control means the process of decoupling the flux linkage and torque control yielding rapid response and high energy conversion rates through appropriate reference flux linkage and torque relationships. The decoupling can be performed by mutual flux linkage control, optimum torque per unit current control, maximum efficiency control or maximum torque-speed control. For high performance speed control, there are two main control methods classified under vector control which are FOC and Direct Torque Control (DTC) [161] which can be applied.

These control techniques have undergone considerable research over the past few years [162], where both methods have been found to have their own advantages and drawbacks. DTC results in a non-constant inverter switching frequency, which may result in high inverter or generator loses. Most of the studies concentrate on the application of vector control to wind turbines since its application to wave energy devices is still limited. Some newer control strategies have been developed in order to account for things such as the usage of batteries [163] in the system, the single cycle control [164] and multilevel control [165].

In this work, the FOC method is used for the vector control of the generator. This method is first developed around 1970. FOC can be implemented in two ways, namely the indirect and direct methods; these depend on the way the rotor flux is identified. Direct FOC determines the orientation of the air gap flux using Hall effect sensors, search coils or other measurement sensors. This increases the cost and special modifications of the generator are required to place the flux sensor. To date, there is no specific equipment that can actually sense the flux directly. At low speed, this may cause inaccuracies when calculating the rotor flux from a directly sensed signal due to the stator resistance voltage drop and other reasons.

As a result, indirect FOC method is chosen for implementation in the simulation of the control of the Bristol Cylinder speed. The calculations of the flux positions for indirect FOC method are based on estimations of the terminal quantities such as the voltages and currents in a generator model. It does not have the low speed problems and is the preferred method for this application. In a PMSG the rotor flux linkage is fixed to the rotor position. The objective of the FOC is to maintain the amplitude of the rotor flux linkage at a fixed value and modify only the torque producing stator current component in order to control the torque of the machine.

Electromagnetic torque is produced by the interaction between the stator flux linkage from the rotor magnets and stator currents (or the rotor flux linkage and rotor current), and it can be expressed as a complex product of the flux and current space phasors. In order to decouple the torque and flux, the stator current is transformed into a rotating reference frame, which is the flux producing component, *d*-axis current

which represents the direction of rotor flux phasor and the torque producing component, *q*-axis current which is perpendicular to the rotor flux.

Here, FOC is implemented by controlling the flux and torque of the PMSG separately using a current control loop with PI controllers. This is done by transforming the stator current vector into the *d-q* components, which control the flux and torque respectively. The objectives are to control effectively the PMSG torque and flux to force the generator to accurately track the command trajectory regardless of the machine and load parameter variations or any external disturbances. This is to regulate the speed of the PMSG so it actually synchronises its speed to the speed of incoming waves, which is a necessity for torque production and energy generation.

Constant torque angle (CTA) control and maximum torque per ampere (MTPA) control [165] strategies are applied to obtain the stator *d-q* current components. The flux positions in the coordinates can be determined by the shaft position sensor because the magnetic flux generated from the PMSG is fixed relative to the rotor shaft position. CTA control keeps the torque angle constant at 90 degrees. This is done by keeping the stator *d*-axis current I_{sd} at 0, and the *d*-axis flux linkage λ will be fixed. This leaves the current vector on the stator *q*-axis only. Since speed changed slowly relative to the control system then the velocity ω_f is assumed constant for a PMSG, so that the electromagnetic torque is then proportional to the stator q-axis current I_{sq}. This is determined by the closed-loop control. The rotor flux is only on *q*-axis while the current vector is controlled to be on this axis in the FOC. In this case, the MTPA control can be achieved since the generated generator torque is linearly proportional to the *q*-axis current. For this method, good control of the stator current amplitude will obtain the maximum torque. The speed vector control scheme of the PMSG is shown in Fig. 4.7 as described in [160], where $\omega_m = \omega_f$ and $K_q = \lambda$.

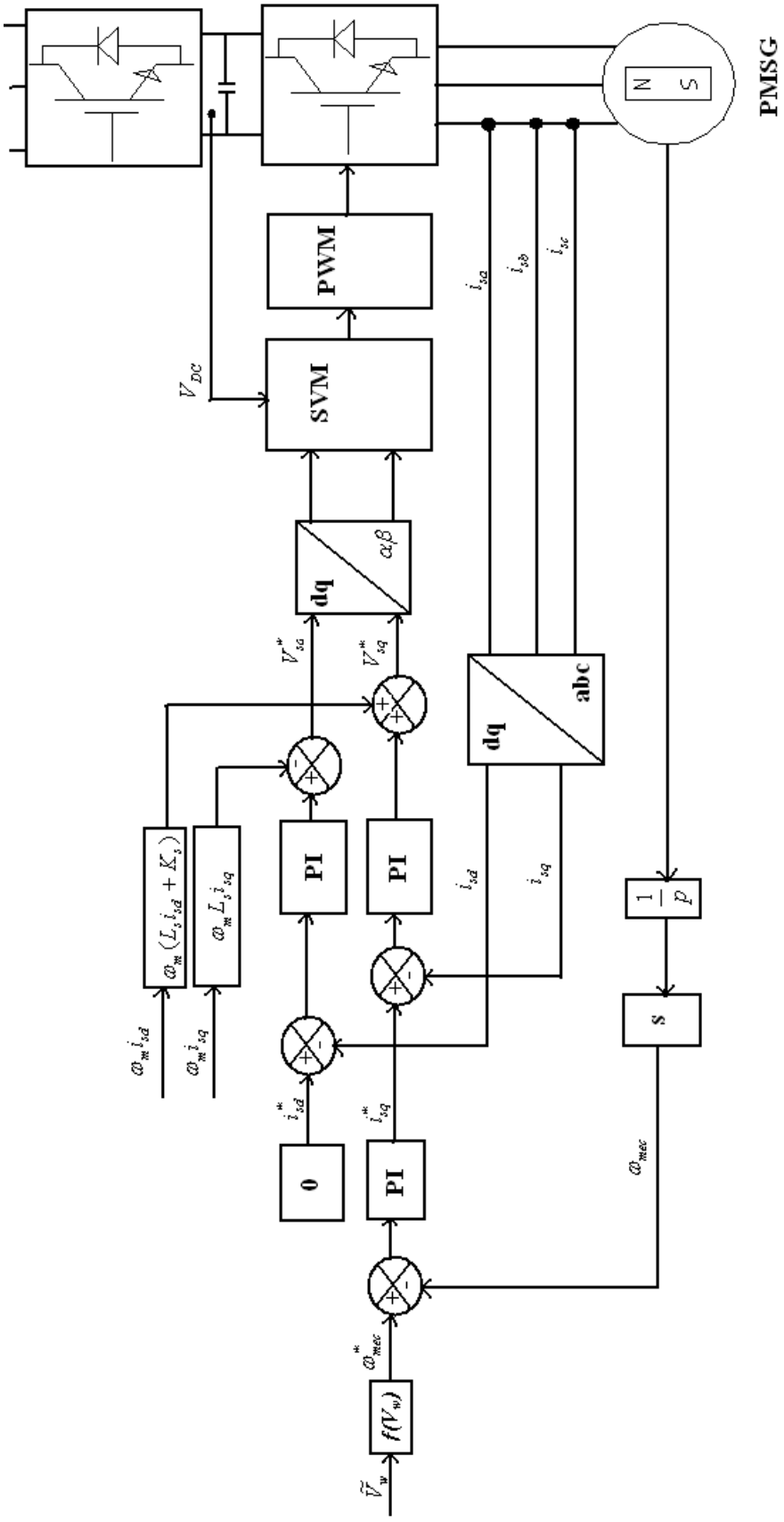

Fig. 4.7. PMSG vector controlled structure [161].

4.5.1 Modelling and Simulations

The whole system is implemented in MATLAB/Simulink and is shown in Fig. 4.8.

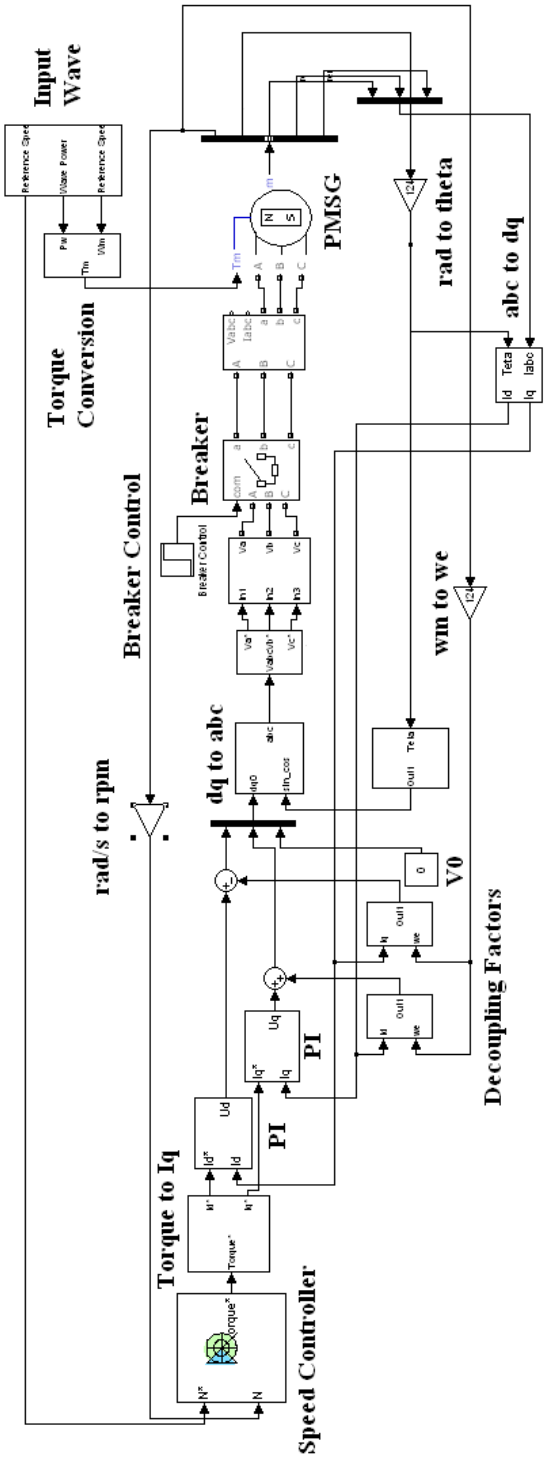

Fig. 4.8. Indirect FOC control scheme.

The Bristol Cylinder driving torque is computed based on the wave power equation and the relation between the torque, speed and power. This is performed in the 'Input Wave' and 'Torque Conversion' block as shown in Fig. 4.8. The torque is supplied to the PMSG to rotate it. Input parameters for the PMSG include the stator phase resistance, stator phase inductance, flux linkage established by the permanent magnets, inertia, friction factor and the number of pole pairs. The PMSG can generates outputs which include the stator phase current, stator back EMF, rotor speed, rotor angle and electromagnetic torque.

The equation of motion shows the relationship between speed, the electromagnetic torque and the inertia so that

$$T_r = T_e + J\frac{d\omega_m}{dt} \tag{4.7}$$

where T_r is the mechanical torque delivered by the prime mover, T_e is the electromagnetic torque of the generator, J is the Bristol Cylinder inertia and ω_m is the rotor speed. From the equation shown above, is can be seen that that the rotor speed can be controlled by varying the electromagnetic torque. The variable which controls the electromagnetic torque is the *q*-axis current component. So the speed can actually be controlled by varying the *q*-axis current.

In the 'Speed Controller' block, the measured rotor speeds obtained from the PMSG in rad/s are converted to rpm. The measured rotor speeds are then compared to the rotor reference speeds obtained from the 'Input Wave' block. Then, the speed errors or differences are fed into an internal PI control in the 'Speed Controller' block to get the reference torque values. After that, the reference torque values will serve as references to the *q*-axis current, I_q*. The simplified equation that relates the reference torque, T* and I_q* is

$$T^* = 1.5\frac{p}{2}\Psi_{PM} I_q^* \tag{4.8}$$

The two 'PI' blocks in Fig. 4.8 are used to control the *q*-axis current and *d*-axis current. The two current references, I_q* and I_d*, are very critical in controlling

the PMSG in order to generate the maximum output power. For this control strategy to work, I_d* must be set to 0. By doing this, the resistive losses are minimized too. The efficiency of the system must be maximum to obtain the maximum output power when the wave height, wave length and depth of rotation axis is between the cut-in and rated value. Therefore, the value of the armature rotational radius has to be optimum too for all values of the wave height, wave length and depth of rotation axis within this working region.

The actual 3-phase stator currents are obtained from the PMSG. These are converted into their *d-q* components in the *abc*-to-*d-q* block. The current components in *d-q* axes are then compared to the references to control the required *d-q* components of the voltage vector through the use of the two PI current controllers. Direct modelling of the 3-phase system by obtaining their circuit equations in 3-phase reference frame is not ideal because this will result in equations with time varying parameters since the self-inductances and mutual-inductances of the machine windings depend mainly on the rotor position. The relationship between a set of *d-q* variables and the corresponding set of 3-phase *abc* variables is provided by the direct-quadrature-zero (*dq0*) transformation. This is often referred as the Park's transformation, where the transformation matrix is represented by *T*:

$$T = \frac{2}{3}\begin{bmatrix} \cos\theta & \cos\left(\theta - \frac{2}{3}\pi\right) & \cos\left(\theta + \frac{2}{3}\pi\right) \\ \sin\theta & \sin\left(\theta - \frac{2}{3}\pi\right) & \sin\left(\theta + \frac{2}{3}\pi\right) \\ \frac{1}{2} & \frac{1}{2} & \frac{1}{2} \end{bmatrix} \tag{4.9}$$

In the case where the 3-phase system is balanced, no *0* component is present, which allows a simplified version of the *d-q* transformation:

$$T = \frac{2}{3}\begin{bmatrix} \cos\theta & \cos\left(\theta - \frac{2}{3}\pi\right) & \cos\left(\theta + \frac{2}{3}\pi\right) \\ \sin\theta & \sin\left(\theta - \frac{2}{3}\pi\right) & \sin\left(\theta + \frac{2}{3}\pi\right) \end{bmatrix} \tag{4.10}$$

The transformation from *abc* to *d-q* variables can be done using:

$$\begin{bmatrix} X_d \\ X_q \end{bmatrix} = T \begin{bmatrix} X_a \\ X_b \\ X_c \end{bmatrix} \tag{4.11}$$

The inverse transformation from *d-q* to *abc* variables is

$$\begin{bmatrix} X_a \\ X_b \\ X_c \end{bmatrix} = T^{-1} \begin{bmatrix} X_d \\ X_q \end{bmatrix} \tag{4.12}$$

where X represents the generator variables, normally the voltage or current. Fig. 4.9 shows the general reference frame for the 3-phase PMSG.

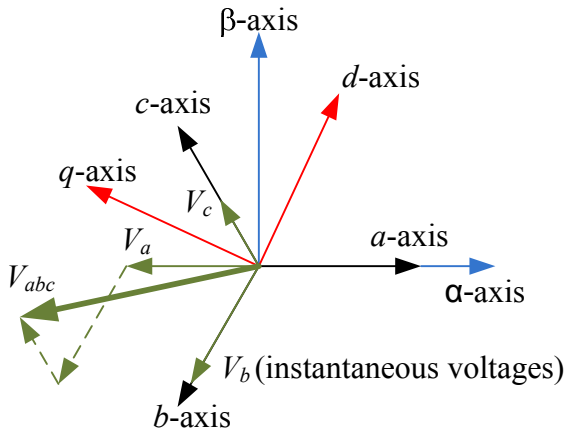

Fig. 4.9. PMSG 3-Phase circuit reference frame.

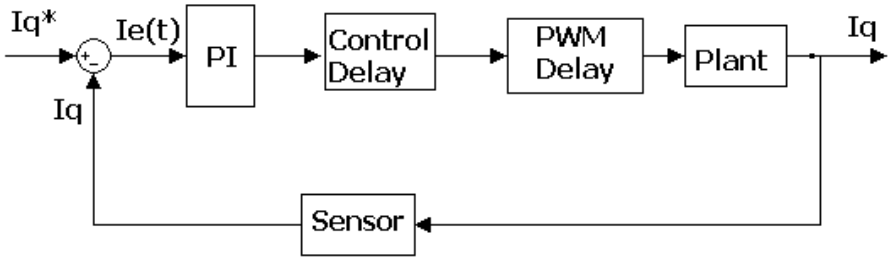

Fig. 4.10. *q*-axis current control loop.

The *q*-axis current control loop is shown in Fig. 4.10 which consists of the PI current controller, delay introduced by the control algorithm, delay introduced by the Pulse Width Modulation (PWM) converter, plant block and delay introduced by the analogue to digital (A/D) conversion of the feedback path through the sensor.

All the delays are represented in the first order transfer function. The delay introduced by the control algorithm has the time constant $T_x = 1/f_x = 0.2$ ms where f_x = 5 kHz is the sampling frequency. The delay due to the PWM converter has the time constant $0.5T_{PWM} = 1/f_{PWM}$ where the PWM switching frequency f_{PWM} = 10 kHz. The D/A conversion delay has the time constant of 0.1 ms.

The transfer function of the proportional integral (PI) controller is

$$PI_q = k_{pi_q} + \frac{k_{ii_q}}{s} = \frac{G(1+\tau s)}{\tau s} \tag{4.13}$$

where k_{pi_q} is the proportional gain, k_{ii_q} is the integral gain of the q-axis current controller, $G = k_{pi_q}$, $G/\tau = k_{ii_q}$, and τ is the integral time of the q-axis current controller. The values of the proportional gain and integral gain are then obtained from the simulation using a trial and error method.

The transfer function of the plant can be obtained since it can be viewed as current passing through a single phase circuit as shown in Fig. 4.11.

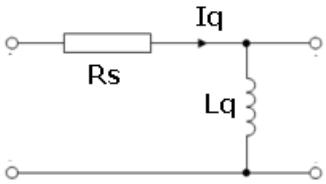

Fig. 4.11. Single phase stator circuit representation.

The current in the circuit is the same in both components since the circuit is in series and it can be calculated from the equation below. This results in a first order transfer function for the plant:

$$I_q = \frac{V_q}{R_s + L_q s} \tag{4.14}$$

$$\frac{I_q}{V_q} = \frac{1}{R_s + sL_q} = \frac{1}{R_s} \times \frac{1}{1 + s\frac{L_q}{R_s}} = \frac{K}{1 + s \times \tau_q} \tag{4.15}$$

where $K = 1/R_s$ and $\tau_q = L_q/R_s$. The transfer function of the plant is

$$\frac{I_d}{V_d} = \frac{1}{R_s + sL_d} = \frac{1}{R_s} \times \frac{1}{1 + s\dfrac{L_d}{R_s}} = \frac{K}{1 + s \times \tau_d} \tag{4.16}$$

where $K = 1/R_s$ and $\tau_d = L_q / R_s$.

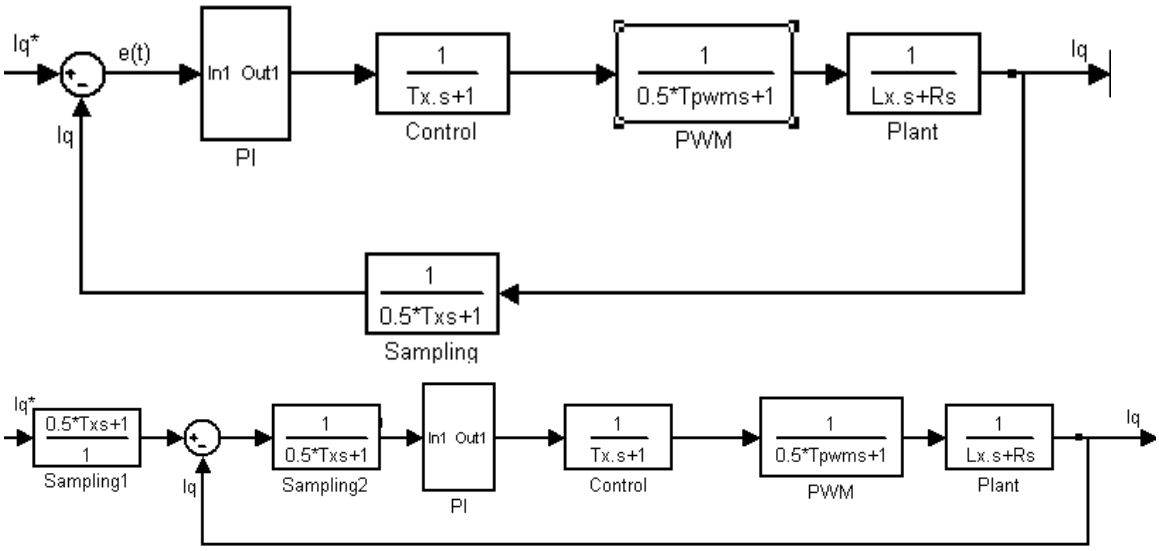

Fig. 4.12. *q*-axis current control loop.

The open loop transfer function is shown in Fig. 4.12 and can be represented by:

$$\begin{aligned} G_{i_q}(s) &= \frac{G\left[\dfrac{1+T_{i_q}s}{T_{i_q}s}\dfrac{K}{\tau_q s+1}\dfrac{1}{T_x s+1}\dfrac{1}{0.5T_x s+1}\dfrac{1}{0.5T_{pwm}s+1}\right]}{\left(1+k_{pi_q}\dfrac{1+T_{i_q}s}{T_{i_q}s}\dfrac{K}{\tau_q s+1}\dfrac{1}{T_x s+1}\dfrac{1}{0.5T_x s+1}\dfrac{1}{0.5T_{pwm}s+1}\right)} \times (0.5T_x s+1) \\ &= \frac{(0.5T_x s+1)G\left(1+T_{i_q s}\right)K}{T_{i_q}s\left(\tau_q s+1\right)\left(T_x s+1\right)\left(0.5T_x s+1\right)\left(0.5T_{pwm}+1\right)+k_{pi_q}K\left(1+T_{i_q}s\right)} \end{aligned} \tag{4.17}$$

The *d*-axis current controller is implemented in a similar way to the *q*-axis current controller.

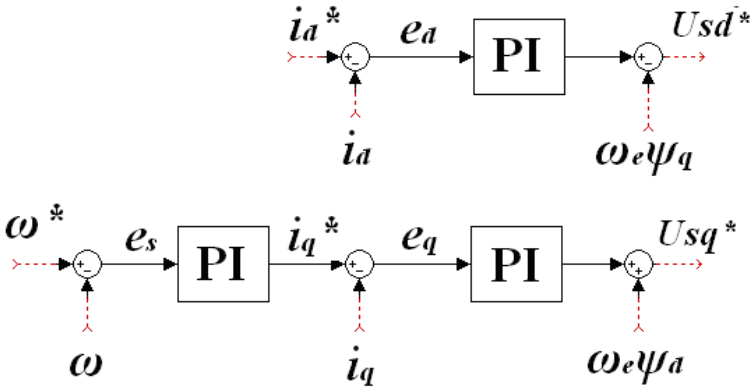

Fig. 4.13. Speed and *d*-*q* axes control.

All the PI blocks implemented in the simulation are shown in Fig. 4.13 where ω is the rotational speed in rpm, ω_e is the rotational speed in rad/s, e_s is the speed error, e_q is the *q*-axis current error, e_d is the *d*-axis current error, $\omega_e\psi_q$ and $\omega_e\psi_d$ are the decoupling factors as shown in Fig. 4.8 and U_{sq}* and U_{sd}* are the voltages for *d*-axis and *q*-axis respectively. The *q*-axis current loop is acting as an inner loop while the speed loop is the outer loop. The speed error is the input for a PI speed controller. The output of the speed controller is the reference signal i_q*. The *q*-*d* axes current errors are the inputs to the other two PI current controllers, and the controllers are used to generate the reference voltages in the *d*-*q* axes to be applied to the generator when it is required. From the stator reference voltage equations in *d*-*q* axes, decoupling factors can be obtained from the voltage equations using:

$$U_{sq}^{*} = R_s i_q + \frac{d\Psi_q}{dt} + \omega_e \Psi_d \tag{4.18}$$

$$U_{sd}^{*} = R_s i_d + \frac{d\Psi_d}{dt} + \omega_e \Psi_q \tag{4.19}$$

The reference voltages in *d*-*q* axes, U_{sq}* and U_{sd}*, are then converted back to 3-phase voltages in the *d*-*q*-to-*abc* block. The voltage applied to the PMSG stator is represented by a 3-phase Controlled Voltage Sources block that is regulated by U_{sq}* and U_{sd}*. The voltages are then transmitted through the Breaker block to control the PMSG speed. A Voltage and Current Measurement block is inserted in between the Breaker block and PMSG to measure the instantaneous voltage and current at the PMSG terminals.

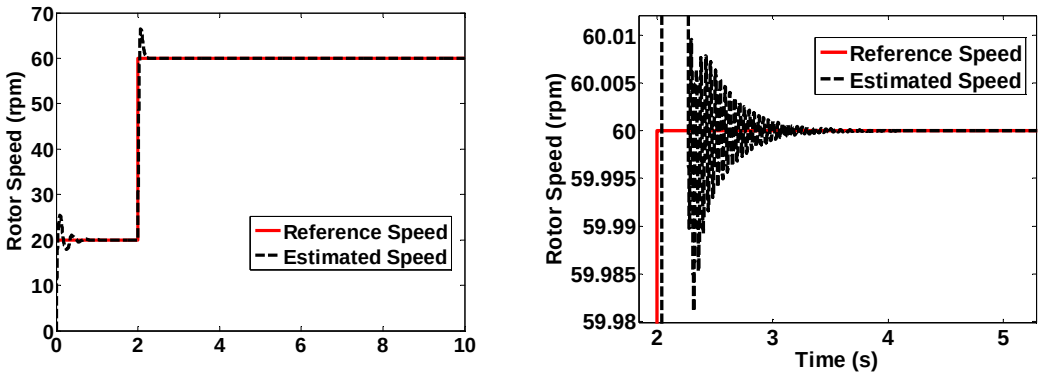

(a) (b)

Fig. 4.14. Rotor speed step response.

Fig. 4.14 shows the rotor speed response for the small lab model. The generator starts with speed 20 rpm and step up to 60 rpm at t = 2 s. This is a step change in waves from 3 s waves to 1 s waves and with low inertia to test the control. The inertia was set to 2.2 kgm^2; at 20 rpm the required torque is -220 Nm, and at 60 rpm the required torque is -660 Nm. In reality the inertia would be higher. The graphs showing the speed response are presented. The graph shows a minimum overshoot and has a settling time of approximately t_s = 1.4 s, which are still acceptable in the actual system. The PMSG is needs to be synchronized with the incident waves so that good response is required; if the cylinder is not synchronized then there will be zero torque (effectively, using synchronous machine terminology, it will "pole slip"). The reference speed is the speed of the incident wave which the generator should be synchronized to and differences in speed will lead to load angle change. Zooming into the graph to observe into more details, it is found that when the speed reference changes, a ripple appears in the rotor speed due to instantaneous change of the wave height or wave period and there is a demand for torque.

4.5.2 Case Study 1: Steady Mechanical Torque for PMSG with 4.1 Ohm Phase Resistance

Fig. 4.15 shows wave power and mechanical torque variations due to a change in wave period and wave height in time. The wave heights targeted are 0.8 m, 0.6 m, and 0.4 m and the wave periods that correspond to the wave heights were chosen as 3 s, 2 s, and 1 s respectively. These result in wave powers of 471 W, 177 W and 39 W. A starting mechanical torque of -225 Nm was initially applied in the simulation, followed by -56 Nm at 4 s and finally -6 Nm is applied to the generator at 7 s. Overall

the simulations run for 8 s. Notice that the negative sign represents the PMSG functioning as generator.

The first set of simulations investigate a series of step changes in speed as shown in Fig. 4.16(a), where the speed is 20 rpm, 30 rpm and 60 rpm. These are the simulation results from the incoming wave power as shown in Fig. 4.15(a). There are three sections (A to C) as illustrated. The results for several variables and parameters are shown. In Figs. 4.16 (b) and (c), I_q and I_d simulations are put forward. These are negative because the motoring convention is used so that the current then lies on the –*q*-axis rather than *q*-axis. I_d is successfully kept at 0 A for the control method to work. The curves for the back EMF and stator current are shown in Figs. 4.16 (d) and (e). Fig. 4.16 (f) shows the zoomed in version of both the back EMF and the stator current. These ensure that sine waves are obtained and the phase difference is 180 degrees. Fig. 4.16 (g) shows the rotor angle in radians. This is carried forward with a negative electromagnetic torque as shown in Fig. 4.18(h). It can be seen that the high resistance machine follows the demanded I_q well. The extreme of a step change is an unlikely scenario since there is considerable inertia in the cylinder and the speed will simply not change virtually instantaneously. The speeds trace the demanded value well. The electromagnetic torques also follow the demand well which illustrates that the Simulink simulation is giving good numerical accuracy. The terminal power of the PMSG is shown in Fig 4.16 (i).

The total power generated by the generator and its efficiency can now be calculated as shown in Table 4.1.

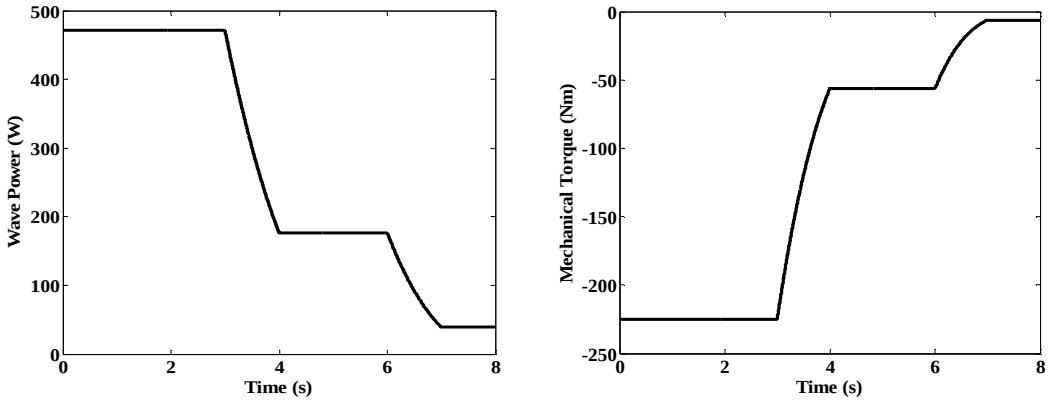

(a) (b)

Fig. 4.15. Ideal waveforms: (a) Wave power absorbed by Bristol Cylinder at 25% conversion rate; and (b) Mechanical torque.

Table 4.1. Generator powers and efficiencies.

	Wave Power (W)	Peak Back-EMF (V)	Peak Stator Current (A)	Power Loses (I^2R)	Simulated Power (W)	Efficiency
Section A	471	40	8	262.4	223	44.59%
Section B	177	60	2	16.4	161	90.97%
Section C	39	121	0.3	0.37	38	97.44%

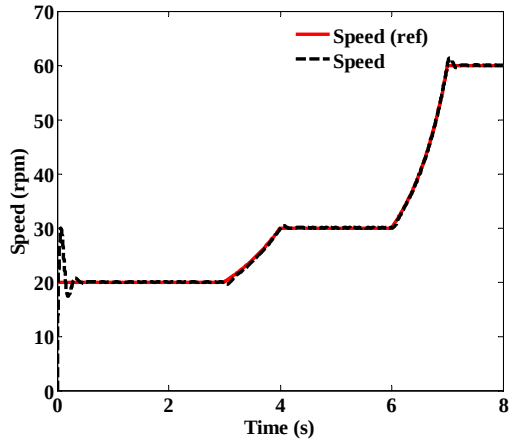

(a)

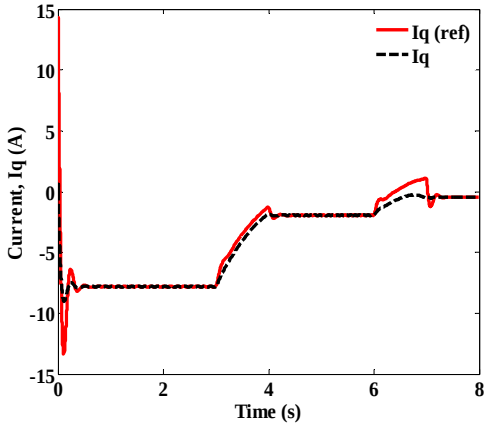

(b)

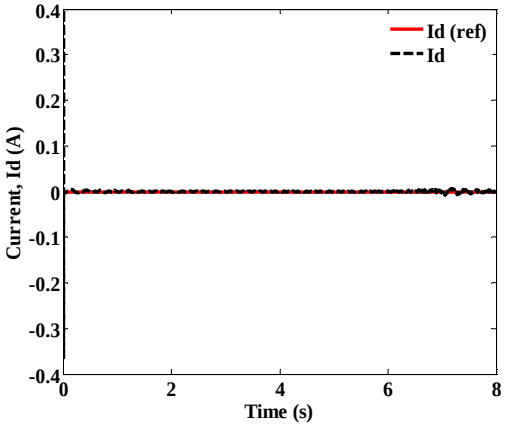

(c)

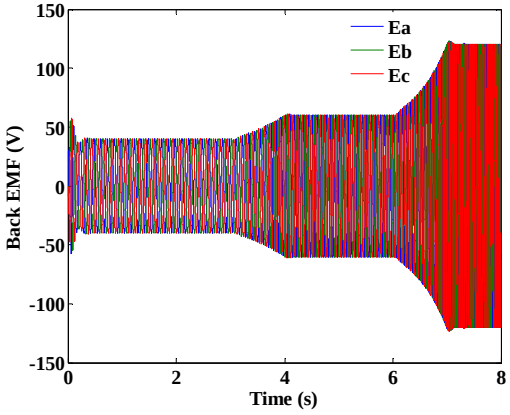

(d)

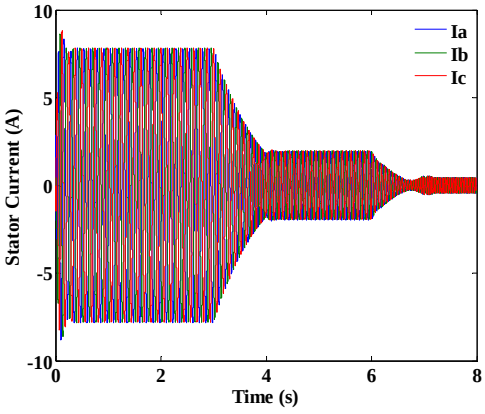

(e)

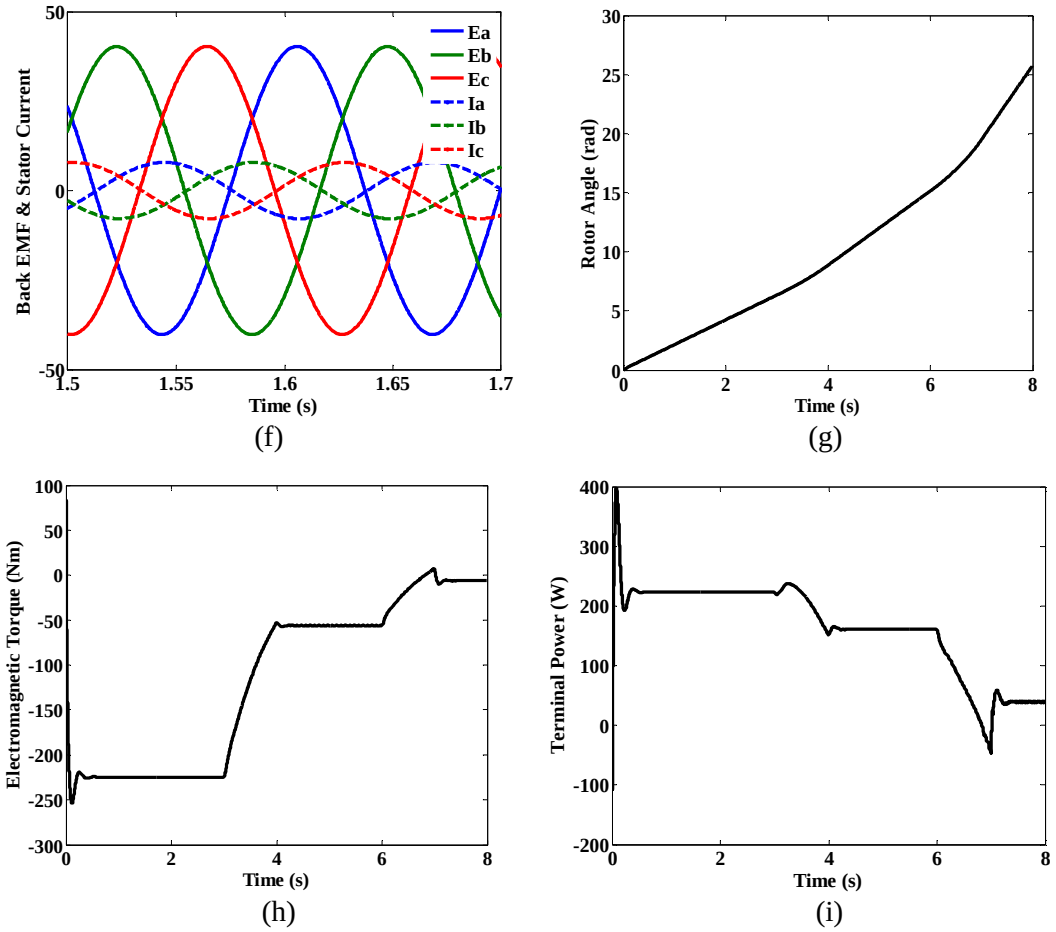

Fig. 4.16. (a) Generator speed; (b) *q*-axis current; (c) *d*-axis current; (d) Back EMF; (e) Stator current; (f) Back EMF and stator current; (g) Rotor angle; (h) Electromagnetic torque; and (i) Terminal power.

4.5.3 Case Study 2: Steady Mechanical Torque for PMSG with 0.41 Ohm Phase Resistance

One of the issues with scaled-down prototypes is the per-unit losses are much higher. In the case of the small device here the copper losses are high. To simulate a machine with much lower per-unit copper losses then it was decided to reduce the phase resistance from 4.1 to 0.41 ohms and repeat the simulations.

The simulations are again investigated using the same set of input wave power, torque and speed as shown in previous case study with smaller value of stator resistance. The results are put forward in Fig. 4.17. This is done in order to attempt to improve the efficiency as discussed earlier. In Figs. 4.17(b) and (c) the I_q and I_d simulations that are shown. Again, these are negative because of the motoring convention and the current then lies on the $-q$-axis rather than q-axis. Notice that the requirement of I_q changes with the change of the resistance. I_d is still maintained at 0 A; it could fluctuate when the speed changes if the control did not react fast enough. Again, the speeds trace the demanded value well.

Table 4.2. Generator powers and efficiencies.

	Wave Power (W)	Peak Back EMF (V)	Peak Stator Current (A)	Power Loses (I^2R)	Simulated Power (W)	Efficiency
Section A	471	40	8.3	28.25	429	91.08%
Section B	177	60	2	1.64	174	98.31%
Section C	39	121	4	6.56	33	84.62%

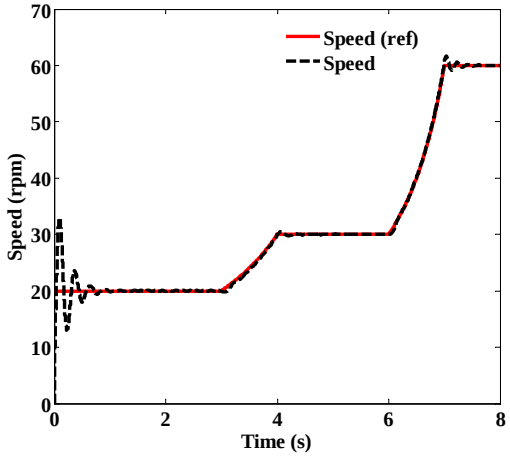
Speed (ref)
Speed
Speed (rpm)
Time (s)

(a)

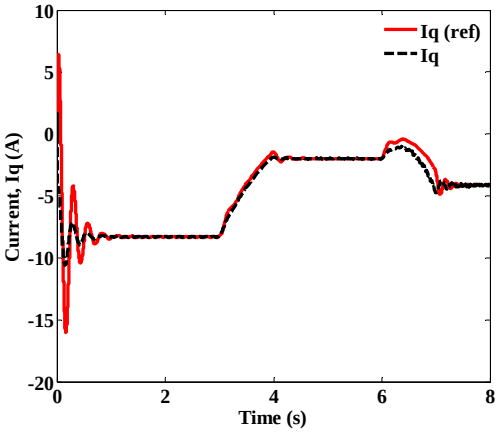
Iq (ref)
Iq
Current, Iq (A)
Time (s)

(b)

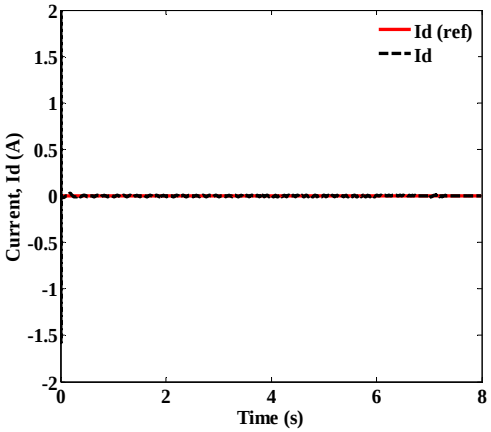
Id (ref)
Id
Current, Id (A)
Time (s)

(c)

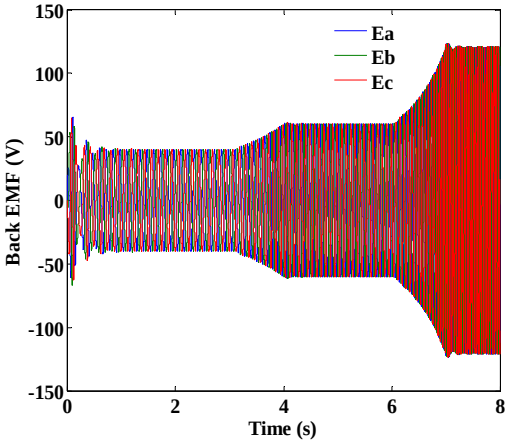
Ea
Eb
Ec
Back EMF (V)
Time (s)

(d)

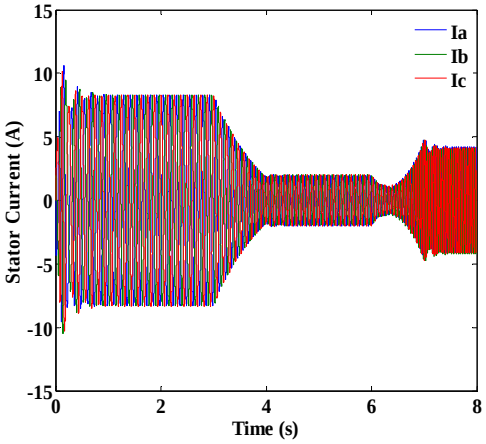
Ia
Ib
Ic
Stator Current (A)
Time (s)

(e)

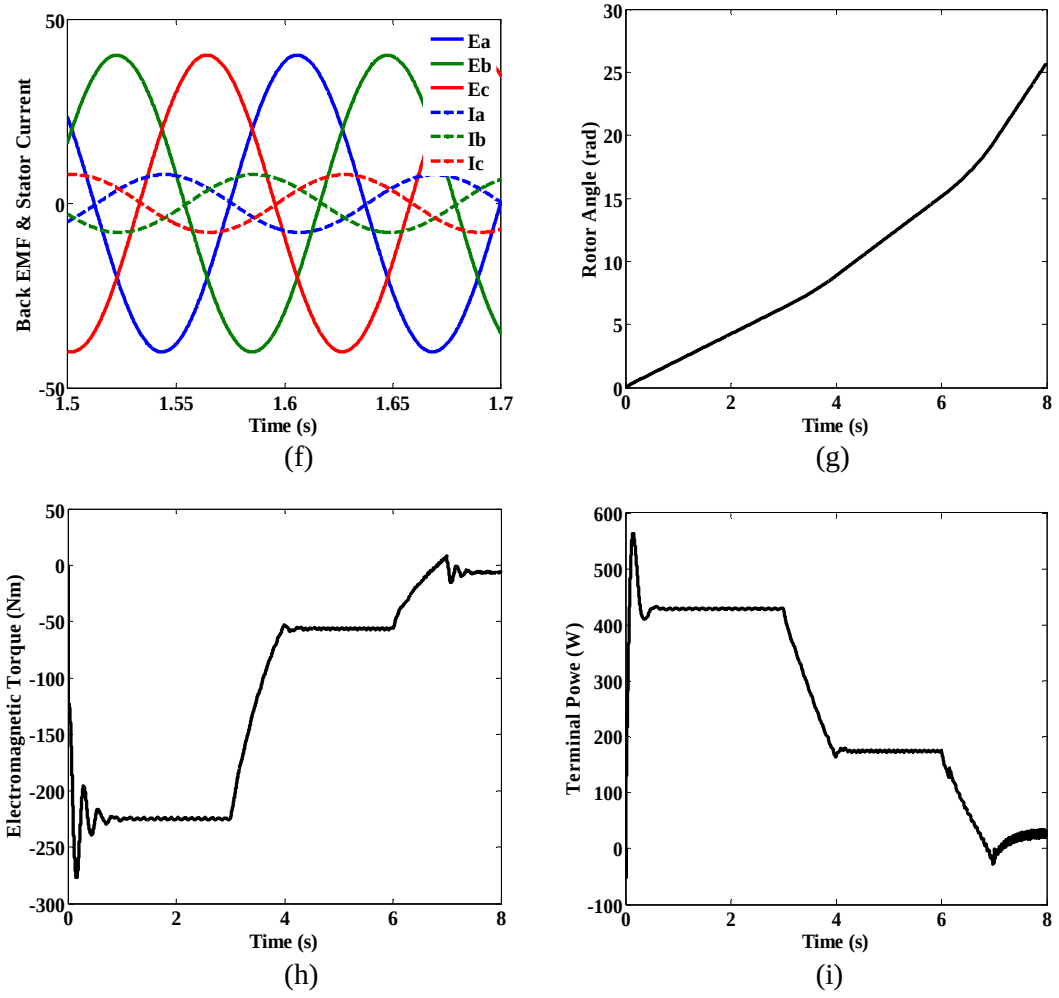

Fig. 4.17. (a) Generator speed; (b) q-axis current; (c) d-axis current; (d) Back EMF; (e) Stator current; (f) Back EMF and stator current; (g) Rotor angle; (h) Electromagnetic torque; and (i) Terminal power.

4.5.4 Case Study 3: Pulsating Mechanical Torque

Pulsating mechanical torque is a more realistic scenario rather than a step change. The wave-energy torque transmitted to the Bristol cylinder is not likely to be constant throughout one full cycle of wave; and real sea waves are not monochromatic. In this simulation we take an extreme case where the wave torque is a sinusoidal about a mean with amplitude that is equal to the mean.

The *q*-axis current, *d*-axis current, back EMF, stator current, rotor angle, terminal power and speed are shown in Fig. 4.18. The pulsating nature of the power deliver is clearly shown. This can be a major issue on large wave energy devices where large capacitor banks may be needed on the DC link to smooth this pulsating power. The *q*-axis current is tracked well with this system.

This simulation illustrates that accurate control is needed and position feedback via an encoder is also important in case pole slipping occurs and the system needs to re-synchronize.

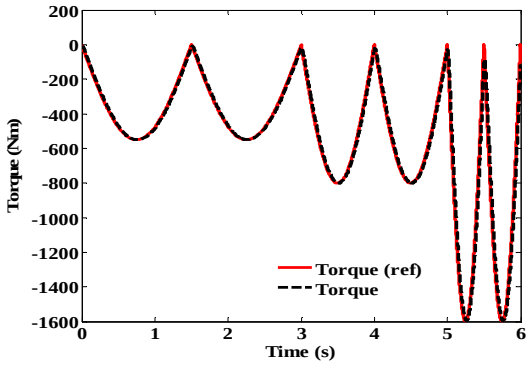

(a)

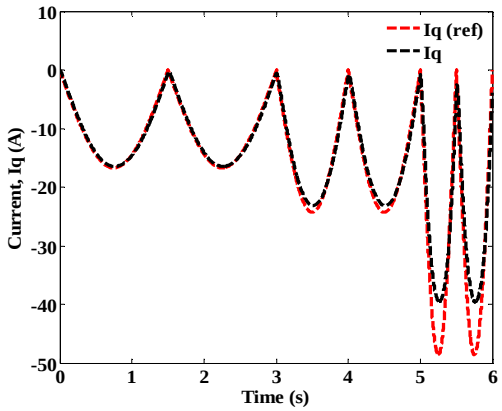

(b)

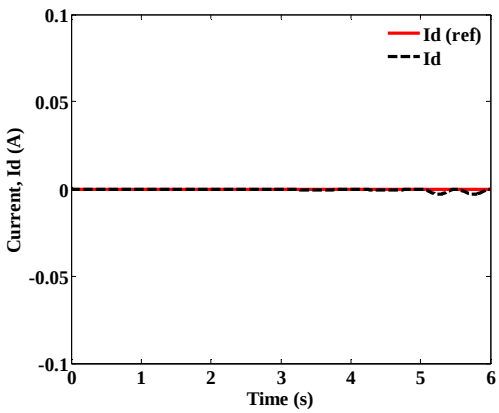

(c)

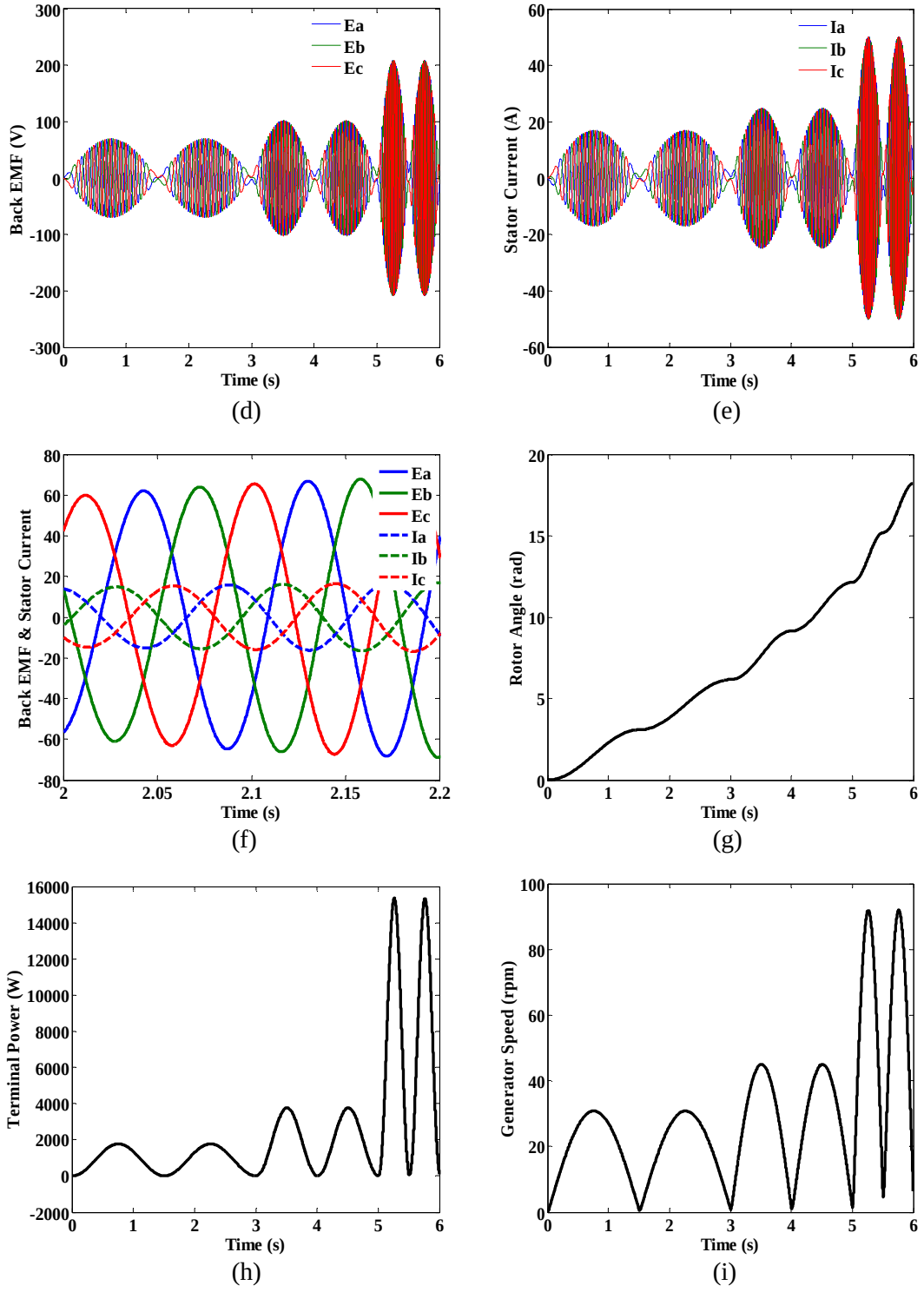

Fig. 4.18. (a) Mechanical torque; (b) *q*-axis current; (c) *d*-axis current; (d) Back EMF; (e) Stator current; (f) Back EMF and stator current; (g) Rotor angle; (h) Terminal power; and (i) Generator speed.

4.6 Speed and Torque Control (The Actual Size Device)

Another set of simulations is needed for the actual size PMSGs. For these case studies, the performance of three types of different PMSGs will be shown. These simulations were performed to compare the performance of generators with different topologies. The parameters of these machines are shown in Table 4.3.

These machines are simulated for the target wave which has a wave-height of 3 m and period of 10 s, and another random wave which has a wave-height of 2 m and period of 8 s. These will give a calculated input power of 1.1 MW at 50% mechanical efficiency and the input mechanical torque of 1.76 MNm from the targeted wave. The load change characteristics are shown in Fig. 4.19. The simulations shown are for only one generator in the Bristol Cylinder.

Table 4.3. Parameters of three different PMSGs.

PMSG	Slotless winding	Slotted winding	Slotted winding reduced size
Rotor diameter (m)	13.34	13.34	10
Axial length (m)	0.438	0.438	0.253
Weight of magnet (kg)	4015	4015	1661
Total weight copper (kg)	1632	3727	1707
Total weight excluding shaft (kg)	48865	48083	20044
Total flux linkage (Wb)	9.069	9.703	8.665
Total phase resistance (ohm)	0.0489	0.0271	0.0216
Total Phase inductance (mH)	14.8	6.3	3.19

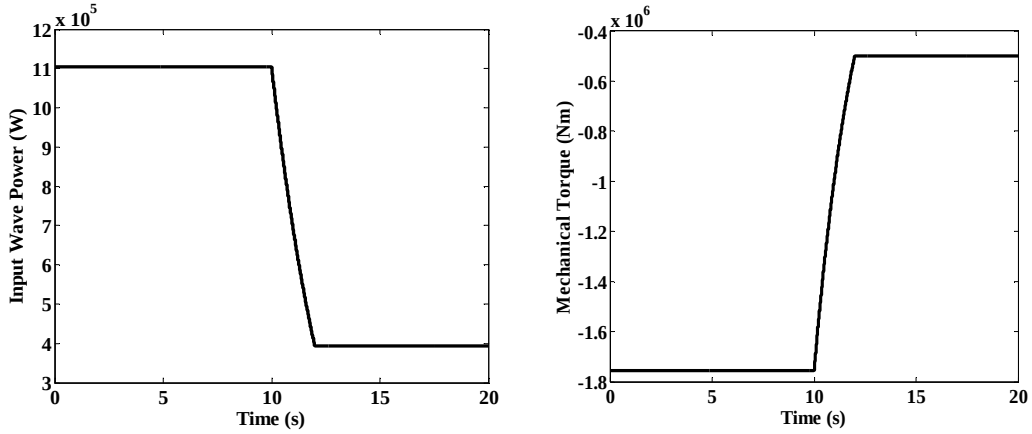

Fig. 4.19. Waveforms (a) Wave power absorbed by Bristol Cylinder at 50% conversion rate (two generators); and (b) Mechanical torque.

From the pulsating torque case studied in previous section, it is found that some assumptions made maybe not as accurate as required. Knowing that the torque may pulsate throughout one full rotation cycle of the Bristol Cylinder and assuming the speed of the PMSG is constant is one of the weaknesses. The fact is that the estimation of the PMSG speed in this complicated case is very difficult. To overcome this weakness, the reference torque is now compared to the electromagnetic (measured) torque of the generator to generate the reference value for I_q. Referring to Fig. 4.8, other control blocks remain the same except for the speed controller which is now changed to the torque controller. The results are shown in the case studies 7, 8, and 9.

4.6.1 Case Study 4: Slotless Winding

The simulation of the full scale device with a slotless winding is carried out in order to study the device performance and its efficiency compared to the lab-scale device. This also enables the working voltage, current and power of the device to be assessed when working in the actual environment.

Fig. 4.20 (a) shows the reference speed and the actual speed of the generator. Starting the generator from stand-still, it is found that the generator will take about 0.22 s to reach the stable speed of 6 rpm. The current for both *q* and *d* axes are shown in Figs. 4.22 (b) and (c) respectively. I_q is found to trace the reference value closely while I_d is maintained at 0 A all the time. The 3-phase stator current and back EMF sets are shown in Figs. 4.22 (d) and (e). The stator current is found to be 1152 A and 328 A and the back EMF is found to be 639 V and 799 V for the first and second wave cycles respectively. Fig. 4.22 (h) shows the electromagnetic torque measured which is approximately equal to -1.76 MNm and -0.5 MNm for the two wave cycles and is approximately equivalent to the input wave torque. The output power, which is the instantaneous terminal power calculated using the equation $V_aI_a+V_bI_b+V_cI_c$, is shown in Fig. 4.22 (i). The resultant power is 1.02 MW and 0.386 MW for the two wave cycles.

The efficiency of the system can be calculated by dividing the instantaneous power by the input wave power (at 50% efficiency), which are 92.73% and 98% for the two wave cycles. With a phase resistance of 0.0489 Ohm, the copper loss was found to be 0.06 MW for the first wave cycle, which is about 5.45% of the total wave input power. The copper loss for the second wave cycle is negligible.

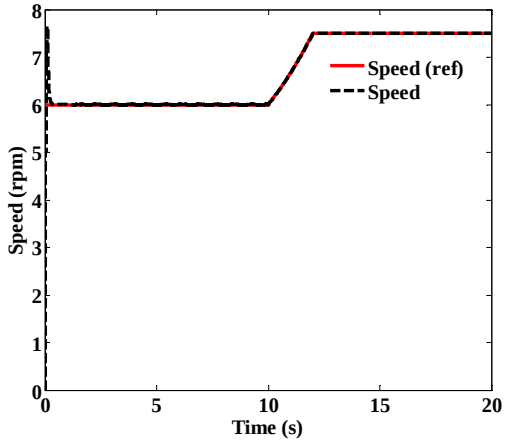
Speed (ref)
Speed
Speed (rpm)
Time (s)

(a)

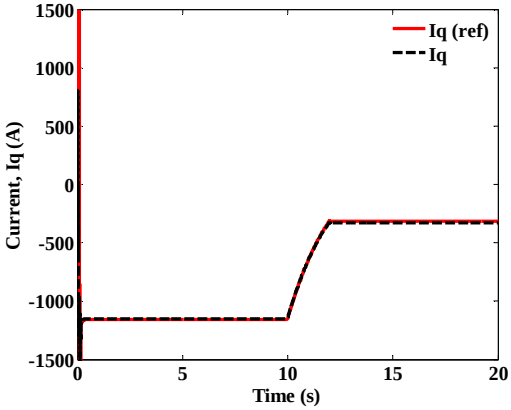
Iq (ref)
Iq
Current, Iq (A)
Time (s)

(b)

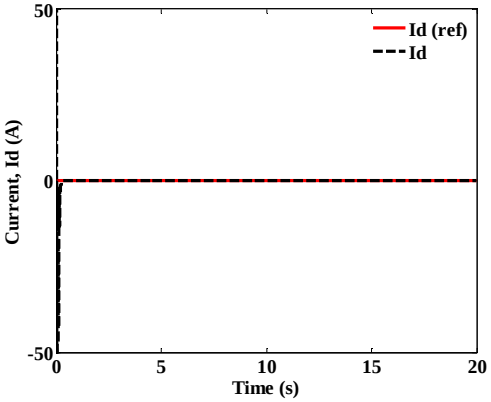
Id (ref)
Id
Current, Id (A)
Time (s)

(c)

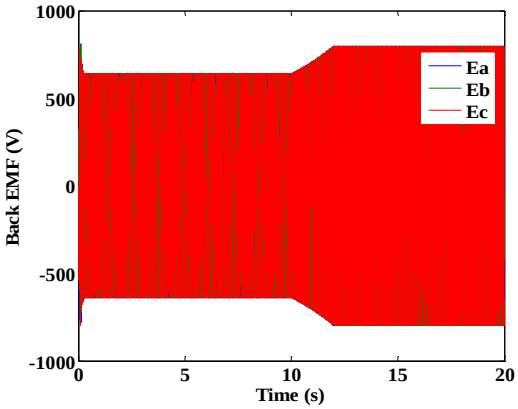
Ea
Eb
Ec
Back EMF (V)
Time (s)

(d)

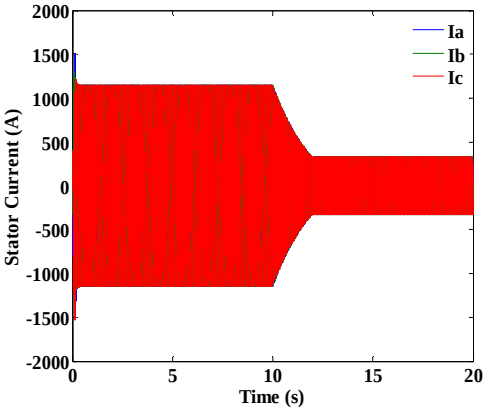
Ia
Ib
Ic
Stator Current (A)
Time (s)

(e)

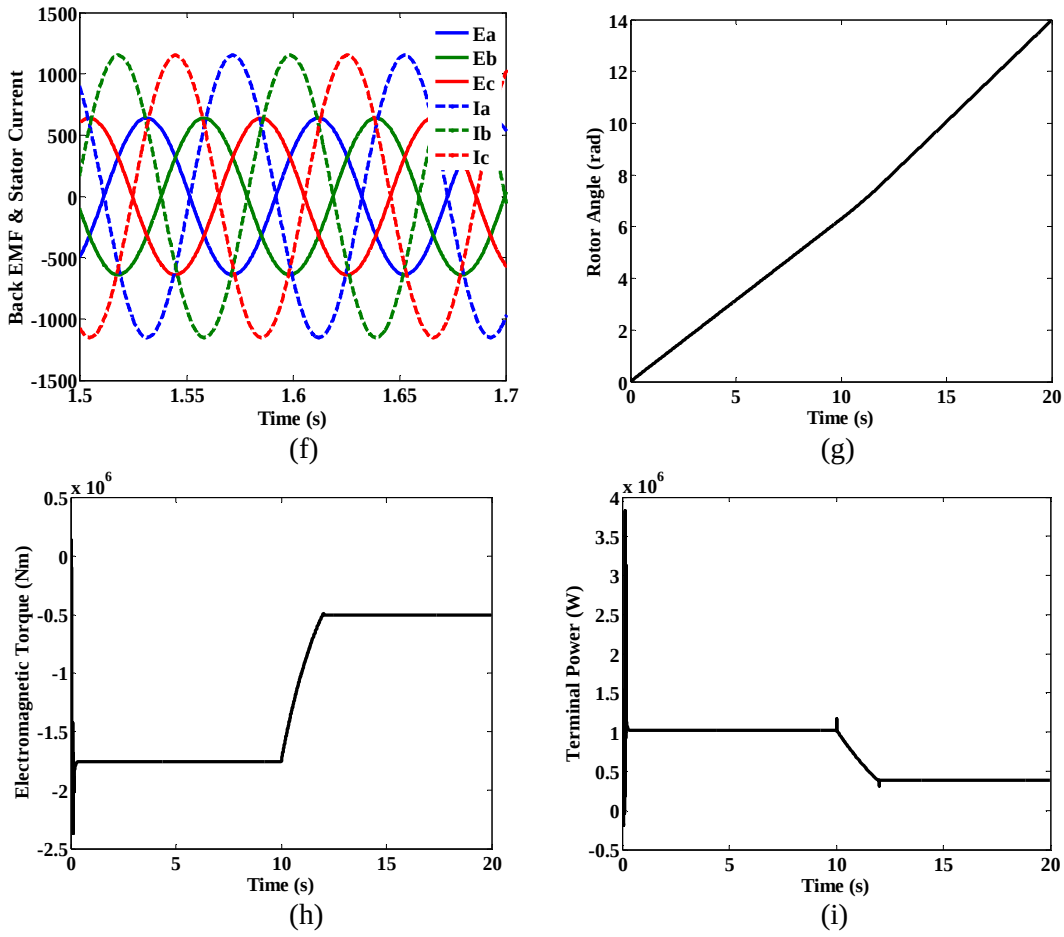

Fig. 4.20. (a) Generator speed; (b) *q*-axis current; (c) *d*-axis current; (d) Back EMF; (e) Stator current; (f) Back EMF and stator current; (g) Rotor angle; (h) Electromagnetic torque; and (i) Terminal power.

4.6.2 Case Study 5: Slotted PMSG

This case study is done to compare the slotted PMSG configuration which is another alternative configuration for the Bristol cylinder. The performance of this PMSG will be compared to the slotless PMSG.

The same simulation was carried out for the slotted PMSG. Fig. 4.21 (a) shows the speed of the reference speed and the actual speed of the generator. Again, the generator was started from stand-still and this time it is found that the generator took about 0.18 s to reach the stable speed of 6 rpm. Fig. 4.21 (b) and (c) show the variation of I_q and I_d respectively. I_q tracks the reference value closely while I_d is maintained at 0 A. The 3-phase currents are shown in Fig. 4.21(d) and the peaks are found to be 974 A and 277 A. In Fig. 4.21 (e) the peak back EMFs are found to be 756 V and 945 V. These are for the two different loadings and speeds. Fig. 4.21 (h) shows the electromagnetic torques for these two operating points which are approximately -1.76 MNm and -0.5 MNm and are equivalent to the input wave torque. The output power, which is again the instantaneous terminal power calculated using the equation $V_aI_a+V_bI_b+V_cI_c$, is shown in Fig. 4.21 (i). The resultant power is 1.07MW and 0.39 MW for the two wave cycles. The efficiency of the system is 97.27% for the first wave cycle. With a phase resistance of 0.0271 Ohm, the copper loss is 0.03MW, which is 2.73% of the total wave input power for the first wave cycle. The second cycle again is negligible.

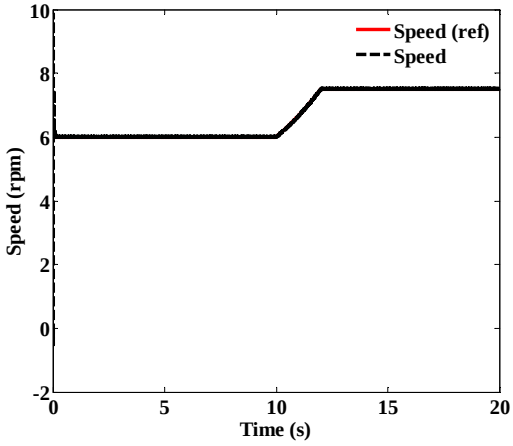
Speed (ref)
Speed
Speed (rpm)
Time (s)

(a)

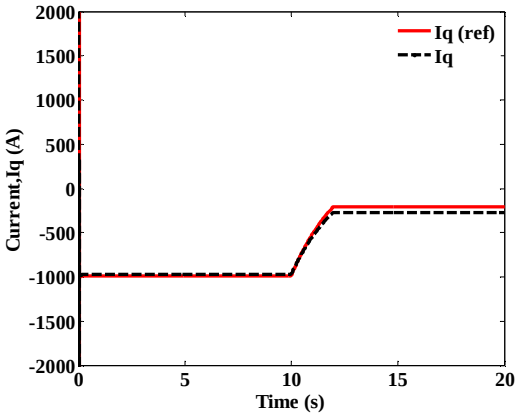
Iq (ref)
Iq
Current,Iq (A)
Time (s)

(b)

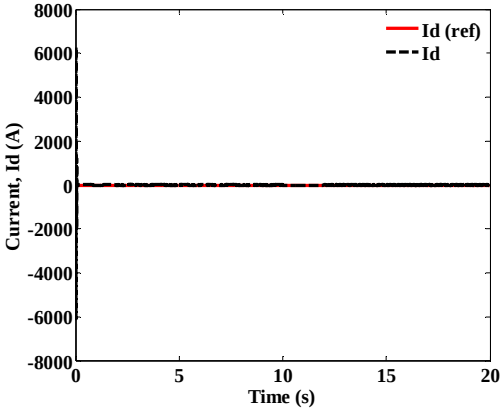
Id (ref)
Id
Current, Id (A)
Time (s)

(c)

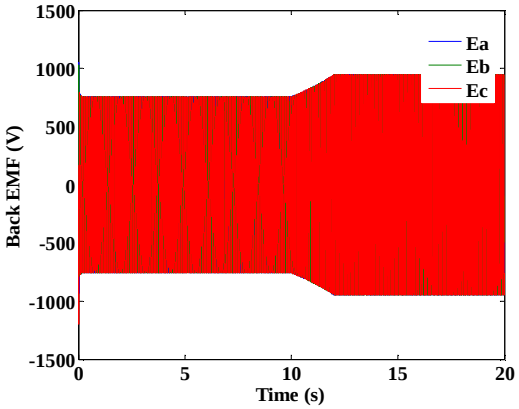
Ea
Eb
Ec
Back EMF (V)
Time (s)

(d)

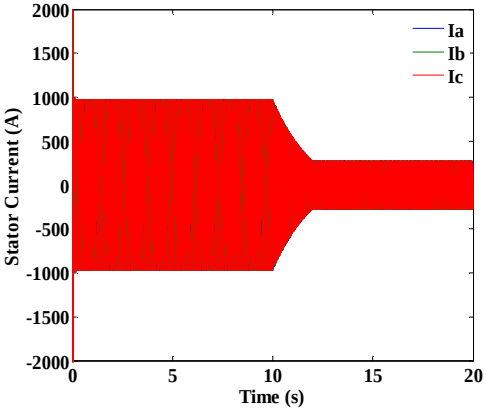
Ia
Ib
Ic
Stator Current (A)
Time (s)

(e)

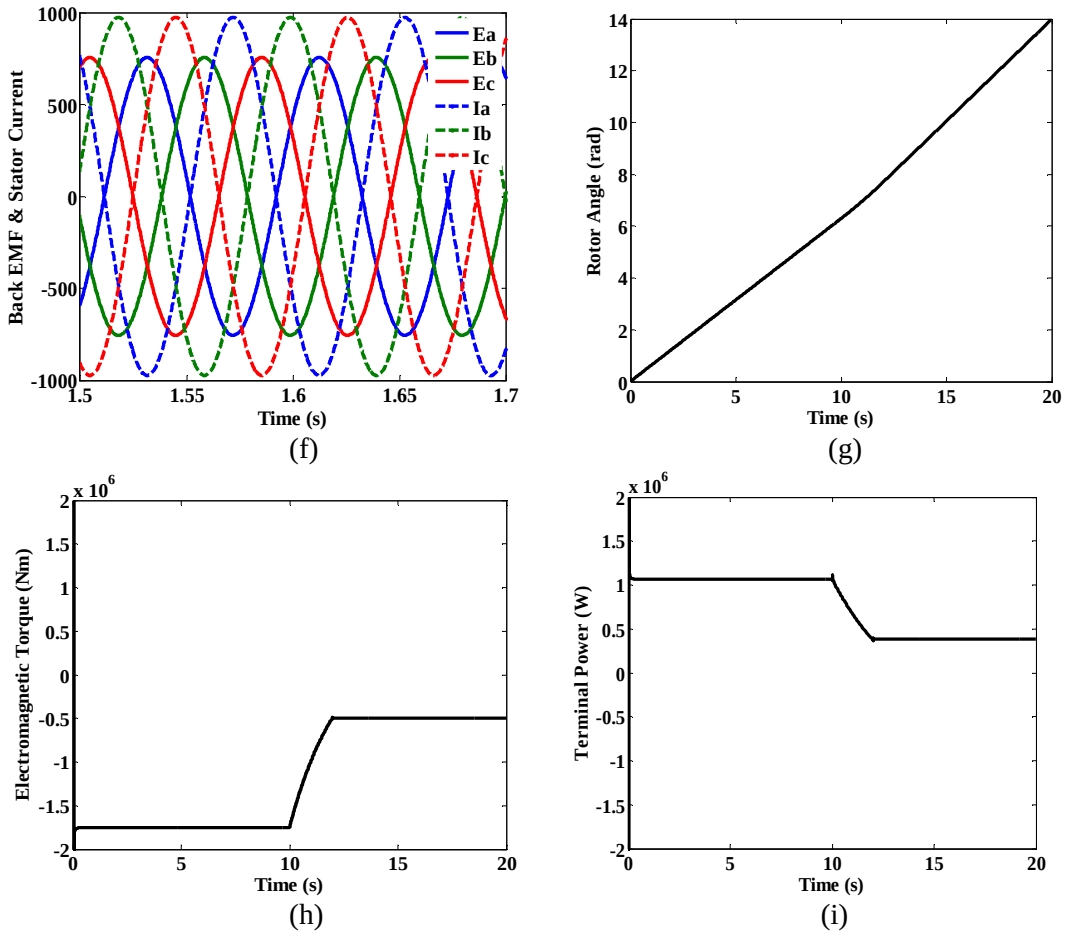

Fig. 4.21. (a) Generator speed; (b) *q*-axis current; (c) *d*-axis current; (d) Back EMF; (e) Stator current; (f) Back EMF and stator current; (g) Rotor angle; (h) Electromagnetic torque; and (i) Terminal power.

4.6.3 Case Study 6: Slotted Winding (reduced size)

This case study is performed to study to possibilities of reducing the size of the slotted PMSG because this will reduce the weight and cost of the PMSG and the overall performance may be improved.

The same scenario as the last two simulations is applied to the reduced size generator. Fig. 4.22 (a) shows the speed of the reference speed and the actual speed of the generator. This time the start time from stand-still is 0.11 s to a stable speed of 6 rpm. This is to be expected since the machine is smaller. Fig. 4.22 (b) and (c) show the current components and again I_q traces the reference value closely while I_d is zero. The 3-phase stator currents and back EMFs in Figs. 4.22 (d) and (e) show a peak stator current of 1151 A and the peak back EMF of 671 V. Fig. 4.22 (h) shows the electromagnetic torque which is 1.76 Nm. The instantaneous output power is shown in Fig. 4.24 (i) and averages to about 1.04 MW. The efficiency is 94.55%. With a phase resistance of 0.0216 Ohm, the copper loss is 0.04 MW, which is about 3.9% of the total wave input power.

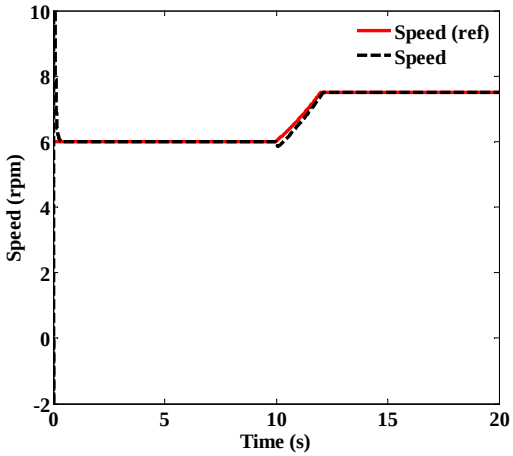

(a)

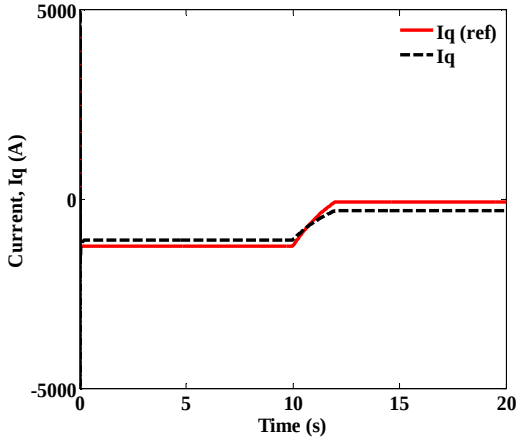
Iq (ref)
Iq
Current, Iq (A)
Time (s)

(b)

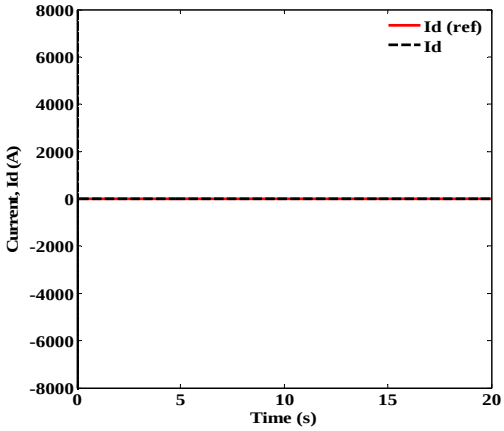
Id (ref)
Id
Current, Id (A)
Time (s)

(c)

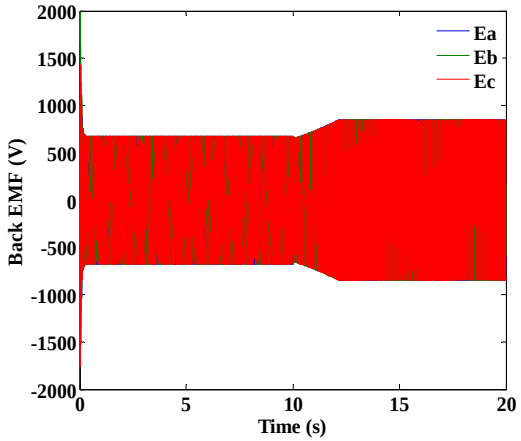
Ea
Eb
Ec
Back EMF (V)
Time (s)

(d)

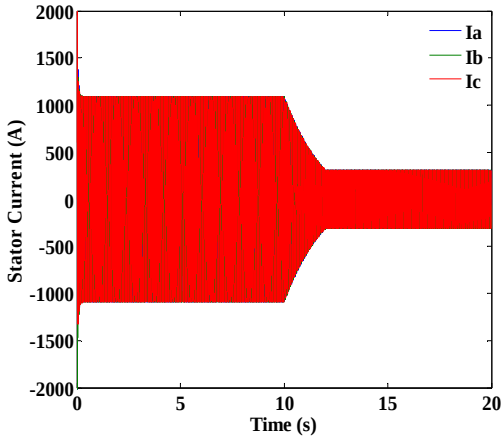
Ia
Ib
Ic
Stator Current (A)
Time (s)

(e)

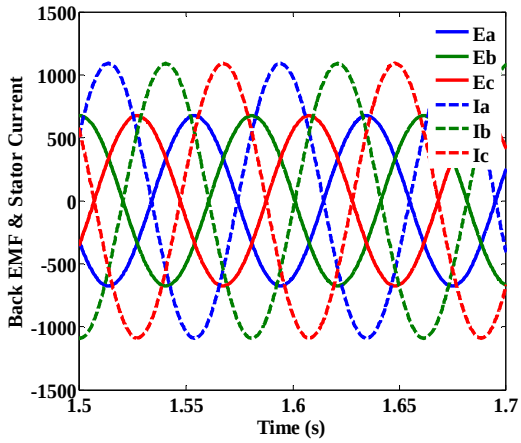
Ea
Eb
Ec
Ia
Ib
Ic
Back EMF & Stator Current
Time (s)

(f)

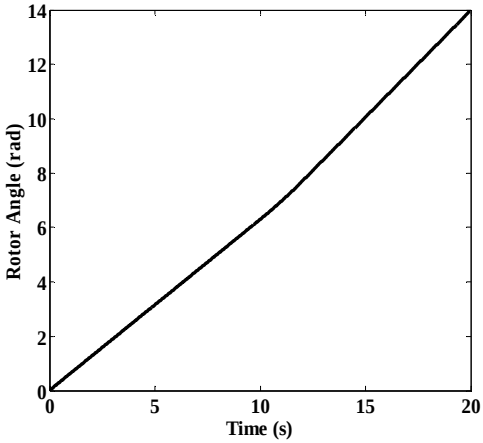
Rotor Angle (rad)
Time (s)

(g)

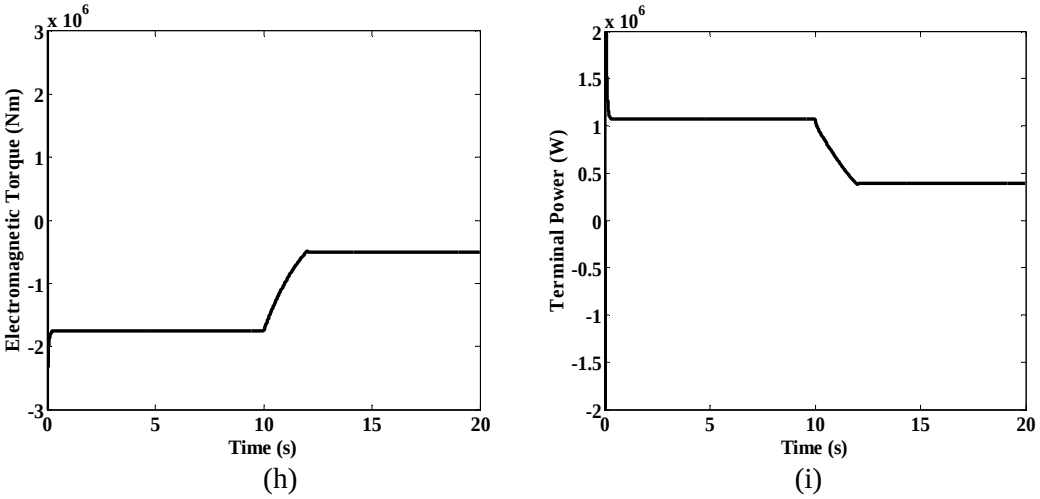

(h) (i)

Fig. 4.22. (a) Generator speed; (b) *q*-axis current; (c) *d*-axis current; (d) Back EMF; (e) Stator current; (f) Back EMF and stator current; (g) Rotor angle; (h) Electromagnetic torque; and (i) Terminal power.

4.6.4 Case Study 7: Slotless Winding (pulsating torque)

In this simulation we take an extreme case where the wave-energy torque is a rectified sine-wave. The pulsating nature of the power deliver is clearly shown in Fig. 4.23. This can be a major issue for a large wave energy device where a large capacitor bank may be needed on the inverter DC link to smooth this pulsating power. The torque and *q*-axis current are tracked well with this system. The rotor angle is shown and it does reach about 6.2 rad at 10 s, which is one full cycle rotation of 360 degree. The speed of the generator is shown for completeness.

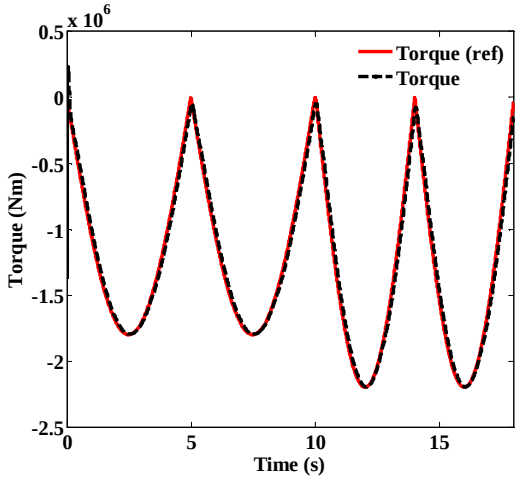

(a)

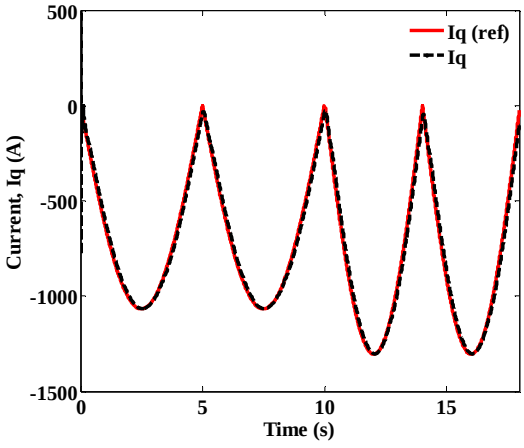

(b)

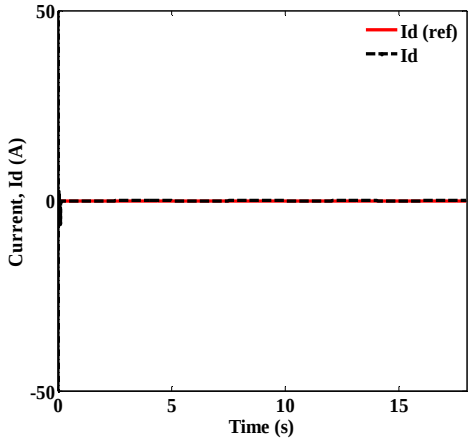

(c)

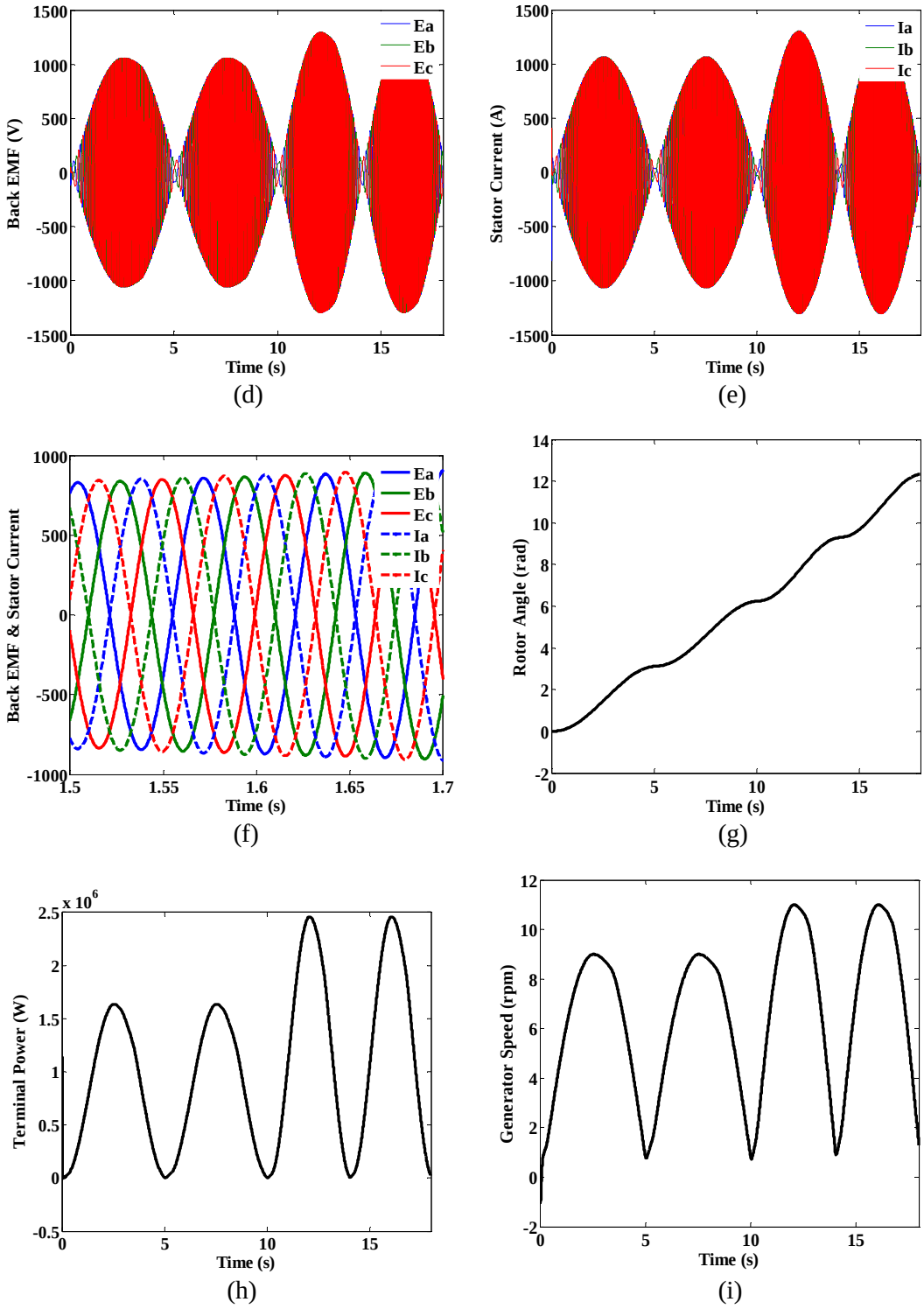

Fig. 4.23. (a) Mechanical Torque; (b) *q*-axis current; (c) *d*-axis current. (d) Back EMF. (e) Stator current; (f) Back EMF and Stator current; (g) Rotor angle; (h) Terminal power; and (i) Generator speed.

4.6.5 Case Study 8: Slotted Winding (pulsating torque)

In this simulation we repeat the same pulsating torque simulation as in previous section. Again, the pulsating nature of the power deliver is clearly shown in Fig. 4.24 (a) and the torque and *q*-axis current are tracked well with one compete revolution simulated in 10 s.

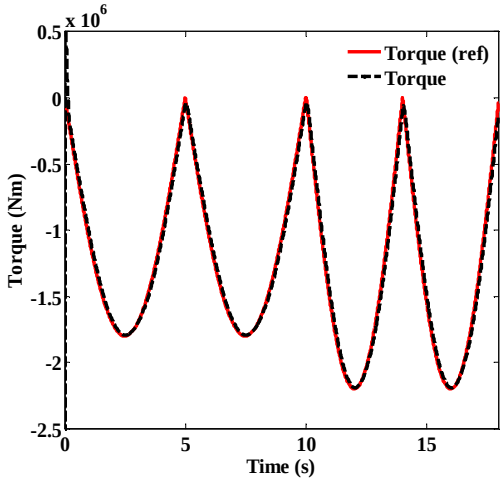

(a)

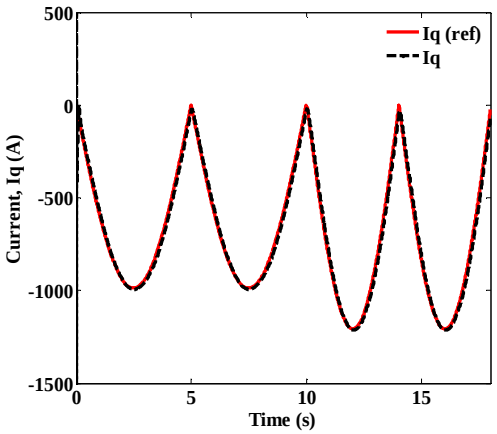

(b)

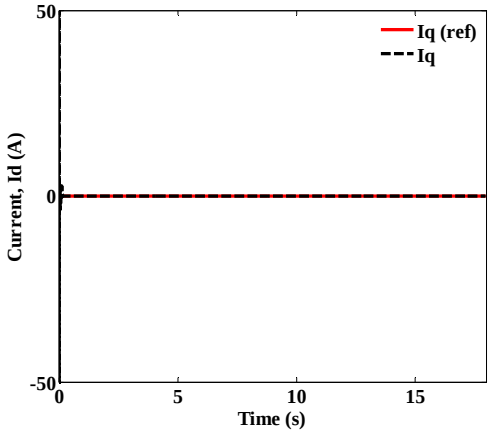

(c)

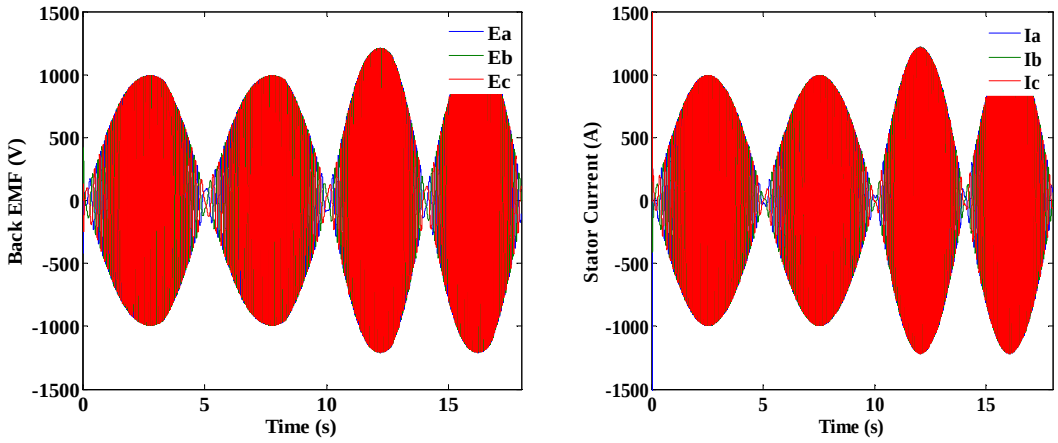

(d)

(e)

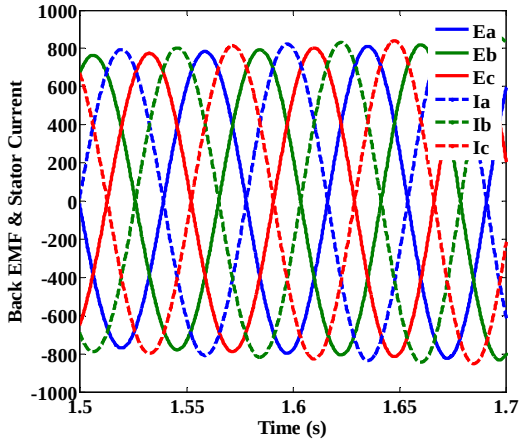

(f)

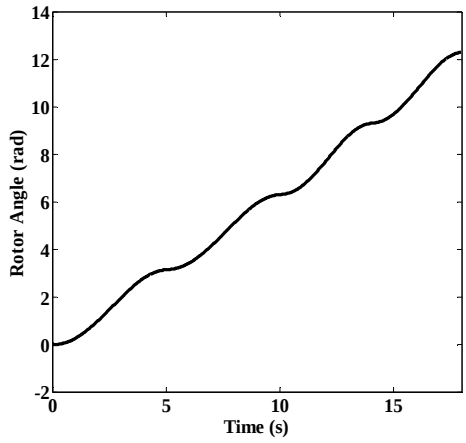

(g)

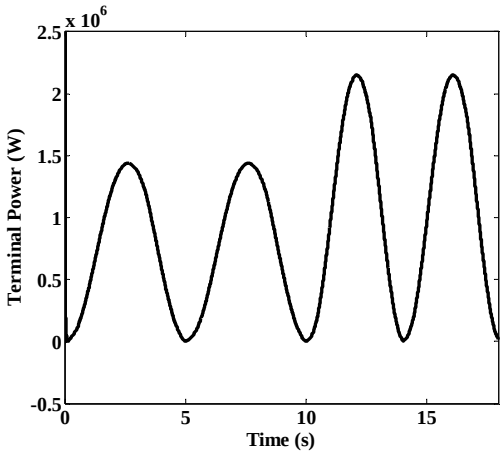

(h)

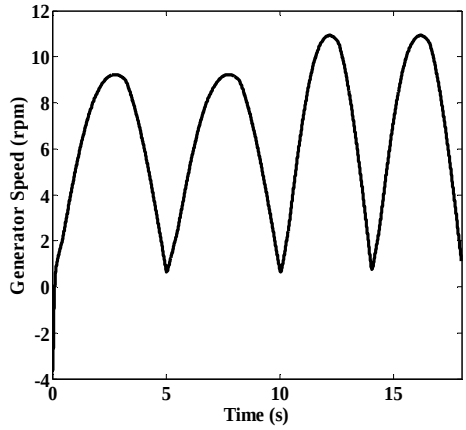

(i)

Fig. 4.24. a) Mechanical Torque; (b) *q*-axis current; (c) *d*-axis current; (d) Back EMF; (e) Stator current; (f) Back EMF and stator current; (g) Rotor angle; (h) Electromagnetic torque; and (i) Terminal power.

4.6.6 Case Study 9: Slotted Winding (reduced size-pulsating torque)

The reduced size machine is simulated here with pulsating torque in a similar fashion to the previous two simulations and one revolution is completed in 10 s. Again the current and torque track the reference value well. It should be pointed out that as the rotation progresses the speed will vary as there is a change in effective "load angle" with respect to the wave. Hence the mechanical angle characteristic is not linear with respect to time. However, the generator appears to be in synchronism.

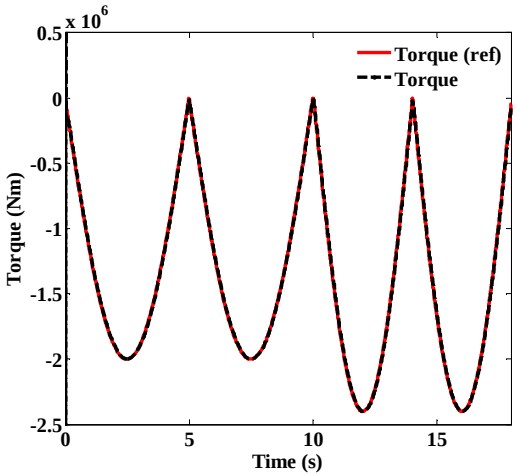

(a)

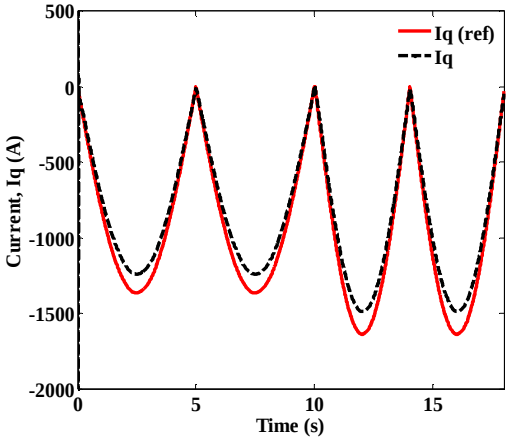

(b)

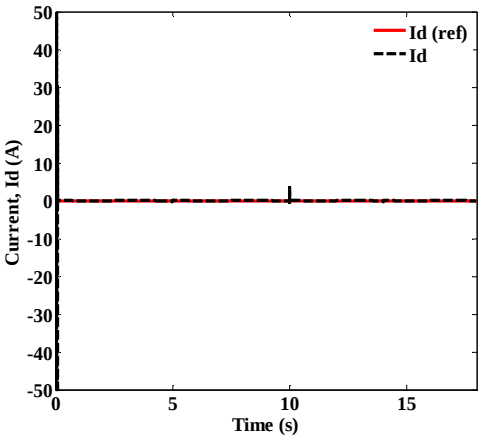

(c)

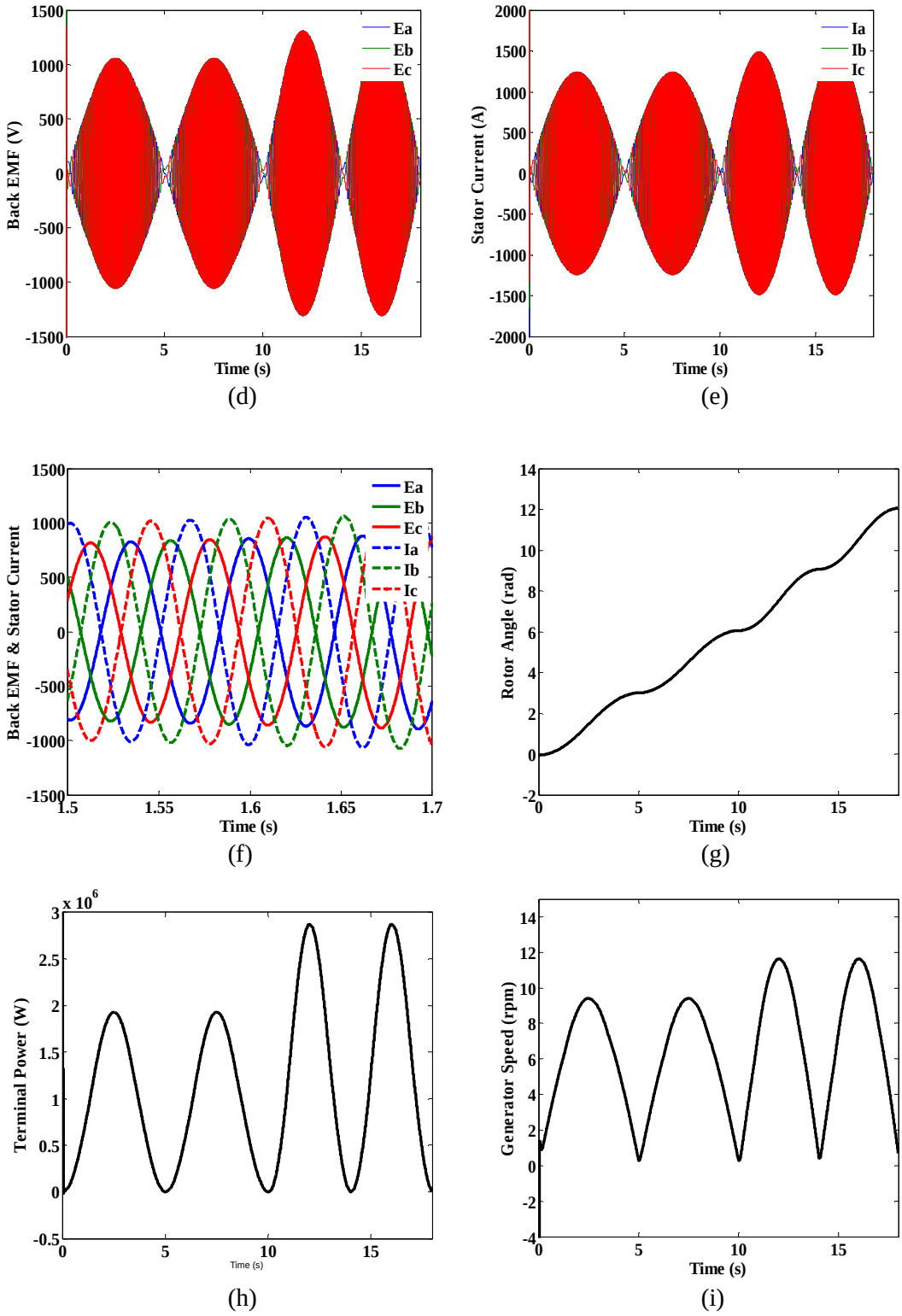

Fig. 4.25. (a) Mechanical Torque; (b) *q*-axis current; (c) *d*-axis current; (d) Back EMF; (e) Stator current; (f) Back EMF and stator current; (g) Rotor angle; (h) Electromagnetic torque; and (i) Terminal power.

4.7 Summary of Case Studies

Case study 1 shows the simulations for the lab scale device with higher resistance compared to case study 2. This can be achieved by reducing the number of winding turns without affecting the back EMF or by using lower resistance copper wires. As expected, the performance of the generator with lower winding resistance is better. It has lower copper loss, and high efficiency compared to generator with higher winding resistance. The simulations for case study 3 are done using the 4.1 Ohm generator winding resistance. The difference between the case 1 and case 3 is the expected incident wave power. According to the theory, wave power is treated as constant source of power supply throughout the whole wave period. In practical, it is found that constant wave power is difficult and the pulsating wave power is more practical. This does make the study more complex. In case 1, the power generated is almost constant throughout a wave period. In case 3, the power generated is pulsating, so large capacitor back may be needed to convert this into smooth DC liked power.

Case studies 4, 5, and 6 studies the performance of the actual sea going device. Case study 4 shows the performance of the slotless winding generator while case study 5 shows the performance of a comparable slotted winding generator. The phase resistance of the slotted PMSG is lower. The output power and the efficiency of the slotted PMSG are higher, and the copper loss lower. However, the performances of the slotless PMSG are still comparable to the slotted PMSG. Even though the performance for the slotted PMSG is more desirable, technically there will be issue of slotting so many copper in the limited space in the stator winding slot. Comparing the slotted PMSG with the reduced size version of its own which is shown in case study 6, the efficiency of the reduced size slotted PMSG is lower and the copper losses is higher. Hence, the performance of the slotted PMSG of original size is more desirable.

The performance of the lab scale slotless winding can be compared to the actual size device too. It is found that, the efficiency of lab scale device is lower compared to the actual size device. Even though the copper loss is higher in the actual size PMSG, it is almost negligible due to the high amount of power generated.

Case studies 7, 8, and 9 show the performance of the actual size device with the pulsating incident wave power. Again it shows pulsating output power. The efficiency of the system remain equivalent to the results of case studies 4, 5, and 6.

Chapter 5

GRID SIDE CONVERTER CONTROL

5.1 Introduction

The space vector PWM rectifier is connected to the power grid through a PWM inverter. Thus, we will refer the PWM inverter as the grid side converter. In reality these are likely to be two back-to-back PWM inverters. The grid side converter is connected to the generator side converter through the DC link. Both the converters are voltage source converters and linked by the DC link or bus. The results in the previous chapter clearly show that there will be pulsating power and to maintain constant DC link voltage, or constrain it to an operating range, then DC link energy storage via a capacitor bank may be needed in order to deliver steady power to the grid. The mean output power should be equal to the mean input power to keep the mean link voltage constant.

The main goal for grid side converter control is to regulate the output power of the wave energy system so that the capacitor voltage will remain within a constrained range. A wave-energy generator can be treated as either a generator bus (PV) or load bus (PQ) in a similar fashion to other power plants [168]. In a PV bus, the voltage of the bus is known and in PQ bus the reactive power fed to the grid is known. Therefore another goal of the grid side control is to regulate the reactive power or the bus voltage. Bus voltage and delivered reactive power are dependent to each other.

It can be concluded that the objectives of the grid side control are to keep the capacitor voltage within a constrained range and to provide reactive power to the grid simultaneously. The capacitor voltage varies according to the incoming power from the wave-energy generator and the output power given to the grid. So the control algorithm must be able to detect the voltage variation and keep the grid and generator AC voltages steady while charging and discharging the DC link capacitor. To boost the generator voltage, the controlled rectifier can supply reactive power to it. But this

too requires energy storage on the DC link. The control algorithm must also allow the grid side converter to supply the reactive power needed by the grid.

Various control methods have been proposed for the purpose of transferring maximum power to the grid [169-173]. All the methods control different generator or motor functions under different conditions.

5.2 Grid Codes Review

Early renewable energy plants in Europe were connected to the distribution network. However in recent years the trend is moving towards connection to the transmission networks directly [174]. Different network voltage levels have specific requirements when connecting to a renewable energy plant. Power flow and energy plant behaviour have a great influence on the grid stability. Grid codes for connecting generators to the grid are developed by grid operators. These have been specified for renewable energy plants and they have to be met by the system manufacturers. The codes grid integration of wave-energy generators are still in early stage development because there are few commercial wave farms. The objectives of the code requirements are to insure the security of supply, reliability and quality. Generally, the grid code requirements are related to active and reactive power control, frequency control, and voltage control and quality. In addition, tap changing transformers, fault ride through capability, renewable energy modelling and verification, communications and external control are all considered. In the following section a review for the UK requirements for electrical networks is presented based on the National Grid Code [175]. The voltage levels of the electrical network in UK are shown in Table 5.1.

To review the active power requirements: the incremental active power steps, from no load to rated power, which a generator can instantaneously supply without causing it to trip or go outside the frequency range of 47.5 to 52 Hz or other pre-agreed frequency, must be determined; and the time for each incremental must be provided. Because sea waves cannot be controlled, the output power of the generator must be controlled to increase or decrease the output power to support the system frequency during unexpected demand [178].

Table 5.1. Voltage levels for electrical network in UK [176][177].

Network	Line Voltage	National Grid	Scottish & Southern	Scottish Power	N. Ireland
Transmission	400kV	√	-	√	-
	275kV	√	√	√	√
	132kV	-	√	√	-
	110kV	-	-	-	√
Distribution	33kV	√	√	√	√
	22kV	√	√	√	√
	11kV	√	√	√	√
	6.6kV	√	√	√	√
	415V	√	√	√	√
	230V	√	√	√	√

The reactive power is typically controlled in a given range. The grid codes state various ways regarding the control capability of reactive power. The generator capability in terms of controlling the reactive power depends on the generator type. Another main code issue is the power quality. This is determined by a set of parameters of the generator that will have impact the voltage quality of electricity network. The related parameters are the active and reactive power as mentioned earlier, voltage fluctuations, switching operations, harmonic current and the others.

5.3 Grid Side Converter Control

Fig. 5.0 shows the block diagram of the grid side converter control technique. It is critical for the grid converter control to respond to the demand for reactive power and to keep the capacitor voltage constrained simultaneously. There are three main control techniques which are integrated into the grid side converter control. The first is the control of capacitor voltage. It is assumed in this part that the grid voltage is the reference and constant:

$$v_g = |v_g| \angle 0 \tag{5.0}$$

Therefore, the active power, P_g and reactive power, Q_g can be derived from

$$P_g = \frac{3}{2}(v_{qg} i_{qo} + v_{dg} i_{do}) \tag{5.1}$$

$$Q_g = \frac{3}{2}(v_{qg} i_{do} + v_{dg} i_{qo}) \tag{5.2}$$

Since $v_{qg} = |v_g|$ and $v_{dg} = 0$ then (5.1) and (5.2) can be simplified to [179]:

$$P_g = \frac{3}{2} v_{qg} i_{qo} \tag{5.3}$$

$$Q_g = \frac{3}{2} v_{qg} i_{do} \tag{5.4}$$

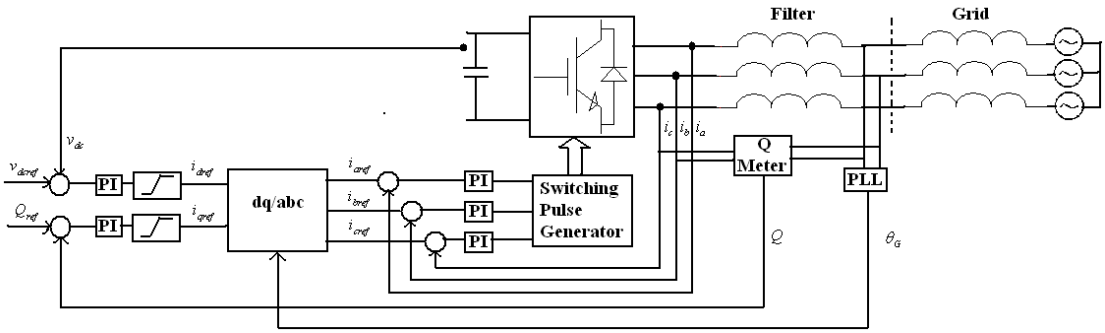

Fig. 5.0. General grid side converter control [168].

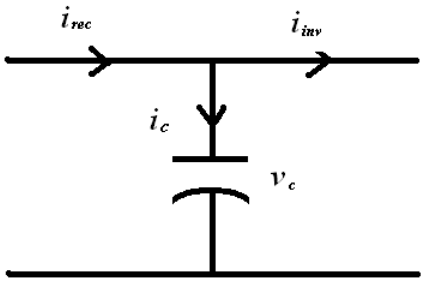

Fig. 5.1. DC link capacitor voltage and currents.

The parameters of the DC link capacitor are shown in Fig. 5.1. The equation for the current can be derived from:

$$i_c = c\frac{dv_c}{dt} = i_{rec} - i_{inv} = \frac{P_t}{v_c} - \frac{P_g}{v_c} \tag{5.5}$$

where P_t is the turbine power or DC link input power, P_g is the grid power, v_c is the capacitor voltage, i_{inv} is the inverter side current, i_{rec} is the rectifier side current, c the capacitor value and i_c the capacitor current. From the equations, it can be deduced that the DC voltage can be adjusted by controlling P_g or i_{qo}. The control loop is shown in Fig. 5.2. The difference between the reference capacitor voltage and the actual capacitor voltage determines the value of i_{qo} that is required to keep the DC voltage constant [180]-[182].

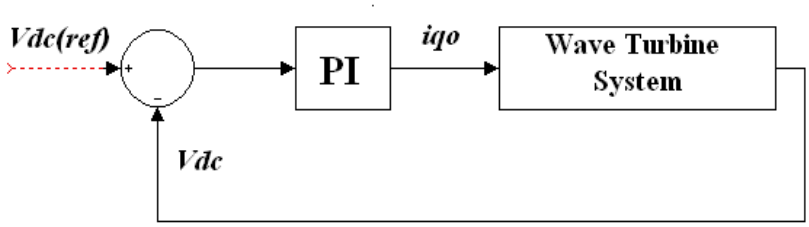

Fig. 5.2. DC link voltage control.

The second control involved is the reactive power control technique [183-185]. Equation (5.4) clearly shows that i_{do} should be varied to control the reactive power. Fig. 5.3 represents the control of the reactive power. The difference between the reference reactive power and the actual reactive power determines i_{do}.

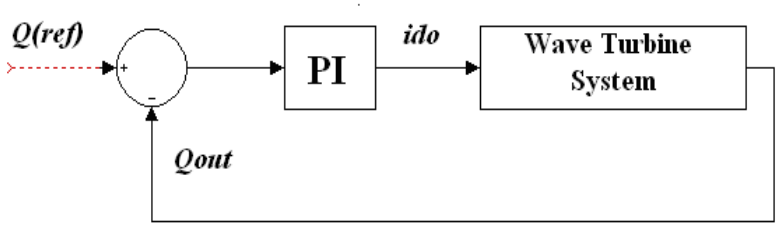

Fig. 5.3. Reactive power control loop.

The third control involved is the control of the bus voltage [186][187]. A similar technique as for the reactive power is used. By adjusting i_{do}, the voltage drop can be controlled and as a result, the bus voltage will be controlled. Fig. 5.4 shows the control loop for the bus voltage control.

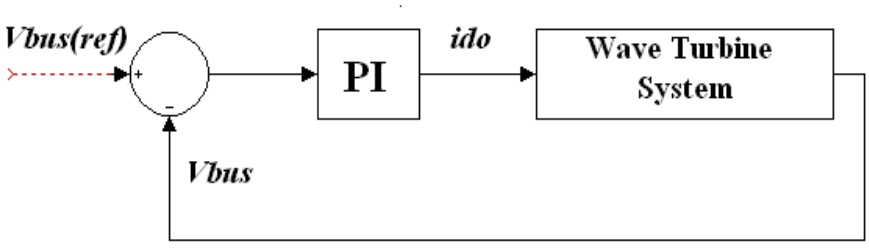

Fig. 5.4. Bus voltage control loop.

5.3.1 Modelling and Simulations

The control process shown in Fig. 5.5 is started by detecting the phase angle from the grid voltages using a Phase Locked Loop (PLL) device. It provides the inverter with the frequency and phase angle. By doing this, the inverter current angle will be synchronized with the grid voltage angle to keep the power factor as close as possible to 1. In PLL, a Park Transform is used to transform the parameters in the *abc* frame to the *d-q* reference frame. A PI is then used to reduce the difference between the grid phase angle, γ and inverter phase angle, θ using

$$\gamma - \theta \cong \sin(\gamma - \theta) = \Delta\theta \tag{5.6}$$

The frequency of the grid is set at 50 Hz. The PI algorithm is used in various locations in the simulation and this computes and transmits a signal that needs to be controlled. The output signals from the PIs depends on several parameters such as the proportional gain, integral time and error as mentioned in previous chapter. The DC link voltage control and the reactive power control loop are implemented in this simulation. Outputs from the PI controllers, which are in the *d-q* reference frame, are transformed back to the *abc* reference frame. The signals will then serve as the input for the SVM (space vector modulator), where the gate control signals will be generated. A simple L-filter is used in this simulation to connect the grid side inverter to an infinite bus.

The results of the simulation are shown in Fig. 5.6 when $V_{dc(ref)}$ is set at 150 V. The grid line-to-line rms voltage is 120 V, and the input for the DC link is from the generator shown in previous chapter for turbine with a stator resistance value of 4.1 Ohm. The PWM carrier frequency is 10 kHz and the DC link capacitor value is 1 μF.

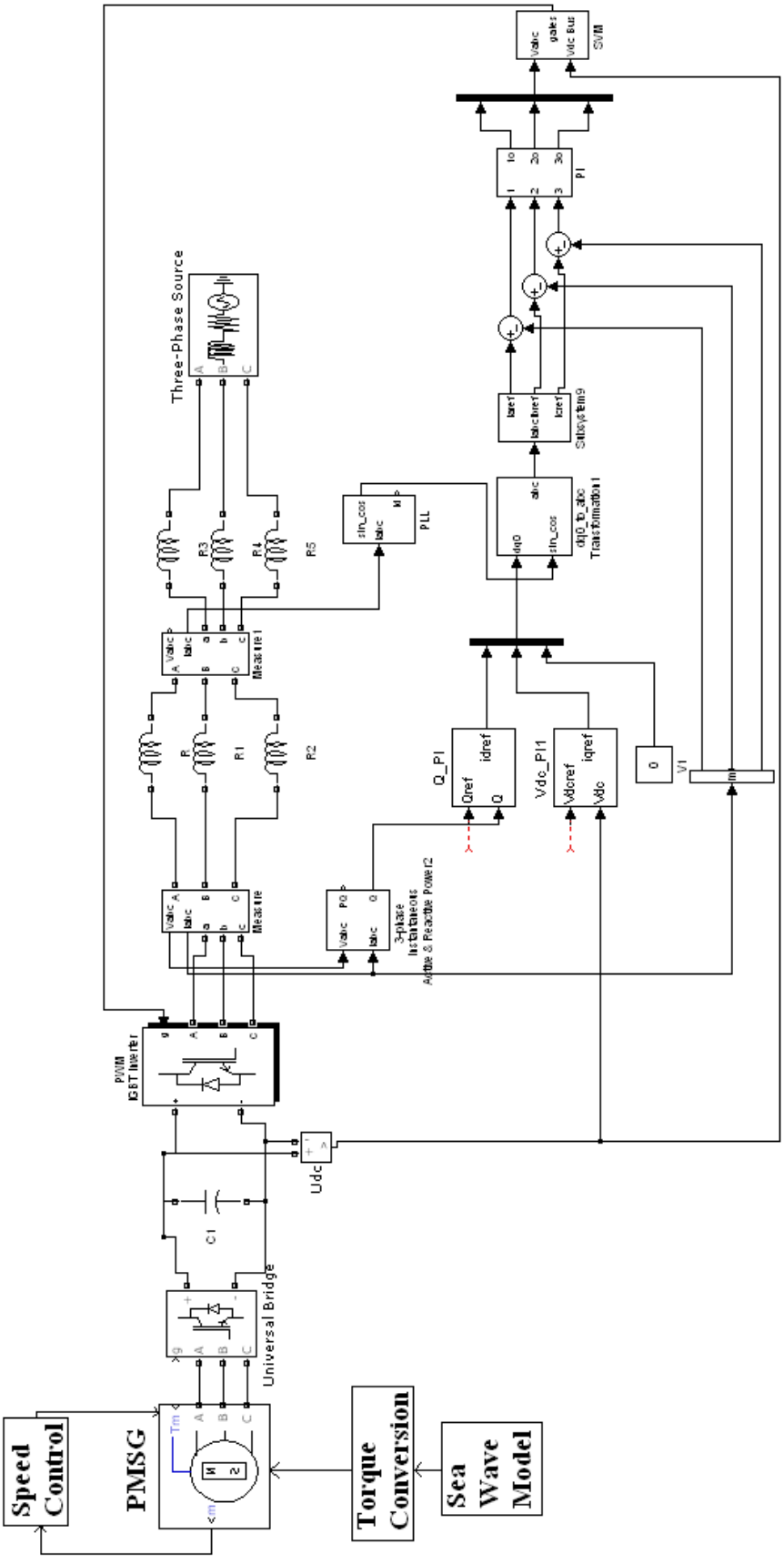

Fig. 5.5. Grid side converter control implemented using MATLAB/Simulink.

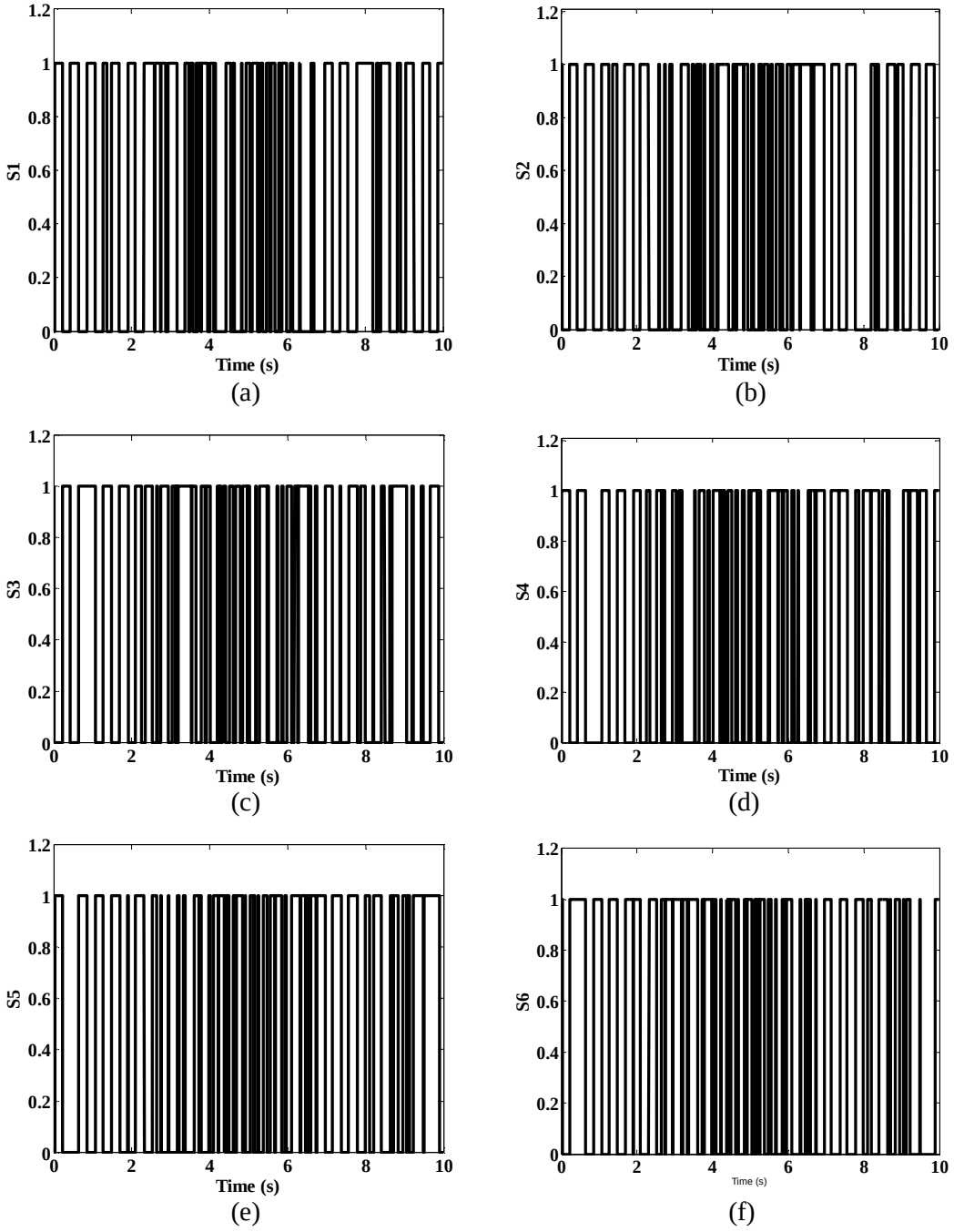

Fig. 5.6. (a)-(f) PWM gating signal generated for all 6 IGBTs.

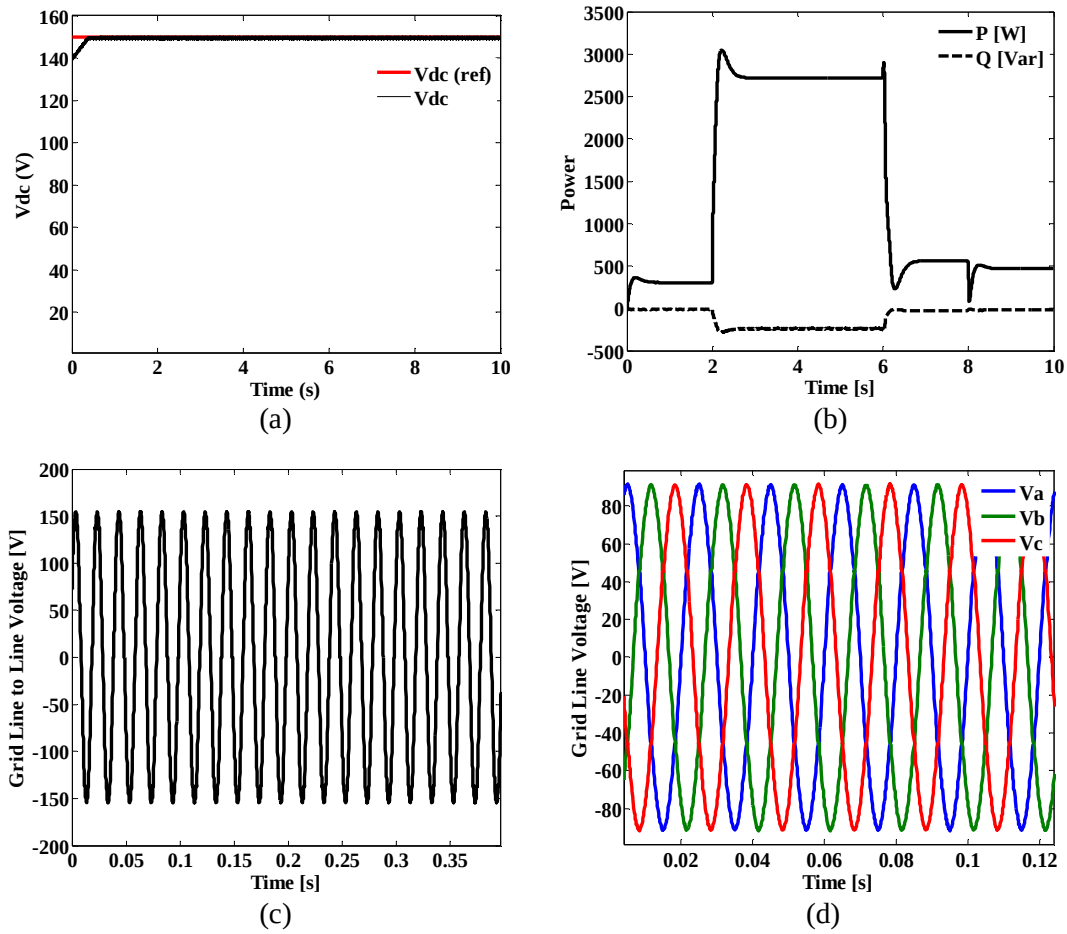

Fig 5.7. (a) DC link voltage; (b) The active power and reactive power of grid side inverter; (c) Grid Line to Line voltage; and (d) Grid line voltage.

Fig. 5.6 shows all the six gate signals for the IGBTs of the inverter. These are the pulses that are generated by using the control methods described above. Fig 5.7 shows the simulation results of the control method with the wave converter system operating under normal conditions. The goal of the simulation is to transfer the maximum power to the grid.

Fig. 5.7(a) shows that the DC link voltage can be traced accurately with minimal fluctuation at the rated voltage of 150V with a rise time of approximately 1.2 s. In the DC link circuit, the voltage is limited to ±10% to prevent over voltages and to protect the IGBTs of the inverters. The controllable region can be adjusted according to the power converter behaviour.

In Fig. 5.7(b), the active power and reactive power requirements for the inverter are shown. As a result of some losses, the transferred active power is slightly reduced compared to the power generated by the PMSG. Demand of the reactive power actually depends of the active power transferred. When active power increases, reactive power increases too. The negative sign of the reactive power indicated that it is in generating mode. The active powers obtained are 300 W, 2700 W, 550 W and 450 W respectively for all 4 cycles while the reactive powers obtained are -12 VAR, -240 VAR, -31 VAR and -20 VAR respectively.

From Figs. 5.7(c) and (d), it can be seen that the grid side voltage is kept at a rated value where the line-to-line voltage is 150 V and the line voltage stays at 90 V.

Overall, the objectives of the control method are achieved. These ensure that maximum power is transferred to the grid with minimal disturbance.

Chapter 6

CONCLUSIONS

6.1 General

In this project, mathematical modelling, analysis, control system design, simulation of generator using the FEMM and PC-BDC, simulation of armature control, generator speed control and grid side converter control using MATLAB/Simulink have been carried out in order to design and simulate a Bristol cylinder weave energy device. Wave properties were studied using Linear Small Wave Amplitude Theory and Stokes Second Order Wave Theory. The design of the generator have been performed analytically and also by using the finite element analysis method. Analysis and control system design for armature control, generator speed control, and grid side converter control were carried out and tuned using MATLAB/Simulink.

The research has shown that with intensive control, the Bristol cylinder rotating wave device is well suited to the task of converting wave energy into useful electrical power. The motivation driving this research has been the increasing interest in renewable energy device development, especially wave devices, which is very rare. The aims are to effectively convert wave power and distribute it to the grid. Wave devices, especially the rotating type, are a relatively new development in renewable energy field. However, they have potential to tap into the existing power supply market in the future.

The studies carried out provide an understanding of the problems involved in the whole process from generating to transmitting. It can be treated as a feasibility study of the device. The analysis and control of a Bristol cylinder wave conversion system was successfully simulated.

The research work has shown that a surface PMSG is a possible solution for the Bristol cylinder as it can be designed with a high pole number for low speed

operation and it has relatively high permanent magnet flux linkage. The flux linkage is limited by the permanent magnet characteristic, air gap, pole number and the sizing of the generator. The problem is always to maximise the pole number, at the same time minimizing the air gap within a given generator size. These are the main issues found in all the low speed generators.

For the generator, power conversion is maximised when the rotation of the Bristol cylinder is synchronised with the speed of prevailing incoming wave. In fact it is a synchronous speed so torque will not be generated at any other speed. This is proved achievable by studying the effect of the armature length corresponding to the incident wave and the speed control. The armature length of the cylinder arms or the rotational radius can be adjusted according to the incident wave while the generator speed control will control the Bristol cylinder rotational speed. The indirect FOC is simulated and it shows good control of the generator speed. The main difficulties will be on how to obtain very accurate measurement of the parameters of the incident wave.

Lastly, the control for the grid side converter was simulated successfully where the main goals is to keep the DC link voltage constant. This is needed so that full active power transfer can be achieved. The control system included a DC link voltage control loop, a reactive power control loop and a bus voltage control loop.

6.2 Suggestions for Further Research

This research work has contributed new findings to generator design and control strategies for rotating wave devices, particularly the Bristol cylinder wave device. It shows that the implementation of the device is feasible. The impact of the control has been assessed using MATLAB/Simulink. Contributions have been made to the design of a lab scale wave tank, the design of a generator specifically for the Bristol cylinder application, and the control strategies that must be implemented to maximise the output power of both the PMSG and the power transmitted to the grid. It is suggested that further research should be undertaken to improve the findings of the present research work as mentioned below:

- A lab scale wave tank can be constructed to test and verified the actual movement of the cylinder in the presence of incoming waves. Actual torque values absorbed must be measured to know exactly the interaction between the cylinder and waves.
- Other than the surface PMSG, PMSGs with other topologies can be designed to provide comparison and to get the best out of the Bristol cylinder. Research on the material for the Bristol cylinder can be considered too, as this area is still limited.
- Research on the wave detection is also required. It is very difficult to obtain accurate data of waves and to predict the time the wave will reach the cylinder. With the improvements in intelligent sensor technology, this is possible. Input of the wave data is very important and critical for this device and it affects the overall performance of the system.
- A single machine was studied in this project; however, research can be done on the effects of using multiple machines at one time. In reality, the Bristol cylinder may not be deployed on a site individually, but in lines or rows. So it is worth addressing the integration of multiple machines on to the grid network.
- For power distribution and transmission network integration, research can be done on the quality of the power supplied. For this research, the main aim is to maximize the transmission from the generator to the grid. The power quality may represent a good opportunity to further the research and improving the transmission of power, particularly since the power is pulsing.

References

[1] Energy Information Administration (EIA). *International Energy Outlook 2010*, 2010.

[2] D. Dunnett and J. S. Wallace, "Electricity generation from wave power in Canada, "*Renewable Energy*, Vol. 34, Issue 1, Jan 2009, pp 179-195.

[3] D. Elwood, S. C. Yim, J. Prudell, C. Stillinger, A. von Jouanne, T. Brekken, A. Brown and R. Paasch, "Design, construction, and ocean testing of a taut-moored dual-body wave energy converter with a linear generator power take-off", *Renewable Energy*, Vol. 35, Issue 2, Feb 2010, pp 348-354.

[4] S. J. Beatty, P. Wild and B. J. Buckham, "Integration of a wave energy converter into the electricity supply of a remote Alaskan island", *Renewable Energy*, Vol. 35, No. 6, June 2010, pp 1203-1213.

[5] S. Boronowski, P. Wild, A. Rowe and G. Cornelis van Kooten, "Integration of wave power in Haida Gwaii", *Renewable Energy*, Vol. 35, No. 11, Nov. 2010, pp 2415-2421.

[6] World Energy Council (WEC), *2010 Survey of Energy Resources*, 2010.

[7] G. Iglesias, M. López, R. Carballo, A. Castro, J.A. Fraguela and P. Frigaard, "Wave energy potential in Galicia (NW Spain)", *Renewable Energy*, Vol. 34, Issue 11, Nov 2009, pp 2323-2333.

[8] Z. Defne, K. A. Haas and H. M. Fritz, "Wave power potential along the Atlantic coast of the southeastern USA", *Renewable Energy*, Vol. 34, Issue 10, Oct 2009, pp 2197-2205.

[9] E. Rusu and C. Guedes Soares, "Numerical modelling to estimate the spatial distribution of the wave energy in the Portuguese nearshore", *Renewable Energy*, Vol. 34, Issue 6, June 2009, pp 1501-1516.

[10] A. Palha, L. Mendes, C. Juana Fortes, A. Brito-Melo and A. Sarmento, "The impact of wave energy farms in the shoreline wave climate: Portuguese pilot zone case study using Pelamis energy wave devices", *Renewable Energy*, Vol. 35, Issue 1, Jan 2010, pp 62-77.

[11] J. E. Stopa, K. F. Cheung and Y.-L. Chen, "Assessment of wave energy resources in Hawaii", *Renewable Energy*, Vol, 36, No. 2, Feb 2011, pp 554-567.

[12] M. Abbaspour and R. Rahimi, "Iran atlas of offshore renewable energies", *Renewable Energy*, Vol. 36, No. 1, Jan. 2011, pp 388-398.

[13] G. Iglesias and R. Carballo, "Wave energy and nearshore hot spots: The case of the SE Bay of Biscay", *Renewable Energy*, Vol. 35, No. 11, Nov. 2010, pp 2490-2500.

[14] A. Palha, L. Mendes, C. Juana Fortes, A. Brito-Melo and A. Sarmento, "The impact of wave energy farms in the shoreline wave climate: Portuguese pilot zone case study using Pelamis energy wave devices", *Renewable Energy*, Vol. 35, No. 1, Jan. 2010, pp 62-77.

[15] D. V. Evans, D. C. Jeffrey, S. H. Salter and J. R. M. Taylor, "Submerged cylinder wave energy device: theory and experiment", *Applied Ocean Research*, Vol. 1, pp. 3-12, 1979.

[16] D. G. Dorrell, M. F. Hsieh and C. C. Lin, "A Multichamber Oscillating Water Column Using Cascaded Savonius Turbines", *IEEE Transactions of Industry Applications,* Vol. 46, No. 6, pp. 2372-2380, 2010.

[17] D. G. Dorrell, M. F. Hsieh and C. C. Lin, "A Small Segmented Oscillating Water Column Using a Savonius Rotor Turbine", *IEEE Transactions on Industry Applications*, Vol. 46, No. 5, pp. 2080-2088, 2010.

[18] M. N. Gomes, L. A. O. Rocha, L. A. Isoldl, C. R. Olinto and J. A. Souza, "Computational Modeling of an Oscillating Water Column Device for the Rio

Grande Coast", *Proc. of 2009 Third Southern Conference on Computational Modeling (MCSUL)*, pp. 107-112, 2009.

[19] R. V. Chaplin and G. A. Aggidis, "An Investigation into Power from Pitch-Surge Point-Absorber Wave Energy Converters", *Proc. International Conference on Clean Electrical Power*, 2007 (ICCEP '07), pp. 520-525, 2007.

[20] G. De Backer, M. Vantorre, C. Beels, J. De Rouck and P. Frigaard, "Power Absorption by Closely Spaced Point Absorbers in Constrained Conditions", *IET Renewable Power Generation*, Vol.4, No. 6, pp. 579-591.

[21] K. Rhinefrank, J. Prudell and A. Schacher, "Development and Characterization of a Novel Direct Drive Rotary Wave Energy Absorber", *Proc. of MTS/IEEE Biloxi-Marine Technology for Our Future: Global and Local Challenges (OCEANS 2009)*, pp. 1-5, 2009.

[22] I. G. Bryden, "Marine Renewable Energy in the United Kingdom and the Role of the University of Edinburgh", *Proc. of 2010 IEEE Power and Energy Society General Meeting*, pp. 1-5, 2010.

[23] M. C. Haller and P. A. Catalan, "Remote Sensing of Wave Roller Lengths in the Laboratory", *Journal of Geophysical Research*, Vol. 114, C07022, 2009.

[24] J. Khan and G. S. Buyan. *Ocean Energy: Global Technology Development Status*. Powertech Labs, 2009.

[25] W. D. Jones, (2008), *Ocean Power Catches a Wave* [Online]. Available: http://spectrum.ieee.org/energy/renewables/ocean-power-catches-a-wave

[26] I. Bulatov, S. J. Perry and J. J. Klemes, "A New Emerging Energy Technology-Pelamis-Demonstration of the Assessment by EMINENT Tool", *12th International Conference on Process Integration, Modelling and Optimisation for Energy Saving and Pollution Reduction (PRES '09)*, Rome, Italy, 12-13 May 2009.

[27] S. D. Weller, T. J. Stallard and P. K. Stansby, "Experimental Measurements of Irregular Wave Interaction Factors in Closely Spaced Arrays", *IET Renewable Power Generation*, Vol. 4, No. 6, pp. 628-637, 2010.

[28] S. L. P. Iahnke, M.N. Gomes, L. A. Isoldi and L. A. O. Rocha, "Energy from the Sea: Computational Modeling of an Overtopping Device", *Proc. of 2009 Third Southern Conference on Computational Modeling (MCSUL)*, pp. 94-95, 2009.

[29] B. W. Nam, S. H. Shin, K. Y. Hong and S. W. Hong, "Numerical Simulation of Wave Flow over the Spiral-Reef Overtopping Device", *Proc. of 2010 XIX International Conference on Electrical Machines (ICEM)*, pp. 1-7, 2010.

[30] D. L. O'Sullivan and A. W. Lewis, "Generator Requirements and Functionality for Ocean Energy Converters", *Proc. of Eighth (2008) ISOPE Pacific/Asia Offshore Mechanics Symposium*, pp. 262-267, 2008.

[31] P. McIver and M. McIver, "Wave-Power Absorption by a Line of Submerged Horizontal Cylinders", *Applied Ocean Research*, Vol. 17, No. 2, pp. 117-126, 1995.

[32] M. A. Mueller, "Electrical generators for direct drive wave energy converters", *IEE Proc on Generation, Transmission and Distribution*, Vol. 149, Iss. 4, pp. 446-456, 2002.

[33] G. S. Bhuyan, "World-wide Status for Harnessing Ocean Renewable Resources", *2010 IEEE Power and Energy Society General Meeting*, pp. 1-3, 2010.

[34] T. Ahmed, K. Nishida and M. Nakaoka, "Grid Power Integration Technologies for Offshore Ocean Wave Energy", *Proc. of 2010 IEEE Energy Conversion Congress and Exposition (ECCE)*, pp. 2378-2385, 2010.

[35] The Queen's University of Belfast, *Islay LIMPET Wave Power Plant, Publishable Report*, The European Commission, Framework of the Non Nuclear Energy Programme JOULE III, Contract JOR3-CT98-0312, 2002.

[36] M. Singh, V. Khadkikar, A. Chandra and V. K. Varma, "Grid Interconnection of Renewable Energy Sources at the Distribution Level With Power-Quality Improvement Features", *IEEE Trans. On Power Delivery*, Vol. 26, No. 1, Jan. 2011, pp 307 – 315.

[37] X. Liang and W. M. Jackson, "Influence of Subsea Cables on Offshore Power Distribution Systems", IEEE Trans. On Industry Applications, Vol. 45, Iss. 6, pp 2136 – 2144, 2009.

[38] G. P. Harrison and A. R. Wallace, "Sensitivity of Wave Energy to Climate Change", *IEEE Transaction on Energy Conversion*, Vol. 20, No. 4, pp. 870-877, 2005.

[39] L. Rodrigues, "Wave Power Conversion Systems for Electrical Energy Production", *International Conference on Renewable Energies and Power Quality (ICREPQ'08),* Santander, Spain, 12-14 March 2008.

[40] S. Patricio, A. Moura, and T. Simas, "Wave energy and underwater noise: State of art and uncertainties", *OCEANS 2009-Europe,* Bremen, 11-14 May 2009, pp. 1-5.

[41] J. R. Halliday, *An investigation into the applicability of the Fourier transform to dispersive water waves & their short term prediction*, PhD Thesis, University of Glasgow, January 2007.

[42] R. M. Sorensen, *Basic Wave Mechanics: For Coastal and Ocean Engineers*, John Wiley & Sons, Chapter 2, 1993.

[43] J. Cruz, *Ocean Wave Energy: Current Status and Future Perspectives (Green Energy and Technology)*, Springer-Verlag Berlin Heidelberg, pp. 147-159, 2008.

[44] M. Faizal, M. R. Ahmed and Y. H. Lee, "On Utilizing the Orbital Motion in Water Waves to Drive a Savonius Rotor", *Renewable Energy*, Vol. 35, No. 1, pp. 164-169, 2010.

[45] T. Garrison, *Oceanography: An Invitation to Marine Science*, Thomson Brooks/Cole, 6th Edition, Chapter 10, 2007.

[46] B. B. Sharp, M. H. A. Khader and H. Ullah, "Wave Induced Water Particle Motion", *Eigth Australasian Fluid Mechanics Conference*, pp. 6A.5-6A.9, 1983.

[47] T. Garrison, *Essentials of Oceanography*, 5th Edition, Brooks/Cole Cengage Learning, 2009.

[48] R. W. Johnson, *The Handbook of Fluid Dynamics*, CRC Press L.L.C and Springer-Verlag GmbH & Co, Chapter 12, 1998.

[49] D. G. Dorrell, J. R. Halliday, S. MacLean, P. Miller and F. Santamaria Mosquera, "Development of Small-Scale Facilities for Initiating Studies into Sea Wave Energy generation", *International Conference on Renewable Energy and power Quality*, Zaragoza, Spain, March 2005.

[50] D. G. Dorrell, "Permanent magnet generators for renewable energy devices with wide speed range and pulsating power delivery", *International Journal of Conputer Applications in Technology*, vol. 35, no. 2, pp. 77-82, 2009.

[51] A. Muetze and J. G. Vining, "Ocean Wave Energy Conversion - A Survey", *Proc. of 41st IAS Annual Industry Applications Conference 2006*, Vol. 3, pp. 1410-1417, 2006.

[52] D. V. Evans, "Power from Water Waves", *Annual Review of Fluid Mechanics*, Vol. 13, pp. 157-187, 1981.

[53] R. Shaw, *Wave Energy: A Design Challenge*, Ellis Horwood Publishers, 1982.

[54] R. L. Wiegel and J. W. Johnson,"Elements of Wave Theory", *Proc. of the International Conference on Coastal Engineering, No. 1, (1950)*, pp. 5-21, 1950.

[55] D. Henry, "On Gerstner's Water Wave", *Journal of Nonlinear Mathematical Physics*, Vol. 15, pp. 87-95, 2008.

[56] E. Wahlen, "On Rotational Water Waves with Surface Tension", *Philisophical Trans. Of The Royal Society A*, Vol. 365, No. 1858, pp. 2215-2225, 2007.

[57] A. Constantin and W. Strauss, "Rotational Steady Water Waves Near Stagnation", *Philisophical Trans. Of The Royal Society A*, Vol. 365, No. 1858, pp. 2227-2239, 2007.

[58] J. P Le Roux, "Profiles of Fully Developed (Airy) Waves in Different Water Depths", *Coastal Engineering*, Vol. 55, No. 9, pp. 701-703, 2008

[59] R. M. Sorensen, *Basic Coastal Engineering*, 3rd Edition, Springer Science + Business Media Inc., 2006

[60] A. D. D. Craik, "The Origins of Water Wave Theory", *Annual Review of Fluid Mechanics*, Vol. 36, pp.1-28, 2004.

[61] D. P. Horn and J. Hardisty, "The Application of Stokes' Wave Theory Under Changing Sea Levels in the Irish Sea", *Marine Geology*, Vol. 94, pp. 341-351, 1990.

[62] J. F. Wilson, B. J. Muga and L. C. Reese, *Dynamics of Offshore Structures*, John Wiley & Sons, pp. 61-83, 2003.

[63] T. V. Heath, "The Development of a Turbo-Generation System for Application in OWC Breakwaters", *Proc. of the 7th European Wave and Tidal Energy Conference*, 2007.

[64] Antonio F. de O. Falcao, "Wave Energy Utilization: A Review of the Technologies", *Renewable & Sustainable Energy Reviews*, Vol. 14., No. 3, 2010.

[65] Antonio F. de O. Falcao, "First Generation Wave Power Plants: Current Status and R&D Requirements", *Journal of Offshore Mechanics and Arctic Engineering*, Vol. 126., No. 4, pp. 384-388, 2004.

[66] D. O'Sullivan, J. Griffiths, M. G. Egan and A. W. Lewis, "Development of an Electrical Power Take Off System for a Sea-test Scaled Offshore Wave Energy Device", *Renewable Energy*, Vol. 36., No. 4, pp. 1236-1244, 2011.

[67] P. A. Mikladal, *Sustainable Energy in the Faroe Islands-The Role of Hydropower*, Burdardygg El Orka, Chapter 2, 2005.

[68] K. Rhinefrank, E. B. Agamloh, A.von Jouanne, A. K. Wallace, J. Prudell, K. Kimble, J. Aills, E. Schmidt, P. Chan, B. Sweeny and A. Schacher, "Novel Ocean Energy Permanent Magnet Linear Generator Buoy", *Renewable Energy*, Vol. 31., No. 9, pp. 1279-1298, 2006.

[69] M. G. Hughes and A. D. Heap, "National-scale Wave Energy Resource Assessment for Australia", *Renewable Energy*, Vol. 35., No. 8, pp. 1783-1791, 2010.

[70] C. Bostrom, O. Svensson, M. Rahm, E. Lejerskog, A. Savin, E. Stromstedt, J. Engstrom, H. Gravrakmo, K. Haikonen, R. Waters, D. Bjorklof, T. Johansson, J. Sundberg and M. Leijon, "Design Proposal of Electrical System for Linear Generator Wave Power Plants", *Proc. of 35th Annual Conference of IEEE Industrial Electronics (IECON '09)*, pp. 4393-4398, 2009.

[71] M. S. Lagoun, A Benbouzid and M. E. H. Benbouzid, "Ocean Wave Converters: State of the Art and Current Status", *Proc. of 2010 IEEE International Energy Conference and Exhibition (EnergyCon)*, pp. 636-641, 2010.

[72] M. Folley, T. W. T. Whittaker and J. van't Hoff, "The Design of Small Seabed-Mounted Bottom-Hinged Wave Energy Converters", *Proc. of the 7th European Wave and Tidal Energy Conference*, pp. 636-641, 2007.

[73] W. D. Jones, *Update-Ocean Power Catches a Wave*, IEEE Spectrum, Vol. 45, No. 7, pp. 14, 2008.

[74] *Managing the Ups and Downs of Energy Generation for Wave Star*, Rockwell Automation Inc., 2010.

[75] V. Heller, J. R. Chaplin, F. J. M. Farley, M. R. Hann and G. E. Hearn, "Physical Model Tests of the Anaconda Wave Energy", *Proc. of the European IAHR Congress 2010,* 2010.

[76] J. P. Kofoed and E. Osaland, "Crest Level Optimization of the Multi Level Overtopping Based Wave Energy Converter Seawave Slot-Cone Generator", *Proc. of 6th European Wave and Tidal Energy Conference,* pp. 243-250, 2005.

[77] N. J. Baker and M. A. Mueller, "Direct Drive Wave Energy Converters", *Proc. of Universities Power Engineering Conference (UPEC),* pp. 1-7, 2001.

[78] P. Boccotti, *Wave mechanics for ocean engineering*, Elsevier Oceanography Series, Amsterdam, 2000.

[79] G. Payne, *Guidance for the experimental tank testing of wave energy converters*, SuperGen Marine, University of Edinburgh, 2008 (available at www.supergen-marine.org.uk)

[80] M. J. Meyers, *Flow Regime Prediction via Froude Number Calculation in a Rock-Bedded Stream, Master Thesis*, Brock University, March 2010.

[81] K. K. McCreight, *A Note on the Selection of Wave Spectra for Design Evaluation*, Research and Development Report, Naval Surface Warfare Center, Bethesda, Maryland 20814, CRDKNSWC-HD-974-02, January 1998

[82] Industrial Technology Research Institute, *Development of analysis techniques of Sea Area of Potential Areas of Energy and Evaluation Utilization*, Technical Report of Bureau of Energy, Ministry of Economic Affairs, Taiwan, 2006.

[83] D. G. Dorrell, M.-F. Hsieh, M. Popescu, L. Evans, D. A Staton and V. Grout, "A Review of the Design Issues and Techniques for Radial-Flux Brushless Surface and Internal Rare-Earth Permanent Magnet Motors", *IEEE Transactions on Industrial Electronics*, Vol. 58, No. 9, Sept. 2011, pp 3741 - 3757.

[84] D. G. Dorrell, A. M. Knight, L. Evans and M. Popescu, "Analysis and Design Techniques Applied to Hybrid Vehicle Drive Machines – Assessment of Alternative IPM and Induction Motor Topologies", *IEEE Transactions on Industrial Electronics*, 2011/2012 (available in Xplore Early Access).

[50] D. G. Dorrell, "Permanent Magnet Generators for Renewable Energy Devices with Wide Speed Range and Pulsating Power Delivery", *International Journal of Computer Applications in Technology (IJCAT)*, Vol. 36, No. 2, 2009.

[85] J. Cao and X. Yang, "Design and Magnetic Field Analysis of a Dual-rotor Permanent-magnet Synchronous Wind Generator", *Proc. of International Conference on Electrical Machines and Systems (ICEMS 2008)*, pp. 3202-3205, 2008.

[86] Y.-M. You, K.-Y. Hwang and B.-i. Kwon, "Optimal Design of Distributed Winding Axial Flux Permanent Magnet Synchronous Generator for Wind Turbine Systems", *Proc. Of 2010 14th Biennial IEEE Conference on Electromagnetic Field Computation (CEFC)*, pp. 1, 2010.

[87] M. E. Topal and L. T. Ergene, "Designing a Wind Turbine with Permanent Magnet Synchronous Generator", *Proc. of 2010 National Conference on Electrical, Electronics and Computer Engineering (ELECO)*, pp 325-329, 2010.

[88] Z. Zhou, W. Knapp, J. MacEnri, H. C. Sorensen, E. F. Madsen, I. Masters and P. Igic, "Permanent Magnet Generator Control and Electrical System Configuration for Wave Dragon MW Wave Energy Take-off System", *Proc. of IEEE International Symposium on Industrial Electronics (ISIE 2008)*, pp, 1580-1585, 2008.

[89] K. Yuen, K. Thomas, M. Grabbe, P. Deglaire, M. Bouquerel, D. Osterberg and M. Leijon, "Matching a Permanent Magnet Synchronous Generator to a Fixed Pitch Vertical Axis Turbine for Marine Current Energy Conversion", *IEEE Journal of Oceanic Engineering*, Vol. 34, No. 1, pp. 24-31, 2009.

[90] A. Shibaike, M. Sanada and S. Morimoto, "Suitable Configuration of Permanenent Magnet Linear Synchronous Generator for Wave Power Generation", *Proc. of Power Conversion Conference-Nagoya 2007 (PCC '07*), pp. 210-215, 2007.

[91] X. Cui, A. Binder and E. Schlemmer, "Straight-Flow Permanent Magnet Synchronous Generator Design for Small Hydro Power Plants", *Proc. of International Conference on Clean Electrical Power*, pp. 323-328, 2007.

[92] P. K. Goel, B. Singh, S. S. Murthy and N. Kishore, "Autonomous Hybrid System Using PMSGs for Hydro and Wind Power Generation", *Proc. of 35th Annual Conference of IEEE Industrial Electronics (IECON '09),* pp. 255-260, 2005.

[93] A. Binder and T. Schneider, "Permanent Magnet Synchronous Generators for Regenerative Energy Conversion", *Proc. of 2005 European Conference on Power Electronics and Applications*, pp. 1-10, 2005

[94] J. F. Gieras and M. Wing, *Permanent Magnet Motor Technology*, 2nd ed, Marcel Dekker, Inc, 2002.

[95] J. R Hendershot and T. J. E. Miller, *Design of Brushless Permanent Magnet Motors*, Magna Physics Pub, Oxford , Clarendon Press, 1994.

[96] S. P. Thompson, *Dynamo Electric Machinery, Vol. II, Alternating Current Machinery*, E &FN Spon, London, 1905.

[97] M. Walker, *Specification and Design of Dynamo-Electric Machinery*, Longmans, Green and Co., London, 1920.

[98] M. Walker, *The Diagnosis of Troubles in Electrical Machines*, Longmans, Green and Co., London, 1921.

[99] C. Concordia, *Synchronous Machines*, USA John Wiley & Sons, 1950.

[100] B. Adkins, *The General Theory of Electrical Machines*, UK, Chapman and Hall, 1964.

[101] A. E. Fitzgerald and C. Kingsley, *Electric Machinery*, USA, McGraw-Hill, 1961.

[102] S. J. Chapman, *Electric Machinery Fundamentals*, USA, McGraw-Hill, 1998.

[103] E. W. Kimbark, *Power System Stability I, II, III*, USA, IEEE Press, 1995.

[104] P. C. Krause, *Analysis of Electric Machinery*, Singapore, McGraw-Hill, 1987.

[105] D. O'Kelly and S. Simmons, *Introduction to Generalised Electrical Machine Theory*, UK, McGraw-Hill, 1968.

[106] P. C. Sen, *Principles of Electric Machines and Power Electronics*, USA, John Wiley & Sons, 1997.

[107] F. Caricchi, F. Crescimbini and O. Honrati, "Modular axial-flux permanent-magnet motor for ship propulsion drives", IEEE Trans. On Energy Conversion, Vol 14., Iss. 3, Sept. 1999, pp 637 – 679.

[108] J. Vaidya and E. Gregory, "Advanced Electric Generator & Control for High Speed Micro/Mini Turbine Based Power Systems", *Proc. of Power Gen International Conference*, pp. 1-13, 2002.

[109] B. Andreas and S. Tobias, "Permanent Magnet Synchronous Generators for Regenerative Energy Conversion – A Survey", *Proc.of 11th European Conference on Power Electronics and Applications (EPE 2005),* 2005

[110] F. Wang, J. Bai, Q. Hou and J. Pan, "Design Features of Low Speed Permanent Magnet Generator Direct Driven by Wind Turbine", *Proc. of 8th*

International Conference on Electrical Machines and Systems, Vol. 2, pp. 1017-1020, 2005.

[111] R. Chedid, F. Chaaban, M. Yehia and L. L Freris, "A Novel Permanent Magnet Low Speed Generator", Proc. of 6th International Conference on Electrical Machines and Drives, pp. 443-447, 1993.

[112] A. S. McDonald, M. A. Mueller and H. Polinder, "Structural Mass in Direct-drive Permanent Magnet Electrical Generators", IET Renewable Power Generation, Vol. 2, No. 1, pp. 3-15, 2008.

[113] A. Ragheb and M. Ragheb, "Wind Turbine Gearbox Technologies", *Proc. of the 1st International Nuclear and Renewable Energy Conference (INREC10*), pp. INREC10-1-INREC10-8, 2010.

[114] H. Polinder, F. F. A. van der Pijl, G. J. de Vilder and P. J. Tavner, "Comparison of Direct-Drive and Geared Generator Concepts for Wind Turbines", *IEEE Transactions on Energy Conversion*, Vol. 21, No. 3, pp. 725-733, 2006

[115] S. Joeckel, *Calculation of Different Generator Systems for Wind Turbines with Paricular Reference to Low-Speed Permanent-Magnet Machines*, Ph.D. Thesis, Darmstadt Univ. of Technology, Shaker, Aachen.

[116] M. Kimura, H. Koharagi, K. Imaie, S. Dodo, H. Arita and K. Tsubouchi, "A Permanent Magnet Synchronous Generator with Variable Speed Input for CO-generation System", *IEEE Power Engineering Society Winter Meeting*, Vol. 3, pp. 1419-1424, 2001.

[117] A. O. Di Tommaso, R. Miceli, G. R. Galluzo and M. Traoanese, "Optimum Performance of Permanent Magnet Synchronous Generators Coupled to Wind Turbines", *IEEE Power Engineering Society General Meeting*, pp. 1-7, 2007.

[118] T. D. Batzel and K. L. Lee, "Slotless Permanent Magnet Synchronous Motor Operation without a High Resolution Rotor Angle Sensor", *IEEE Transaction on Energy Conversion*, Vol. 15, No. 4, 2000.

[119] J. Ormerod, "Permanent Magnet", *IEE Colloquium on New Permanent Magnet Materials and Their Applications*, pp. 1/1-1/5, 1989.

[120] E. Schloemann, "*Fluctuations of the Magnetic Field Generated by Permanent Magnets*", Journal of Applied Physics, Vol. 55, No. 6, pp. 2470-2472, 1984.

[121] M. A. Rahman and A. M. Osheiba, "Performance of Large Line-Start Permanent Magnet Synchronous Motors", *IEEE Trans. On Energy Conversion*, Vol. 5, No. 1, pp. 211-217, 1990.

[122] B. W. Williams, *Power Electronics:Devices, Drivers, Applications and Passive Components*, Chapter 17, pp. 617-675, 2006

[123] D. Hanselman, *Brushless Permanent Magnet Motor Design*, 2nd Ed, McGraw-Hill, New York, 1994.

[124] C. C. Hwang, C. M. Chang, S. P. Cheng, C. K. Chan, C. T. Pan, and T. Y. Chang, "Comparison of Performances between IPM and SPM Motors with Rotor Eccentricity", *Journal of Magnetism and Magnetic Materials*, Vol. 282, pp. 360-363, 2004.

[125] F. Libert and J. Soulard, "Design Study of Different Direct-Driven Permanent-Magnet Motors for a Low Speed Application", *Proc. of Nordic Workshop on Power and Industrial Electronics (NORpie*), 2004.

[126] P. Lampola, "*Direct Driven. Low-Speed Permanent-Magnet Generators for Wind Power Applications*", Thesis for the degree of Doctor of Science, Helsinki University of Technology 2000.

[127] I. Elosegui, M. Martinez-Iturralde, A. Garcia Rico, J. Florez, J. M. Echeverra, and L. Fontan, "Analytical Design of Synchronous Permanent Magnet Motor/Generators", *Proc. of IEEE International Symposium on Industrial Electronics*, pp. 1165-1170, 2007.

[128] Y. G Guo, Y. P. Dou, J. G. Zhu, Y. D. Zhan, and J. X. Jin, "Parameter Determination and Performance Analysis of a PM Synchronous Generator by

Magnetic Field Finite Element Analysis", *Proc. of Australasian Universities Power Engineering Conference (AUPEC 2007)*, pp. 1-4, 2007.

[129] T. F. Chan, W. Wang, and L. L. Lai, "Analysis and Performance of a Permanent Magnet Synchronous Generator Supplying an Isolated Load", *IET Electric Power Applications*, Vol. 4, No. 3, pp. 169-176, 2010.

[130] T. F. Chan, W. M. Wang, and L. L. Lai, "Permanent-Magnet Synchronous Generator Supplying an Isolated Load", *IEEE Transactions on Magnetics*, Vol. 46, No. 8, pp. 3353-3356, 2010.

[131] I. Boldea, *The Electric Generators Handbook: Variable Speed Generator*. Taylor & Francis Group, 2006.

[132] J. Z. Zhang, M. Cheng, and Z. Chen, "Optimal Design of Stator Interior Permanent Magnet Machine with Minimized Cogging Torque for Wind Power Application", *Energy Conversion and Management*, Vol. 49, No. 8, pp. 2100-2105, 2008.

[52] D. V. Evans, "Power from Water Waves", *Annual Review of Fluid Mechanics*, Vol. 13, 1981, pp. 157-187, 1981.

[133] M. R. Harris, "Comparative Electromagnetic Parameters for Alternative Motor Types", *IEE Colloquium on Motors and Drives for Battery Powered Propulsion*, pp. 3/1-3/4, 1993.

[134] T. J. E. Miller, *Switched Reluctance Motors and Their Control*, Magna Physics publishing division, pp. 163, 1993,.

[135] S. K. Bhattacharya, Electrical Machines, 3rd Edition, Tata McGraw-Hill Publishing Company Limited, 2009.

[136] J. A. Walker, D. G. Dorrell and C. Cossar, "Flux-Linkage Calculation in Permanent- Magnet Motors Using the Frozen Permeabilities Method", *IEEE Trans. On Magnetics*, Vol. 41, No. 10, Oct 2005.

[137] J. F. Gieras, E. Santini, M. Wing, "Calculation of Synchronous Reactances of Small Permanent-Magnet Alternating-Current Motors: Comparison of Analytical Approach and Finite Element Method with Measurements" *IEEE Transactions on Magnetics*, Vol. 34, No. 5, Sept 1998.

[138] M. Wing and J. Gieras, "Accuracy of Finite Elements in Computing the Synchronous Reactances of Surface and Buried Permanent Magnet Brushless Motors", *The International Journal for Computation and Mathematics in Electrical and Electronic Engineering*, Vol. 14, No. 4, pp. 71-74, 1995.

[139] L. Petkovska and G. Cvetkovski, "Steady State Performance Evaluation of a Permanent Magnet Synchronous Motor Based on FEA", *Proc. of the 9 Spanish Portuguese Congress on Electrical Engineering*, 2005.

[140] T. Lubin, T. Hamiti, H. Razik and A. Rezzoug, "Comparison Between Finite-Element Analysis and Winding Function Theory for Inductances and Torque Calculation of a Synchronous Reluctance Machine", *IEEE Trans. on Magnetics*, Vol. 43, No. 8, August 2007.

[141] G. Michalke, A.H. Hansen, and T. Hartkopf, "Control strategy of a variable speed wind turbine with multipole permanent magnet synchronous generator", *Proc. 2007 European Wind Energy Conference and Exhibition (EWEC 2007)*, Brussels, 2007.

[142] S. Arnaltes, "Comparison of Variable Speed Wind Turbine Control Strategies", *Proc. International Conference on Renewable Energies and Power Quality (ICREPQ' 03)*, 9-12 April 2003.

[143] O. B. K. Hasnaour, J. Belhadj, and M. Elleuch, "Direct Drive Permanent Magnet Synchronous Generator Wind Turbine Investigation – Low Voltage Ride Through Capability Dynamic Behaviour in Presence of Grid", *Journal of Electrical System*, Vol. 4, No. 3, Sept 2008.

[144] E. Muljadi, K. Pierce, P. Migliore, "Control Strategy for Variable-Speed Stall-Regulated Wind Turbines", *National Renewable Energy Laboratory (NREL) Report*, No. CP-500-24311, pp. 7, 1998.

[145] M. P. Kazmierkowski, R. Krishnan, and F. Blaabjerg, *Control in Power Electronics*, pp. 487-506, Academic Press, 2002.

[146] B. Boukhezzar, "Comparison Between Linear and Nonlinear Control Strategies for Variable Speed Wind Turbnie Power Capture Optimization", *Proc. International Conference and Exhibition on Ecological Vehicles and Renewable Energies, (EVER 2009)*, 26-29 March 2009.

[147] J. Tedd, *Testing, Analysis and Control of Wave Dragon, Wave Energy Converter*, PhD Thesis, Aalborg University, 2007.

[148] J. Tedd, J. P. Kofoed, M. Jasinski, A. Morris, E. Friis-Madsen, R. Wisniewski, and J. D. Bendtsen, "Advanced Control Techniques for WEC Wave Dragon", *Proc. of the 7th European Wave and Tidal Energy Conference (EWTEC 2007)*, 2007.

[149] M. Amundarain, M. Alberdi, A.J. Garrido, and I. Garrido, "Modeling and Simulation of Wave Energy Generation Plants: Output Power Control", *IEEE Transactions on Industrial Electronics*, Vol. 58, No.1, 2011.

[150] D. L. O'Sollivan and A.W. Lewis, "Generator Selection and Comparative Performance in Offshore Oscillating Water Column Ocean Wave Energy Converters", *IEEE Transactions on Energy Conversion*, Vol. 26, No. 2, 2011.

[151] M. Kamensky, M. Guglielmi, and A. Formal'Skii, "Optimal Switching Control of an Absorber Ocean Wave Energy Device", 16th Mediterranean Conference of Control and Atomation, pp. 785-790, 2008.

[152] E. Tedeschi, and M. Molinas, "Impact of Control Strategies on the Rating of Electric Power Take Off for Wave Energy Conversion", *2010 IEEE International Symposium on Industrial Electronics (ISIE)*, pp. 2406-2411, 2010.

[153] G. Boyle, *Renewable Energy – Power for a Sustainable Future*, Oxford University Press, 2004.

[154] D. G. Dorrell, "Design Requirements for Brushless Permanent Magnet Generators for Use in Small Renewable Energy Systems", *Proc. of IEEE Industrial Electronics Society Annual Meeting (IECON)*, 2007.

[155] J. R. Halliday, D. G. Dorrell, and A. Wood, "Fourier Approach to Short Term Deterministic Wave Prediction", *International Conference of the Offshore and Polar Engineers Society (ISOPE)*, 2006.

[156] M. P. Schoen, J. Hals, and T. Moan, "Wave Prediction and Robust Control of Heaving Wave Energy Devices for Irregular Waves", *IEEE Transactions on Energy Conversion*, Vol. 26, No. 2, June 2011.

[157] D. Mehrzad, J. Luque, and M. Capella, *Vector Control of PMSG for Wind Turbine Applications*, Department of Energy Technology, Aalborg University.

[158] "Feasibility study of Bristol Cylinder wave device," Green Cat Renewables, unpublished report.

[159] I. Munteanu, A. I. Bratcu, N. A. Cutululis, and E. Ceanga, *Optimal Control of Wind Energy Systems: Towards a Global Approach*, Springer-Verlag London Limited, 2008

[160] Shuhui Li, T. A. Haskew, and L. Xu, *Conventional and Novel Control Designs for Direct Driven PMSG Wind Turbines*, Electric Power Systems Research, In Press, Available online 21 October 2009.

[161] M.S. Merzoug, and F. Naceri, "Comparison of Field-Oriented Control and Direct Torque Control for Permanent Magnet Synchronous Motor (PMSM)", *World Academy of Science, Engineering and Technology*, Vol. 45, pp. 300-305, 2008.

[162] A. Chikhi, M. Djarallah, and K. Chikhi, "A Comparative Study of Field-Oriented Control and Direct-Torque Control of Induction Motors Using An

Adaptive Flux Observer", *Serbian Journal of Electrical Engineering*, Vol. 7, No. 1, 2010.

[163] M. Singh, and A. Chandra, "Control of PMSG Based Variable Speed Wind-Battery Hybrid System in an Isolated Network", *IEEE Power & Energy Society General Meeting (PES 09)*, pp. 1-6, 2009.

[164] M. li, and K. Smedley, "One-Cycle Control of PMSG for Wind Power Generation", *IEEE Power Electronics and Machines in Wind Applications, (PEMWA 2009)*, pp. 1-6, 2009.

[165] M. G. Molina, and P. E. Mercado, "An Efficient Control Strategy of Variable Speed Wind Turbine Generator for Three-Phase Grid-Connected Applications", *13th Regional Meeting of the Ibero-American Cigre-grouping*, pp. 1-8, 2009.

[166] C. Stancu, S. Hiti, and F. Biais, "Maximum Torque-Per-Ampere Control of A Saturated Surface-Mounted Permanent Magnet Motor", *IEEE 33rd Annual Power Electronics Specialists Conference (PESC 2002)*, Vol. 4, pp. 1667-1672, 2002.

[167] B. Boukhezzar, "Comparison Between Linear and Nonlinear Control Strategies for Variable Speed Wind Turbnie Power Capture Optimization", *Proceeding of the International Conference and Exhibition on Ecological Vehicles and Renewable Energies (EVER 2009)*, 2009.

[168] A. Abedini, *Integration of Permanent Magnet Synchronous Generator Wind Turbines Into Power Grid*, Phd Dissertation, The University of Wisconsin-Milwaukee, 2008.

[169] S. Y. Park, J. S. Lai, and W. C. Lee, "An Easy, Simple, and Flexible Control Scheme for a Three-Phase Grid-Tie Inverter System", *2010 IEEE Energy Conversion Congress and Exposition*, pp. 599-603, 2010.

[170] G. Q. Shen, J. Zhang, X. Li, C. R. Du, and D. H. Xu, "Current Control Optimization for Grid-Tied Inverters with Grid Impedance Estimation", *2010*

25th Annual IEEE Applied Power Electronics Conference and Exposition (APEC), pp. 861-866, 2010.

[171] Z. Q. Qin, S. P. Su, J. N. Lei, and H. Dong, "Study on Intelligent Control of Three Phase Grid-Connected Inverter of Wind Power Generation", 2008 International Conference on Intelligent Computation Technology and Automation (ICICTA), pp. 1149-1152, 2008.

[172] X. Jin, "Photovoltaic Grid-Connected Inverter Harmonic Compensation and Grid-Connected Unified Control", *2009 Asia-Pacific Power and Energy Engineering Conference (APPEEC)*, pp. 1-4, 2009.

[173] E. Isen and A. F. Bakan, "Simulation of Three-Phase Grid Connected Parallel Inverters with Current Error Compensation Control", *2011 8th International Conference on Electrical Engineering/Electronics, Computer, Telecommunications and Information Technology (ECTI-CON)*, pp. 748-751, 2011.

[174] G. A. Raducu, *Control of grid side inverter in a B2B configuration for WT applications*, Master Thesis, Aalborg University, 2008.

[175] National Grid Electricity Transmission, *The Grid Code*, National Grid Electricity Transmission, 2011.

[176] UK Power Networks, *Design and Planning: Framework for underground networks in UK power networks*, UK Power Networks, 2011.

[177] S. Butler, *UK Electricity Networks: The nature of UK electricity transmission and distribution networks in an intermittent renewable and embedded electricity generation future*, Imperial College of Science, Technology and Medicine Centre for Environmental Technology, 2001.

[178] SP Transmission & Distribution, *The Scottish Grid Code*, SP Transmission & Distribution, 2002.

[179] D. Mehrzad, J. Luque, and M. C. Cuenca, *Vector Control of PMSG for Grid-Connected Wind Turbine Applications*, Master Thesis, Institute of Energy Technology, Aalborg Universitet, 2009.

[180] Y. Tang, J. K. Wei, and S. J. Xie, "A New Direct Peak DC-Link Voltage Control Strategy of Z-Source Inverters", *2010 25th Annual IEEE Applied Power Electronics Conference and Exposition (APEC)*, pp. 867-872, 2010.

[181] T. L. Vandoorn, B. Meersman, L. Degroote, B. Renders, and L. Vandevelde, "A Control Strategy for Islanded Microgrids With DC-Link Voltage Control", *IEEE Transactions on Power Delivery*, pp. 703-713, 2011.

[182] X. B. Yuan, F. Wang, R. Burgos, Y. D. Li, and D. Boroyevich, "DC-Link Voltage Control of Full Power Converter for Wind Generator Operating in Weak Grid Systems", *2008 23rd Annual IEEE Applied Power Electronics Conference and Exposition (APEC)*, pp. 761-767, 2008.

[183] S. Dasgupta, S. K. Sahoo, and S. K. Panda, "Single-Phase Inverter Control Techniques for Interfacing Renewable Energy Sources With Microgrid-Part I: Parallel-Connected Inverter Topology with Active and Reactive Power Flow Control Along With Grid Current Shaping", *2008 IEEE Transactions on Power Electronics*, Vol. 26, No. 3,pp. 717-731, 2011.

[184] D. L. Logue and P. T. Krein, "Utility Distributed Reactive Power Control Using Correlation Techniques", *2001 16th Annual IEEE Applied Power Electronics Conference and Exposition (APEC)*, pp. 1294-1300, 2001.

[185] G. H. Choe, A. K. Wallace, and M. H. Park, "Control Technique of Active Power Filter For Harmonic Elimination and Reactive Power Control", *Conference Record of the 1988 IEEE Industry Applications Society Annual Meeting*, pp. 859-866, 1988.

[186] R. Uhrin, and F. Profumo, "Performance Comparison of Output Power Estimators used in AC/DC/AC Converters", *1994 20th International*

Conference on Industrial Electronics, Control and Instrumentation, pp. 344-348, 1994.

[187] M. M. Amin, M. A. Elshaer, and O. A. Mohammed, "DC Bus Voltage Control for PV Sources in a DC Distribution System Infrastructure", *2010 IEEE Power and Energy Society General Meeting*, pp. 1-5, 2010.

Appendix 1

UTS MICRO WAVE TANK DRAWINGS

Plans for Steelwork for New Micro Wavetank in CB 2.02.07

Materials

Materials nominally specified as 100 mm box section and 100 mm angle section. This can be reduced if necessary if still deemed strong enough, There will be up to 2200 Kg of water in the tank when full.

All uprights and 6 horizontal stretchers (shown) are 100 mm box section steel:

8 uprights × 1.8 m + 6 uprights × 0.7 m + 6 stretchers × 1.1 m = 25.2 m of 100 mm square box section

All other components are 100 mm angle section:

6 runners × 4.9 m + 8 diagonal bracers × 0.91 m + 7 stretchers × 1.1 m = 44.38 m of 100 mm angle section

Construction: To be welded or bolted as required

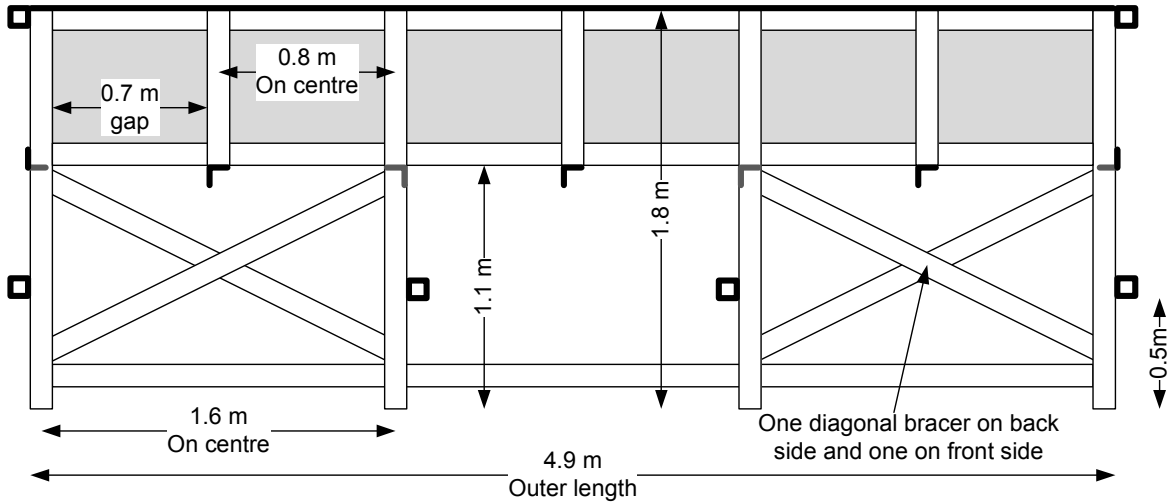

SIDE VIEW

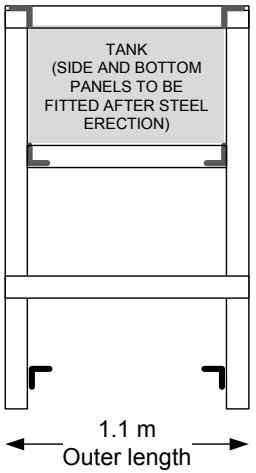

END VIEW

D G Dorrell
1 June 2011

Plans for Beach and paddle for New Micro Wavetank in CB 2.02.07

Calculations

Large sump tank is 3500 L.

Tank water volume = 0.45 × 0.9 × 4.9 = 1.98 m2 = 1980 L; for 2 minute filling 1000 L/min or 16 L/s (current pumps on hydro are be close to this)

Target waves 100 mm height at 0.5 m wavelength: T = 0.58 s giving 0.8 W/m of wavefront (about 6 wavelengths)

Maximum period = 1 s (about 2 wavelengths), minimum period 0.3 s

Recirculation pump – assume overtopping by 100 mm (worst case) wave. Worst case water volume = 0.5 × 0.5 sec × 0.9 width × 0.1 waveheight / 0.58 period = 0.038 = 38 L/s. This seems very high but is an absolute maximum over-calculation based on the vulume of water on the wave from peak to trough and total length; the water level will drop and the amount overtopping will decrease. Try try small pump at 2 L/s then go back to large sump pump if this does not work.

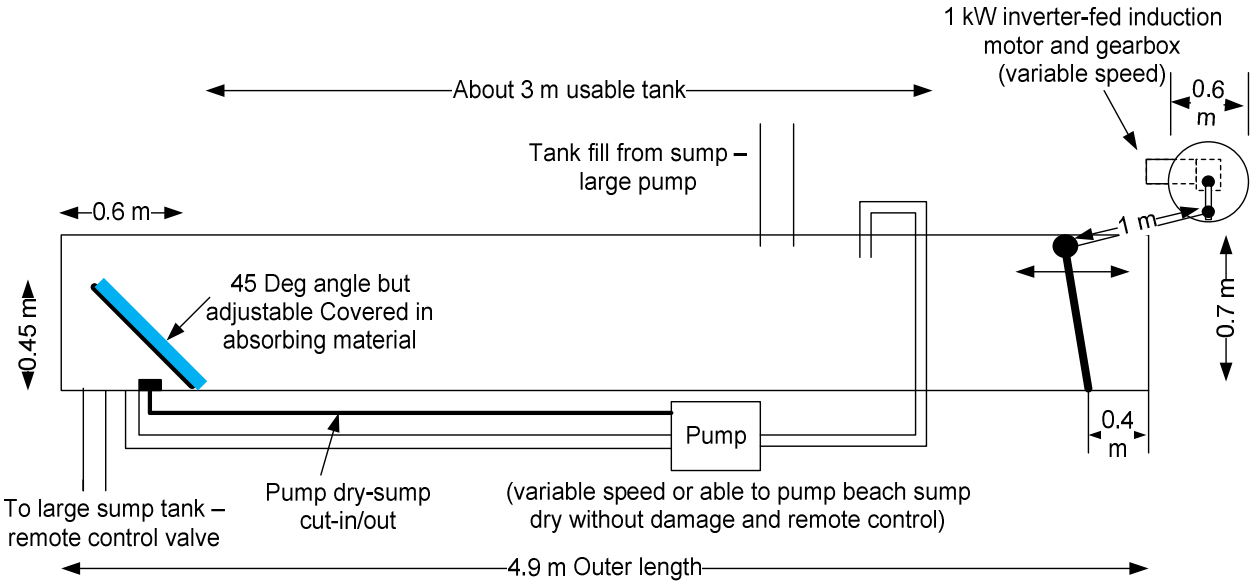

CROSS SECTION LENGTHWAYS VIEW

D G Dorrell
26 Aug 2011

Plans for Paddle for New Micro Wavetank in CB 2.02.07

Similar system at University of Glasgow (this was changed to the paddle being at the back and the motor drive being in front of the paddle)

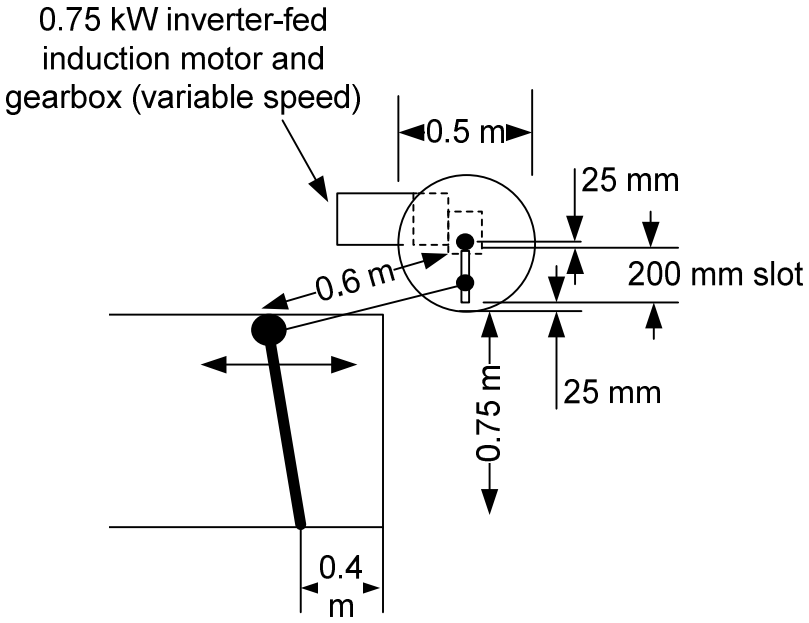

D G Dorrell
8 Sept 2011

Appendix 2

FEMM LUI PROGRAM

The following code was written to synchronously rotate the rotor and current phasors in the FEMM generator model.

```
open("r38-torqueV0-0.fem")
mi_saveas("temp.fem")

pi = 3.141592
step = 1

for deg=0, 15, step do
                t=(1/360)*deg
                ia=0.5*cos(2*pi*23.98*t)
                  ib=0.5*cos(2*pi*23.98*t+(2/3)*pi)
                  ic=0.5*cos(2*pi*23.98*t+(4/3)*pi)
                mi_seteditmode("group")
                mi_selectgroup(1)
                mi_moverotate(0,0,step)
                mi_modifycircprop ("Ia",1,ia)
                mi_modifycircprop ("Ib",1,ib
                mi_modifycircprop ("Ic",1,ic)

                mi_analyze()
                mi_loadsolution()

                --collect the flux linkage for each phase
                i1,v1,flux1=mo_getcircuitproperties("Ia")
                  i2,v2,flux2=mo_getcircuitproperties("Ib")
                 i3,v3,flux3=mo_getcircuitproperties("Ic")

                -- cogging torque calculation routine
                mo_groupselectblock(1)
                cog=mo_blockintegral(22)
                mo_clearblock(1)

                mo_groupselectblock(3)
                  currenta=mo_blockintegral(7)
                  mo_clearblock(3)

                mo_groupselectblock(2)
                  A1=mo_blockintegral(1)
```

```
                mo_clearblock(2)

               mo_groupselectblock(3)
                A2=mo_blockintegral(1)
                mo_clearblock(3)

               mo_groupselectblock(4)
                A3=mo_blockintegral(1)
                mo_clearblock(4)

               mo_groupselectblock(5)
                A4=mo_blockintegral(1)
                mo_clearblock(5)

                handle = openfile("cogtor1.dat","a")
              write(handle,deg,"     ",i1," ",flux1," " ,A1," ",A2," ",A3," ",A4," ","\n")
               closefile(handle)

        mo_close()
end
```

Appendix 3

PUBLISHED PAPERS

The following papers have been published in relation to this project:

[1] S. S. Ngu, D. G. Dorrell and E. Acha, “Control of a Bristol Cylinder for Wave Energy Generation”, International Power Electronics Conference (IPEC), Japan, 2010, pp 3196 – 3203.

[2] D. G. Dorrell, S. S. Ngu and C. Cossar, “Comparison of High Pole Number Ultra-Low Speed Generator Designs Using Slotted and Air-Gap Windings”, IEEE Transactions on Magnetics, Vol. 48, Iss. 11, 2012, pp 3120 – 3123.

[3] D. G. Dorrell, S. S. Ngu and C. Cossar, “Outline design of a direct-drive low-speed brushless permanent-magnet generator for an ocean-going Bristol-cylinder type device”, IEEE International Symposium on Industrial Electronics (ISIE), Hangzhou, China, 2012, pp 1444 – 1449.

[4] S. S. Ngu, D. G. Dorrell and C. Cossar, “Design and operation of very slow-speed generators for a Bristol cylinder sea wave generating device”, IEEE Energy Conversion Congress and Exposition (ECCE), Raleigh, USA, 2012, pp 946 – 953.

[5] D. G. Dorrell, S. S. Ngu and C. Cossar, “Comparison of permanent magnet generators for a very low speed renewable energy application”, International Conference on Electrical Machines (ICEM), Marseille, France, 2012, pp 115 – 121.